DISTRIBUTION OF STRESS IN THREE-DIMENSIONAL MODELS OF HUMAN CORONARY ATHEROSCLEROTIC PLAQUE BASED ON ACRYLIC HISTOLOGIC SECTIONS

A Dissertation
Presented to
The Academic Faculty

by

Margaret Loraine Lowder

In Partial Fulfillment
of the Requirements for the Degree
Doctor of Philosophy in Bioengineering

Georgia Institute of Technology
August 2007

COPYRIGHT 2007 BY MARGARET LORAINE LOWDER

DISTRIBUTION OF STRESS IN THREE-DIMENSIONAL MODELS OF HUMAN CORONARY ATHEROSCLEROTIC PLAQUE BASED ON ACRYLIC HISTOLOGIC SECTIONS

Approved by:

Dr. Raymond P. Vito, Advisor
School of Mechanical Engineering
Georgia Institute of Technology

Dr. Oskar Skrinjar
Department of Biomedical Engineering
Georgia Institute of Technology

Dr. Robert E. Guldberg
School of Mechancial Engineering
Georgia Institute of Technology

Dr. W. Robert Taylor
Department Biomedical Engineering
Georgia Institute of Technology
Division of Cardiology
Emory University School of Medicine

Dr. John N. Oshinski
Department of Biomedical Engineering
Georgia Institute of Technology
Division of Radiology
Emory University School of Medicine

Date Approved: May 30, 2007

To my mom, dad, and brother

ACKNOWLEDGEMENTS

I am absolutely amazed and humbled by the many who have invested in me. They have made the completion of this work possible. First, I must thank my advisor, Dr. Raymond Vito. I am grateful that I have had the opportunity to work under his expert leadership on this interesting project. I thank him for his instruction, direction, and for encouraging me to achieve.

I would also like to thank to my committee members, Dr. Robert Guldberg, Dr. John Oshinski, Dr. Oskar Skrinjar, and Dr. Robert Taylor for their willingness to share of their time and knowledge. I gratefully recognize Dr. Alexander Rachev. His countless suggestions, based on his in-depth understandings, have greatly improved the quality of my work and have helped to shape this dissertation.

I owe a sincere debt of gratitude to Dr. Jack Lackey. Dr. Lackey was first my professor and then, and to this day, my mentor. Were it not for him, I would not have attended graduate school. I cannot express my appreciation for his endless guidance, advice, and encouragement. In my lifetime, I can only hope to have as profound an influence on another person, as he has had on me.

I would like to thank Tracey Couse for graciously sharing her histology-related expertise. Her insights and efforts were crucial to the success of my research. On a personal note, Tracey is one of the kindest and most helpful people I have ever met. I thank her and her husband, Anthony Couse, for their compassion and friendship.

I have had the pleasure of working with wonderful people while in the Vito Laboratory. I extend my thanks to them for creating an intellectually stimulating and

enjoyable work environment. I also thank them for their sound recommendations pertaining to my research. Dr. Peter Carnell, whose wealth of knowledge is beyond impressive, was always willing to offer ideas. I profited significantly from his groundwork. His help and support were invaluable. Dr. Senhu Li likewise contributed to my accomplishments. His overall pleasantness made my interactions with him delightful. I can think of no greater lab mate than Dr. Brian Wayman. Brian is truly blessed with the gifts of encouragement and optimism and I have benefited tremendously as a result of our friendship. Much to my relief, Melissa Hallow has shared in the workload of generating thousands of histology sections and has done it with a nice attitude. YuShin Kim, Karen Tisdale, Dr. James Warnock, Jonathan Morris, Dr. Hai-Chao Han, and Dr. Pete Davis have also been exceedingly helpful. I was honored to have worked with two undergraduate mentees, Alex Podust and Shaun Eshraghi. I am overwhelmed by their outstanding intellect and potential. I thank them for their useful assistance.

I would like to thank several members of the Guldberg Laboratory, Angela Lin, Dr. Srinidhi Nagaraja, and Galen Robertson, for their helping hand with the micro-CT scanner. I thank Holifield Farms for the donation of the tissue that was used in the first part of my work and Daiana Weiss for preparing the tissue that was used in the latter stages. I also thank the anonymous organ donors and heart transplant recipients who made this work possible.

I would be remiss if I did not thank the many staff members at the Petit Institute for Bioengineering and Bioscience who have been a great help to me. I especially thank Steve Woodard, Chris Ruffin, Segried Allen, Allen Echols, Rudy Paratchek, and Sha'Aqua Asberry.

I gratefully acknowledge my fellow graduate students who I'm privileged to have met: Onyi Irrechukwu, JoSette Broiles, Harvinder Gill, Veer Mahajan, Dr. Srinidhi Nagaraja, Megan Oest, and Padmini Rangamani. Each has been sympathetic to the challenges and rewards of graduate school. I thank them for sharing in my frustrations and joys.

I thank my former teachers at Suder Elementary, Jonesboro Middle, and Jonesboro High schools for the difference they made.

I must thank my dear friends, Lorinda and Austin Sapp and Melanie and Rod Tatum, for their unending encouragement. I could not hope for better friends. I also thank Mrs. Lenora Moneyheffer and her late husband, Mr. Paul Moneyheffer for being wonderful examples of goodness.

I lovingly acknowledge my many extended family members in Alabama, California, Colorado, South Carolina, and here in Georgia whose contributions are too numerous to mention. A famous author once said, "No matter what you've done for yourself or for humanity, if you can't look back on having given love and attention to your own family, what have you really accomplished?" I hope my family is as certain of my love and devotion to them, as I am of theirs to me.

Finally, I thank those who matter most: my mother, Jackie Lowder, who I miss more than I could ever convey, my father, Sam Lowder, my brother, Keigm Lowder, and my sister-in-law, Mahli Lowder. They are my teachers and my friends. They are my inspiration and my greatest source of joy. I am propelled by their support and belief in me. I am forever grateful for their unwavering love.

TABLE OF CONTENTS

Page

ACKNOWLEDGEMENTS iv

LIST OF TABLES xi

LIST OF FIGURES xiii

LIST OF ABBREVIATIONS xvii

SUMMARY xviii

CHAPTER 1: BACKGROUND 1

Atherosclerosis and Its Progression 3

Plaque Classification 8

Plaque Features and Stability 9

Fibrous Cap Thickness 10

Lipid Content 10

Inflammatory Cell Content 11

Stenosis Severity 12

Calcification Content 13

Mechanical Stresses and Stability 13

Need for Histology 15

Histologic Related Distortions 17

Methyl Methacrylate 19

Mechanical Properties of Arterial Tissue 20

Finite Element Models of Atherosclerotic Plaques 23

Two-Dimensional Analyses 24

Three-Dimensional Analyses 27
CHAPTER 2: RESEARCH OBJECTIVES 30
Hypothesis 30
Specific Aim I 31
Specific Aim II 32
Specific Aim III 33
CHAPTER 3: MATERIALS AND METHODS 34
Specific Aim I 34
Tissue Preparation 34
Histologic Preparation 35
Micro-CT and Histologic Image Acquisition 36
Registration Marks 36
3-D Reconstruction Techniques and Measurements 37
Distortion Correction 40
Error in Distortion Correction 40
Comparison of Methyl Methacrylate and Paraffin 41
Statistics 42
Specific Aim II 42
Modeling of Geometry 43
Modeling of Mechanical Properties 62
Modeling of Loading and Boundary Conditions 69
Stress Calculations 71
Normalization of Stress 72

Two-Dimensional Mechanical Modeling 73
Validation for Sectioning Interval 74
Specific Aim III 81
Longitudinal Variation 82
Fibrous Cap Thickness 82
Lipid Content 83
Stenosis Severity 83
Calcification Content 84
Statistics 84
CHAPTER 4: RESULTS 86
Specific Aim I 86
Micro-CT and Histology Images 86
Shrinkage and Sectioning Distortions 87
Distortion Correction 88
Comparison of Methyl Methacrylate and Paraffin 90
Specific Aim II 91
Specimens 91
Three-Dimensional Mechanical Models 92
Specific Aim III 95
Three-Dimensional Distribution of Stress 96
Stress Predictions from 3-D versus Plane Strain Models 99
Effect of Plaque Features 107
Effect of Plaque Features on 3-D versus 2-D Model Stress Predictions 113

CHAPTER 5: DISCUSSION 118
Specific Aim I 118
Measuring and Correcting for Histologic Distortions 118
Distortions in Methyl Methacrylate versus Paraffin 120
Limitation of Specific Aim I 121
Additional Applications 121
Specific Aim II 122
Modeling Approach 122
Limitations of Specific Aim II 123
Specific Aim III 125
Distribution of Stress 125
Effect of Longitudinal Variation 126
Effects of Fibrous Cap Thickness and Lipid Content 128
Effect of Stenosis Severity 130
Effect of Calcification Content 130
Limitation of Specific Aim III 131
Clinical Relevance 131
CHAPTER 6: CONCLUSIONS AND FUTURE WORKS 133
Conclusions 133
Future Works 136
APPENDIX A: HISTOLOGY PROTOCOLS 139
APPENDIX B: MATLAB CODE 150
REFERENCES 202

LIST OF TABLES

Page

Table 1.1: Modified AHA classification scheme for atherosclerotic plaques. Table modified from Virmani, et al. (2000) 9

Table 3.1: Average color channel values of pixels in a stained image classified as either background, media, or other tissue in the corresponding manual segmentation..... 53

Table 3.2: Average values of moduli (n=7) of plaque constituents (Beattie, et al., 1998) 63

Table 3.3: Percent change in volume of outer wall and luminal reconstructions as a result of downsizing from all sections to every second, third, forth, or fifth section..... 76

Table 3.4: Percent change in mean, maximum, and minimum von Mises stress (35,070 elements)..... 78

Table 3.5: Percent change in mean, maximum, and minimum von Mises stress (corresponding center cross-section) 80

Table 3.6: Percent change in mean, maximum, and minimum von Mises stress (62,795 elements)..... 81

Table 4.1: Summary of distortions due to histologic preparation including axial and cross-sectional area shrinkage, and principal strains ($\varepsilon 1$ and $\varepsilon 2$). Also included is the angle between the principal strain direction and the cutting direction (ϕ)..... 88

Table 4.2: Summary of sectioning and shrinkage correction associated errors..... 89

Table 4.3: Maximum stress in corresponding cross-section models..... 90

Table 4.4: Maximum stress in serial MMA and paraffin cross-section models 90

Table 4.5: Characteristics of patients from which specimens were collected..... 91

Table 4.6: Classification of specimens..... 92

Table 4.7: Geometric characteristics of models..... 92

Table 4.8: Spearman rank correlations for normalized stresses versus fibrous cap thickness 108

Table 4.9: Spearman rank correlations for normalized stresses versus lipid content 110

Table 4.10: Spearman rank correlations for normalized stresses versus stenosis severity 111

Table 4.11: Spearman rank correlations for normalized stresses versus calcification content 113

LIST OF FIGURES

Page

Figure 1.1: AHA classification scheme for atherosclerotic plaques. Figure modified from Stary, et al. (1995) 8

Figure 3.1: Photograph of the mounting system used 35

Figure 3.2: Graphic user interface used to select registration marks in a histologic image 38

Figure 3.3: Schematic of the approach used to compare the effects of preparation related distortions on stresses in acrylic versus paraffin 41

Figure 3.4: Schematic overview of methods used to develop 3-D FE models of plaques 43

Figure 3.5: Change in pressurized diameter of a porcine carotid artery with respect to time due to pressure fixation at 80 mm Hg 45

Figure 3.6: Representative image of a slide in the unstained (A) and stained (B) state 48

Figure 3.7: Selection of a landmark in an unstained (A) and stained (B) image 49

Figure 3.8: Representative image of an unstained section 50

Figure 3.9: Alignment techniques applied to an idealized case 51

Figure 3.10: Representative image of a stained section (A) and the corresponding manual segmentation (B) 52

Figure 3.11: Representative image of a stained section (A) and the corresponding automatic segmentation (B) 54

Figure 3.12: Steps used to identify the arterial wall. 55

Figure 3.13: Representative semi-automatic segmentations of lipid (A) and calcification (B) 56

Figure 3.14: Representative segmentation of an image of a stained artery in which each pixel has been classified as media, fibrous intima, lipid, calcification, or background 56

Figure 3.15: Steps followed to obtain a NURBS surface of the lumen of an artery 60

Figure 3.16: Steps followed to obtain a solid model of an artery 61

Figure 3.17: Ansys Solid 187 element geometry 65

Figure 3.18: Schematic representation of mixture theory 66

Figure 3.19: Steps followed to obtain regions of interest in segmentations used to calculate mechanical properties for each element 68

Figure 3.20: Ansys Plane 42 element geometry 73

Figure 3.21: Total number of pixels of healthy tissue (A), lipid (B), fibrous intima (C), and calcification (D) in each section collected at an interval of 30 μm 75

Figure 3.22: Reconstructions of the outer wall surface based on every section (A) and every 5th section (B) and of the luminal surface based on every section (C) and every 5th section (D) 77

Figure 3.23: von Mises stress distribution in a corresponding cross-section from models based on all sections (A), every 2nd section (B), every 3rd section (C), every 4th section (D), and every 5th section (E) 79

Figure 4.1: Cross-sectional images of an artery in its fresh (A), embedded (B), and sectioned and stained state (C) 87

Figure 4.2: Corresponding segmented cross-sectional images of an artery in its fresh state (A), embedded state (B), and sectioned and stained state (C), and reconstructions of the sectioning artifact corrected state (D), and shrinkage artifact corrected state (E) 89

Figure 4.3: Solid and skeleton views of the model of Specimen A 93

Figure 4.4: Solid and skeleton views of the model of Specimen B 93

Figure 4.5: Solid and skeleton views of the model of Specimen C 94

Figure 4.6: Solid and skeleton views of the model of Specimen D 94

Figure 4.7: Solid and skeleton views of the model of Specimen E 95

Figure 4.8: von Mises stress distribution in Pa for 3-D model of Specimen A 96

Figure 4.9: von Mises stress distribution in Pa for 3-D model of Specimen B 97

Figure 4.10: von Mises stress distribution in Pa for 3-D model of Specimen C 97

Figure 4.11: von Mises stress distribution in Pa for 3-D model of Specimen D 98

Figure 4.12: von Mises stress distribution in Pa for 3-D model of Specimen E 98

Figure 4.13: Mean upper quartile stress in 3-D versus plane strain models 99

Figure 4.14. Mean maximum stress in 3-D versus plane strain models 100

Figure 4.15: von Mises stress distributions in Pa for 2-D models and 3-D model of Specimen A 102

Figure 4.16: von Mises stress distributions in Pa for 2-D models and 3-D model of Specimen B 103

Figure 4.17: von Mises stress distributions in Pa for 2-D models and 3-D model of Specimen C 104

Figure 4.18: von Mises stress distributions in Pa for 2-D models and 3-D model of Specimen D 105

Figure 4.19: von Mises stress distributions in Pa for 2-D models and 3-D model of Specimen E 106

Figure 4.20: Normalized mean stresses at axial locations with thin (< 65 μm) versus thick fibrous caps 108

Figure 4.21: Normalized mean stresses at axial locations with lipid versus no lipid 109

Figure 4.22: Normalized mean stresses at axial locations with high stenosis severity (> 40%) versus low stenosis severity (< 40%) 111

Figure 4.23: Normalized mean stresses at axial locations with calcification versus no calcification 112

Figure 4.24: Stress values from the 3-D model, stress values from the 2-D models, and fibrous cap thickness at corresponding axial locations in Segment 1 of Specimen D 114

Figure 4.25: Stress values from the 3-D model, stress values from the 2-D models, and fibrous cap thickness at corresponding axial locations in Segment 1 of Specimen C 114

Figure 4.26: Stress values from the 3-D model, stress values from the 2-D models, and fibrous cap thickness at corresponding axial locations in Segment 1 of Specimen E 115

Figure 4.27: Stress values from the 3-D model, stress values from the 2-D models, and lipid content at corresponding axial locations in Segment 2 of Specimen D 116

Figure 4.28: Stress values from the 3-D model, stress values from the 2-D models, and lipid content at corresponding axial locations in Segment 2 of Specimen C 116

Figure 4.29: Stress values from the 3-D model, stress values from the 2-D models, and lipid content at corresponding axial locations in Segment 2 of Specimen E 117

LIST OF ABBREVIATIONS

2-D	Two-Dimensional
3-D	Three-Dimensional
AHA	American Heart Association
CHD	Coronary Heart Disease
EC	Endothelial Cell
FE	Finite Element
GMA	Glycol Methacrylate
IVUS	Intravascular Ultrasound
LDL	Low-Density Lipoprotein
Micro-CT	Microcomputed Tomography
MDCT	Multi-Detector Row Computed Tomography
MMA	Methyl Methacrylate
MMP	Matrix Metalloproteinase
MMP-1	Interstitial Collagenase
MMP-3	Stromelysin
MMP-9	Gelatinase
MRI	Magnetic Resonance Imaging
NURBS	Non-Uniform Rational B-Spline
OCT	Optical Coherence Tomography
RCA	Right Coronary Artery
SMC	Smooth Muscle Cell

SUMMARY

Each year in the United States over a million people experience a myocardial infarction. The majority of these attacks are caused by coronary artery plaque cap rupture with subsequent thrombus formation. Because rupture is a mechanical event and the tendency of a plaque to rupture is due in part to increases in the mechanical stresses in the fibrous cap, mechanical analyses are important to understanding plaque stability. Results from mechanical analyses are capable of providing clinically relevant information pertaining to plaque stability assessments.

Histology is the only method capable of identifying plaque features that are associated with vulnerability. Therefore, minimally distorted histologic sections should serve as a basis for constructing the computation models used in mechanical analyses. Further, because substantial longitudinal variations in geometry and mechanical properties often exist in plaques, computational models should be three-dimensional (3-D). Finally, given the complex geometries of atherosclerotic plaques and the fact that they are composed of different materials, the finite element (FE) method should be used to determine the distribution of stress under physiological loading. Until now, a critical need has existed to determine the distribution of stress in 3-D FE models of human coronary atherosclerotic plaques based on minimally distorted histologic sections.

In this research study, a method to measure and correct for distortions caused by acrylic histologic processing was first created. The devised strain-based method yields a limited set of parameters needed for a first order correction. Thus, corrections can be easily implemented using FE methods. Next, a methodology to create 3-D

finite FE models of human coronary atherosclerotic plaques was developed. This methodology accounts for longitudinal variations in geometry and mechanical properties and uses stable acrylic histologic sections as a basis for model construction. Models of plaques, ranging in disease severity, were generated using the developed methodology. Lastly, the distributions of stress in these models were obtained and the effects of some plaque features on stresses were determined.

Results from this study confirm that morphological description of a plaque is not sufficient to predict plaque rupture. The findings suggest that in many cases the 3-D stress field within a plaque must be known in order to assess plaque stability. Finally, the results show that patient specific models must be developed if the 3-D stress field within a plaque is to be determined.

CHAPTER 1:

BACKGROUND

Cardiovascular disease is the leading cause of death in the United States, claiming the lives of 36.3% of the nearly 2.4 million Americans who die each year. Coronary heart disease (CHD) accounts for the majority of deaths from cardiovascular diseases, making it the single largest killer of American males and females. The occurrence of CHD is almost entirely due to atherosclerosis (Rosamond et al., 2007).

Most acute myocardial infarctions, a form of CHD, are caused by atherosclerotic plaque rupture with subsequent thrombus formation rather than stenotic progression (Amarenco et al., 1992; Falk et al., 1995; Fuster, 1994). While the exact mechanism by which a plaque ruptures remains unclear, plaque features, such as a large lipid pool size, a thin fibrous cap, and a high content of inflammatory cells, have been linked to plaque instability. Thus, plaques with a large lipid pool, thin fibrous cap, and large inflammatory cell content are known as vulnerable plaques.

Morphological studies indicate that detection of a vulnerable plaque is not in itself enough to predict rupture. This means not all plaques with a large lipid pool and thin, fibrous cap that is densely infiltrated with inflammatory cells will rupture. Thus, relevant characteristics other than morphological features must be involved.

Plaque rupture is a mechanical event. The tendency of a plaque to rupture is due in part to increases in the mechanical stresses in the fibrous cap (Cheng et al., 1993; Huang et al., 2001; Kilpatrick et al., 2001; Richardson et al., 1989). In order to calculate the distribution of stress in diseased vessels, mechanical models must be developed.

Due to the complex geometries of atherosclerotic plaques and the fact that they are composed of different materials, structural analyses rely on the finite element (FE) method to determine the distribution of stress under physiological loading. As with any mechanical model, finite element models require accurate, detailed geometric data, assignment of mechanical properties, prescription of boundary and loading conditions, and modeling of mechanical processes.

The distribution of stress in two-dimensional (2-D) cross-sections of atherosclerotic plaques has been studied extensively (Beattie et al., 1998; Cheng, et al., 1993; Huang, et al., 2001; Kilpatrick, et al., 2001; Kilpatrick et al., 2002; Lee et al., 1996; Loree et al., 1992; Ohayon et al., 2001; Tang et al., 2004; Veress et al., 1998; Veress et al., 2000; Williamson et al., 2003). However, 2-D models are based on the assumption of plane strain, which is valid only when there are no longitudinal variations in geometry and/or mechanical properties. In reality, this assumption is not always valid and can lead to inaccurate stress predictions, which can in turn lead to inaccurate plaque stability assessments.

Existing three-dimensional (3-D) models (Holzapfel et al., 2005; Holzapfel et al., 2002; Ohayon et al., 2005; Tang, et al., 2004; Vonesh et al., 1997) are limited in that all are based on imaging modalities. Imaging modalities, such as magnetic resonance imaging (MRI) or computed tomography (CT), are not able to identify vulnerable plaques (Burke et al., 2001; Wilensky et al., 2006). Histology is the only technique capable of this. Therefore, in order to determine the distribution of stress in a plaque and correlate plaque features with stress, planar histologic sections must serve as a basis for constructing 3-D computational models. However, a challenge to constructing such

models is that the preparation of slides induces distortions (Carnell et al., 2006; Deverell et al., 1989; Jones et al., 1994; Lowder et al., 2007). Failure to correct for large distortions is likely to result in misrepresentation of the actual stress distribution and to render meaningless any correlation with plaque features.

This research uses the finite element method to determine the 3-D distribution of stresses in human coronary atherosclerotic plaque models based on minimally distorted, serial histologic sections. Correlative relationships between various plaque features, including fibrous cap thickness, lipid content, stenosis severity, and calcification content are also tested for. In this chapter, background information and published research findings relevant to this work are provided.

Atherosclerosis and Its Progression

Atherosclerosis comes from the Greek words "athero" meaning gruel and "sclerosis" meaning hardness. It occurs in large- and medium-sized arteries and involves the accumulation of fat-laden substances, cholesterol, cellular waste products, calcium, and other substances in the inner lining of an artery. This accumulation, called plaque, produces thickening, hardening, and restructuring of the vascular wall (Fuster, 1999; Yutani et al., 1999). Atherosclerosis is a chronic disease that is characterized by chronic inflammation. Inflammation promotes the development and progression of atherosclerosis and also plaque instability (Libby, 2002; Libby et al., 2002; Ross, 1999).

The healthy arterial wall is made up of three layers: the intima, or inner layer, the media, or middle layer, and the adventitia, or outer layer. According to the definition used by most cell biologists, the intima consists of the endothelial cells, the basal lamina, and, in some cases, the subendothelial layer. The subendothelial layer, which is made up

of collagenous bundles, elastic fibrils, smooth muscle cells (SMCs), and possibly fibroblasts, is typically only present in the large elastic arteries, like the human aorta.

The media consists of smooth muscle cells, bundles of collagen fibrils, a network of elastic fibrils, and a varying number of elastic sheets depending on the artery. The media is separated from the adventitia by a layer of elastin. The adventitia consists of collagen fibers, ground substance, and some fibroblasts, macrophages, myelinated nerves, nonmyelinated nerves, and vasa vasorum. Vasa vasorum are blood vessels that perfuse the arterial wall.

Elastin provides elasticity to tissues. Medial elastin is the chief determinant of arterial distensibility. Its polypeptide chains are cross-linked together to form elastic fibers. Collagen primarily serves as a supporting element in the extracellular matrix. It is more rigid and less extensible than most proteins and contains sizable domains of triple-helical conformation. Glycine, proline, and hydroxyproline are its dominant amino acids. Thus far, 12 types of collagen have been identified. Collagen type is dependent on chain composition and degree of glycosylation. The collagen of the basal lamina is Type IV. The collagen in the media and adventitia is mostly Type III, some Type I, and a hint of Type V (Fung, 1993).

The structure of an artery depends on its type. For example, in large arteries, the number of lamellar layers increases with increasing wall thickness. In smaller arteries, the wall thickness to diameter ratio is increased and the elastin is less prominent in the media. As the distance from the aorta increases, eventually, only the inner and outer elastic laminae of an artery can be seen clearly (Fung, 1993).

As a plaque develops, the structure of the arterial wall changes. The exact process by which plaques are initiated and develop remains controversial. Plaque formation tends to occur on the inner curvature of the coronary arteries that contact the heart surface (Friedman et al., 1983). The endothelial cells (ECs) are exposed to low and oscillatory wall shear stress of blood flow which affects their biochemistry and permeability to macromolecules and water (Ku et al., 1985). This, along with the adhesion of molecules and cytokines, may be the major mediator of atherogenesis (Noll, 1998). It has been suggested that loss of medial functional elasticity due to structural alterations of medial elastin increases the possibility of endothelial damage and dysfunction (Avolio et al., 1998). Other studies suggest that the initiation of atherosclerosis is the result of an innate immune system response to the accumulation and modification of lipoproteins in the arterial intima (Hansson et al., 2002). High concentrations of cholesterol in the blood are one of the major risk factors for atherosclerosis. Excessive low-density lipoprotein (LDL) cholesterol concentrations are especially detrimental (Ross, 1999).

The earliest type of atherosclerotic lesion, called the fatty streak, is made-up of foam cells, which are fat-laden macrophages, and T lymphocytes (Libby, 2002). Fatty streak formation is initiated by the accumulation of LDL cholesterol particles in the wall, which leads to chemical alterations of the LDL cholesterol particles. Specifically, the LDL particles undergo oxidation by endothelial cells and SMCs. The oxidized LDL cholesterol particles impair normal endothelial cell function. The particles stimulate endothelial cells causing them to express adhesion molecules on their luminal surfaces. These adhesion molecules attach to monocytes and T lymphocytes circulating in the blood. The modified LDLs also stimulate the endothelial cells to secrete chemokines,

chemicals that attract the attached monocytes and T lymphocytes into the intimal layer of the artery wall. In the intima, continued inflammation results in upregulation of moncyte-derived macrophages and T lymphocytes. Macropahages do not readily take up LDL cholesterol to form foam cells. Instead, oxidized LDL cholesterol particles bind to macrophage scavenger receptors and are then ingested.

With the progression of disease, macrophages, endothelial cells, and SMCs, secrete cytokines and growth factors that encourage the migration and proliferation of SMCs. Inflammatory stimulation causes medial SMCs to secrete enzymes that degrade elastin and collagen. This degradation allows the SMCS to penetrate through the elastic laminae and collagenous matrix of the growing plaque (Libby, et al., 2002). In an attempt to provide the artery with sufficient strength to withstand mechanical loads, the migrated SMCs of the atherosclerotic lesion synthesize and organize extracellular matrix proteins. SMCs are the main source of the fibrous cap's extracellular matrix, especially the tough Type I and III collagens that supply the greatest stiffness to the fibrous cap, and elastin, which provides elasticity (Lee and Libby, 1997). Such production is essential for the formation of a fibrous cap.

As disease continues to progress, inflammatory cells secrete tissue factor, a potent thrombogenic agent, and lytic enzymes, which weaken the fibrous cap. The exact mechanism of plaque rupture is unknown. However, the clinical implications of rupture are well understood. If rupture of the fibrous cap occurs, the lipid core is exposed to flowing blood. This exposure initiates thrombus formation, which may lead to acute coronary syndromes, such as unstable angina and acute myocardial infarction (Arroyo

and Lee, 1999). One study suggests that approximately 60% of myocardial infarctions are caused by rupture of plaques with subsequent thrombus formation (Casscells et al., 2003).

In some cases the thrombus may be resorbed. This causes a healing response that leads to increased collagen accumulation and SMC growth. The plaque can continue to evolve into a calcified plaque. The cores of these plaques contain deposits of calcium hydroxapatite embedded in the collagen and elastin matrix. New blood vessels may also be present (Weissberg, 2000). Such advanced plaques may cause significant stenosis and produce symptoms of stable angina pectoris.

While plaque rupture is clearly important, it is not the only cause of thrombus formation. In advanced plaques, superficial erosion of the endothelial layer may lead to thrombus formation. Here again, clot formation can subsequently result in unstable angina or acute myocardial infarction (Libby, 2001).

Positive remodeling, or compensatory enlargement, is defined as the enlargement of an artery in association with plaque accumulation in order to maintain an adequate, if not normal, lumen area. The concept of positive remodeling was first introduced by Glagov and colleagues (1987) based on analysis of histopathologic data from 136 hearts obtained at autopsy. They found that in coronary arteries, narrowing of the lumen only occurs once the lesion occupies greater than 40% of the internal elastic lamina area. Cross-sectional in vivo intravascular ultrasound (IVUS) studies at a single time point have confirmed these findings (Hermiller et al., 1993; Losordo et al., 1994). The explanation for this adaptive change is unknown. However, Glagov and colleagues (1987) suggested that since plaques are usually eccentric this change may be the result of the

effect of the plaque on the underlying wall or of altered flow velocity on the uninvolved segment opposite the plaque.

Plaque Classification

Morphological features of a plaque have been used for classification purposes. A classification scheme was first proposed by the American Heart Association (AHA) (Stary et al., 1995; Stary et al., 1994). The AHA classification scheme is given in Figure 1.1.

Nomenclature	Main Histology	Main growth mechanism	Sequences in progression
Type I (initial) lesion	Isolated macrophage foam cells	Lipid accumulation	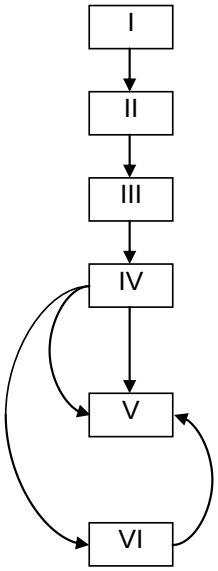
Type II (fatty streak) lesion	Mainly intracellular lipid accumulation	Lipid accumulation	
Type III (intermediate) lesion	Type II changes and small extracellular lipid pools	Lipid accumulation	
Type IV (atheroma) lesion	Type II changes and core of extracellular lipid	Lipid accumulation	
Type V (fibroatheroma) lesion	Lipid core and fibrotic layer, or multiple lipid cores and fibrotic layers, or mainly calcific, or mainly fibrotic	Accelerated smooth muscle and collagen increase	
Type VI (complicated) lesion	Surface defect, hematoma-hemorrhage, thrombus	Thrombus, hematoma	

Figure 1.1. AHA classification scheme for atherosclerotic plaques. Figure modified from Stary, et al. (1995).

Virmani and colleagues (2000) suggest that AHA scheme is difficult to use for two reasons. First, it is difficult to remember because it relies on a long list of roman numerals modified by letter codes. Second, it is misleading in that it implies that there is

an orderly, linear pattern of lesion progression. Virmani and colleagues therefore devised a simpler classification scheme that is consistent with the AHA categories, but is easier to use. The scheme was termed the "modified AHA classification" and is given in Table 1.1.

Table 1.1. Modified AHA classification scheme for atherosclerotic plaques. Table modified from Virmani, et al. (2000).

Nomenclature	Main Histology	Thrombus
Nonatherosclerotic intimal lesions		
Intimal thickening	Normal accumulation of smooth muscle cells in intima	Absent
Intimal xanthoma, or "fatty streak"	Luminal accumulation of foam cells	Absent
Progressive atherosclerotic lesions		
Pathological intimal thickening	Smooth muscle cells in a proteoglycan-rich matrix with areas of extracellular lipid accumulation without necrosis	Absent
Erosion	Luminal thrombosis; plaque same as above	Thrombus mostly mural and infrequently occlusive
Fibrous cap atheroma	Well-formed necrotic core with an overlying fibrous cap	Absent
Erosion	Luminal thrombosis; plaque same as above; no communication of thrombus with necrotic core	Thrombus mostly mural and infrequently occlusive
Thin fibrous cap atheroma	Thin fibrous cap infiltrated by macrophages and lymphocytes with rare smooth muscle cells and an underlying necrotic core	Absent; may contain intraplaque hemorrhage/fibrin
Plaque rupture	Fibroatheroma with cap disruption; luminal thrombus communicates with the underlying necrotic core	Thrombus usually occlusive
Fibrocalcific plaque	Collagen-rich plaque with significant stenosis usually contains large areas of calcification with few inflammatory cells; a necrotic core may be present	Absent

Plaque Features and Stability

In the past, morphological studies have been conducted to determine whether various features are consistently present in ruptured plaques. Results suggest that certain features, including a thin, fibrous cap, large lipid pool, and high inflammatory cell

content, are consistently present in ruptured plaques. Other features which are associated with the most advanced lesions types, including high stenosis severity and high calcification content, cannot be linked to rupture.

Fibrous Cap Thickness

Fibrous cap thickness is a morphological characteristic specifically associated with plaque rupture. Based on a study analyzing the hearts of 113 men with coronary disease who died suddenly, a cap thickness of 65 μm has been defined as a criterion of instability (Burke et al., 1997). This criterion was chosen because in plaques that ruptured the mean cap thickness was 23 ± 19 μm and 95% of caps measured less than 64 μm within a limit of only two standard deviations.

Still, the presence of a thin, fibrous cap is not sufficient to predict rupture. In a study examining over 200 sudden death cases, approximately 120 patients (60%) died of acute thrombi which resulted from the rupture of thin fibrous caps. In 70 % of these 120 patients, thin fibrous caps, which were not ruptured, were found (Virmani, et al., 2000). In 30% of the remaining 80 patients, whose death was not associated plaque rupture, thin, fibrous caps were present (Farb et al., 1996). Similarly, in a detailed autopsy study of coronary arteries from 54 men who died after having stable angina for more than 2 years, 40% of the 448 plaques analyzed had thin, fibrous caps that were rupture-free (Hangartner et al., 1986). Thus, not all plaques with thin, fibrous caps rupture.

Lipid Content

Lipid content is another morphological characteristic specifically associated with plaque rupture. Observations have shown that lipid-rich lesions are more likely to

rupture and cause myocardial infarctions than lipid-poor lesions (Davies, 1990; Richardson, et al., 1989). This is in part because lipid is a potent thrombogenic agent (Wilcox, 1992). Ruptured plaques have significantly higher lipid content than do plaques with thick, fibrous caps. However, no significant difference in lipid content has been observed between plaques with thin, fibrous caps and ruptured plaques (Virmani et al., 2005). Thus, not all plaques with large lipid pools rupture.

Inflammatory Cell Content

Inflammation in coronary arteries has also been implicated as a contributing destabilizing factor (Biasucci et al., 2000; Falk, 1989; Libby, 1995; Moreno et al., 1994). Atherosclerotic lesions often contain a prominent accumulation of inflammatory cells, including macrophages (Falk, et al., 1995; Libby, 1995; Moreno, et al., 1994). The macrophage is the principal inflammatory cell of an atherosclerotic plaque. These cells densely infiltrate the thin, fibrous caps of most ruptured plaques (Virmani, et al., 2000). Macrophage content also correlates positively with lipid content (Bezerra et al., 2001).

Macrophages have been shown to release lytic enzymes, including matrix metalloproteinases (MMPs), capable of weakening the fibrous cap and increasing its susceptibility to rupture (Lee, 2000; Newby and Zaltsman, 1999; Welgus et al., 1990). Stromelysin (MMP-3), interstitial collagenase (MMP-1), and gelatinase (MMP-9) are all upregulated in atherosclerotic plaques (Galis et al., 1994; Henney et al., 1991; Nikkari et al., 1995). Although matrix degradation promotes plaque instability, it has been suggested that impaired cap formation due to SMC aging, mummification, and apoptosis may be as important as increased cap degradation in promoting plaque rupture (Newby

and Zaltsman, 1999). Therefore, quantification of inflammatory cell content alone is not sufficient to predict rupture.

Stenosis Severity

The percentage of stenosis in an artery is calculated by dividing the lesion area by the internal elastic lamina area (the lesion area plus the luminal area). While some myocardial infarctions are caused by stenotic progression, the majority are not. Although intimal inflammation increases with increased stenosis severity (Baroldi et al., 1988), angiographic studies have demonstrated that most lesions responsible for myocardial infarction are minimally occlusive (< 50% stenosis) prior to the clinical event (Giroud et al., 1992; Little et al., 1988). A minimal degree of stenosis does not, however, equate to a small plaque area. IVUS studies have shown that segments of coronary arteries that are angiographically normal may contain large plaques (St Goar et al., 1992; Tuzcu et al., 1995).

Recall that positive remodeling of the outer layers of the arterial wall allows for plaque development without narrowing the lumen. Although positive remodeling is advantageous in terms of preventing luminal stenosis, it is also thought of as harmful. Increases in the extent of positive remodeling have been linked to increases in plaque vulnerability. Plaques with positive remodeling, compared to plaques with vessel shrinkage (negative remodeling), have larger lipid cores and higher macrophage contents (Pasterkamp et al., 1998; Schoenhagen et al., 2000; Varnava et al., 2002). Further examinations into the causes of instability in plaques that have undergone positive remodeling while remaining minimally stenosed are warranted.

Calcification Content

Autopsy studies have shown that coronary artery calcification is an excellent marker for the presence of atherosclerotic plaque (McCarthy and Palmer, 1974; Rifkin et al., 1979). Calcification content is strongly correlated with stenosis severity (Burke, et al., 2001; Kragel et al., 1989) and plaque burden, which is defined as the vessel area (media area plus lesion area) divided by the vessel area plus the luminal area (Burke, et al., 2001; Rumberger et al., 1995; Taylor et al., 2000). Increased plaque burden is associated with an increase in coronary events (Falk, et al., 1995). In concurrence, studies have shown that calcification content is an independent predictor of subsequent coronary events (Detrano et al., 1996; Pletcher et al., 2004; Raggi et al., 2000).

While the presence of calcification is indicative of atherosclerosis, morphological data from coronary arteries obtained at autopsy suggest that calcification content is not associated with plaque instability. Ruptured plaques have relatively low amounts of calcification. Further, plaques with thin, fibrous caps have widely varying amounts of calcification (Burke, et al., 2001). Calcification content correlates negatively with inflammatory cell content (Shaalan et al., 2004). More work is needed to elucidate the relationship between calcification content and plaque stability.

Mechanical Stresses and Stability

Plaque rupture is a mechanical event. Evidence supports the finding that the tendency of a plaque to rupture is due in part to increases in the mechanical stresses in the fibrous cap. Various studies have revealed that plaque rupture typically occurs in the shoulder regions of plaques (Ohayon, et al., 2001; Richardson, et al., 1989). Stress concentrations occur in the shoulder regions of plaques due to large differences in

stiffness between the fibrous cap and underlying lipid pool (Cheng, et al., 1993; Huang, et al., 2001; Richardson, et al., 1989).

In order to calculate the stress in a diseased artery, mechanical models must be developed. There are five key steps associated with the development of any mechanical model. These include modeling of geometry, loads and boundary conditions, mechanical properties, and mechanical processes.

Due to the complex geometries of atherosclerotic plaques and the fact that they are composed of different materials, the finite element method is used to determine the distribution of stress under physiological loading in mechanical models. With this method a geometrically complex domain is represented by a collection of geometrically simple subdomains, called finite elements, so that it is possible to approximate the solution of a problem over each element (Reddy, 1993). Any geometrical shape that provides necessary relationships among the values of the solution at selected points, called nodes, qualifies as a finite element. Finite element models may be 2-D or 3-D. In 2-D models, only in-plane nodal displacements may occur, whereas in 3-D models nodes may displace in up to three directions.

Three-dimensional FE models of atherosclerotic plaques more accurately predict the distribution of stress in diseased vessels than do 2-D models. Two-dimensional models are based on the assumption of plane strain, which is valid only when there are no longitudinal variations in geometry and/or mechanical properties. In reality, this assumption is not always valid and can lead to inaccurate stress predictions.

Based on morphological data, not all plaques with thin, fibrous caps and large lipid pools should have high stresses. Two-dimensional models may not be able to arrive

at this result due to the assumption of plane strain. Thus, 3-D models must be developed if a mechanical explanation is to be provided.

Need for Histology

Histology is the only technique capable of identifying vulnerable plaques. Recall that these plaques are defined as ones with large lipid pools and thin (<65 μm thick), fibrous caps, which are densely infiltrated with inflammatory cells. Imaging techniques are not currently able to detect such plaques.

Coronary angiography is an established imaging technique used to visualize atherosclerotic disease. However, its value as a diagnostic tool is limited. In addition to having a low sensitivity for identifying plaques in the presence of positive remodeling (plaque development without narrowing of the lumen) and diffuse disease, angiography yields 2-D images capable of depicting only the size of arterial openings (Low et al., 2006).

In recent years, techniques attempting to identify plaque constituents have been introduced. Some techniques, including IVUS, MRI, multi-detector row computed tomography (MDCT), and optical coherence tomography (OCT) are already being used to image diseased coronary arteries in patients. However, each of these techniques has critical shortcomings.

Although MRI can be used to detect plaque constituents in carotid arteries, in deeper-lying coronary arteries MRI suffers from a low signal-to-noise ratio and subsequently low resolution images (Wilensky, et al., 2006). Similarly, while IVUS can be used to obtain the thickness and echogenicity of arterial wall structures, the current-

generation of catheters give rise to low resolution images (Saia et al., 2006). MRI (spatial resolution of 800 μm) and IVUS (spatial resolution of 100 μm) cannot identify thin, fibrous caps much less biological markers of disease.

MDCT can provide coronary calcification scores. However, as shall be discussed later, such scores reflect plaque burden, defined as the vessel area (media area plus lesion area) divided by the vessel area plus the luminal area, as it relates to healed plaque ruptures and/or positive remodeling (Burke et al., 2003; Schmermund and Erbel, 2001). In addition, assessment of non-calcified components using contrast-enhanced MDCT is unreliable because the Hounsfield units of the components within an individual plaque may overlap (Achenbach et al., 2004). The spatial resolution of MDCT (600 μm) highlights yet another of its limitations. OCT has a spatial resolution of 10 μm and can be used to measure thin fibrous caps (Kukreja et al., 2006) but cannot be used to identify inflammatory cells. Additionally, misclassification of lesions can occur due to OCT's limited depth penetration (2 mm) and inability to distinguish calcium deposits from lipid pools (Manfrini et al., 2006).

Ex vivo studies using MRI (Nikolaou et al., 2004; Worthley et al., 2000), IVUS (Murashige et al., 2005; Nair et al., 2001; Nair et al., 2002), MDCT (Becker et al., 2003; Nikolaou, et al., 2004), and OCT (Brezinski et al., 1996; Jang et al., 2002; Patwari et al., 2000; Yabushita et al., 2002), offer superior resolution compared to in vivo studies. However, in such studies, histology must be used to validate the imaging results.

Histology remains the ex vivo gold standard for identifying lesion constituents and biological markers of disease in atherosclerotic coronary arteries. Achieving a spatial resolution below 65 μm is not problematic. In addition, stains allow constituents

and biological markers of disease to be identified with confidence. Histology is the only way to detect vulnerable plaques. Therefore, in order to determine the distribution of stress in plaques, histologic sections must be used to construct 3-D mechanical models.

Histologic Related Distortions

A challenge to constructing 3-D models from serial histologic sections is that the preparation of slides, including fixation, dehydration, clearing, infiltration, embedding, sectioning, and staining, induces distortions in the tissue (Carnell, et al., 2006; Deverell, et al., 1989; Jones, et al., 1994; Lowder, et al., 2007).

Fixation and subsequent dehydration and embedding change tissue volume. For example, tissues fixed in formaldehyde and embedded in paraffin shrink by approximately 33% (Bancroft and Gamble, 2002). Actually, the extent of the distortions varies between tissue types and is also dependent upon the processing protocol. In the case of arteries, the literature is not in agreement as to the exact effects. One study found that fixation in formalin at zero transmural pressure caused significant swelling in thoracic porcine aortas. In the same study, these changes were not found when the arteries were pressure fixed in formalin and stretched (Wilhjelm et al., 1997). Another study found that fixation and stretching of pressurized aortic arteries resulted in a significant decrease in artery diameter (Wolinsky and Glagov, 1967). In human femoral arteries that were not pressurized, formalin fixation resulted in a significant decrease in artery size in noncalcified arteries but not in calcified arteries (Park et al., 1993). Yet in non-pressurized human atherosclerotic carotid arteries, formalin fixation caused significant increases in size (Dalager-Pedersen et al., 1999).

The reported effects of processing and embedding likewise vary. In one study, the luminal area of human coronary arteries shrunk by 65% due to formalin fixation, processing, and embedding in paraffin (Falk, 1982). In another, the luminal area of human coronary arteries with minimal atherosclerosis decreased by only 8% due to formalin fixation, processing, and embedding in paraffin and did not change at all in arteries with moderate to severe atherosclerosis (Siegel et al., 1985). One study has reported the effects of processing and embedding arteries in acrylic. This study found that fixation in formalin, processing, and embedding in paraffin caused a 19% shrinkage in cross-sectional area whereas fixation in formalin and embedding in acrylic, in this case glycol methacrylate (GMA), caused no significant changes in cross-sectional area in canine carotid and femoral arteries. This is likely because the techniques used for infiltration and embedding with GMA require no alcohol-dehydration phase (Dorbin, 1996).

Sectioning induced distortion has also been shown to depend on tissue type and embedding media (Deverell, et al., 1989; Jones, et al., 1994). Unfortunately, neither of these studies examined arterial tissue. Still, it has been shown that sectioning and staining of human iliac arteries embedded in paraffin resulted in an 11% decrease in arterial diameter (LeVeen et al., 1983).

While the occurrence of distortions due to histologic preparation has long been recognized, little attention has been devoted to addressing this problem when 3-D models are constructed based on histologic sections. This is probably due to the difficulty associated with measuring and correcting for such distortions. However, failure to

account for these distortions may result in misrepresentation of the actual stress distribution.

Methyl Methacrylate

Paraffin wax is the most popular histologic embedding medium because it is the most inexpensive, easily handled, and easily sectioned medium (Bancroft and Gamble, 2002). However, as has been discussed, the effects of geometric distortions caused by histologic preparation can be minimized by embedding in acrylic as opposed to paraffin (Dorbin, 1996). Recall that in the Dorbin study, the acrylic embedding media used was GMA. However, previous work in our laboratory has shown that immunostaining of GMA embedded arteries is limited. This is because GMA, which cannot be removed from the tissue following embedding, is too dense to be effectively penetrated by immunological stains. Methyl methacrylate (MMA) is an acrylic that can be removed.

As with any acrylic medium, MMA allows sections to be cut without eliminating tissue calcium. This is because acrylic and calcification are of comparable stiffness. In paraffin, adequate stabilization of calcified tissues is not achieved. Samples must therefore be decalcified prior to embedding in paraffin. However, decalcification is undesirable because it compromises morphological detail (Islam and Frisch, 1985). In MMA sections, deformations in tissues surrounding calcification are negligible. Furthermore, because MMA sections are much stiffer than paraffin sections, folding of sections is not as problematic in MMA as it is in paraffin. Work is needed to quantify the distortions that occur as a result of MMA embedding. In addition, the effect of such distortions on stresses should also be determined.

Mechanical Properties of Arterial Tissue

Quantifying the mechanical properties of healthy and diseased arterial tissue is essential for developing a better understanding of their physiology and pathophysiology. As reported in various text books and review articles (Fung, 1993; Humphrey, 2002; Vito and Dixon, 2003)**,** experimentation in healthy tissue has shown that arteries are heterogeneous, non-linear, and anisotropic. They are viscoelastic in that they exhibit stress relaxation, creep, and hysteresis. They are treated as incompressible if fluid movement through and out of the arterial wall are neglected. Arteries are relatively insensitive to the rate of strain imposed and act differently in smooth muscle cell inactive and active states. In addition, residual stress and strain are present in arteries. The stiffness of arteries increases with aging because the ratio of collagen to elastin steadily increases as does the degree of collagen cross-linking (Valenta et al., 2002). Women exhibit a greater age-related rise in arterial stiffness than do men (Waddell et al., 2001).

While there is extensive literature on atherosclerotic pathogenesis, the role of hemodynamics, histopathology, and clinical treatment, little attention has been devoted to the determination of atherosclerotic plaque mechanical properties. It has been suggested that this lack of data is probably the most uncertain aspect in the existing literature on plaque rupture (Richardson, 2002).

Some experimental studies have sought to determine the mechanical properties of atherosclerotic plaques. These studies can be divided into two types. The first type is used to determine the mechanical properties of individual constituents. The second is used to determine the mechanical properties of entire plaques.

Many of the earliest studies focused on determining the properties of the plaque cap which was isolated from the plaque core and vessel. In the first work of this kind, Lee and colleagues (1991) conducted mechanical tests on atherosclerotic plaque caps from human abdominal aortas. A static load which produced a compressive stress normal to the surface of the plaque was applied to simulate the radial stresses experienced by the arterial wall. After allowing the caps to creep for 30 minutes, a dynamic stress amplitude with a varying frequency was superimposed on the initial stress. Results showed that the stiffness of the fibrous caps was related to the underlying histologic structure (calcified caps were stiffer than cellular caps and hypocellular caps were stiffer than cellular caps) and that for all histologic classes the stiffness increased with increasing frequency of stress. The relevance of the reported dynamic compressive stiffness is limited given the stress-strain behavior is non-linear and thus the stiffness values depend on the applied load or displacement where the stiffness is measured. In addition, compression testing does not account for tissue anisotropy nor can it be used to obtain the more physiologically relevant circumferential properties of the plaque.

Suggesting that commercially available tensometers are unsuitable because they are used to study specimens much larger than an atherosclerotic plaque, Lendon et al. (1993) custom-built a tensometer to study the stress-strain relationships of small connective tissue specimens, typically 7mm x 1.5mm. They tested rectangular strips of human aortic ulcerated and non-ulcerated plaque caps in circumferential tension. To distribute the applied load more uniformly, the ends were widened for clamping by attaching squares of paper to the strips. Wide variations in stress-strain relationships between the ulcerated and non-ulcerated plaque caps were reported. Loree et al. (1994a)

studied the effects of plaque structure and applied tensile stress on the static circumferential tangential modulus. Human aorta intimal plaques were preconditioned prior to quasistatic tensile loading to failure. In contrast to the radial compressive modulus, the static circumferential tangential modulus was not significantly affected by the degree of cellularity and calcification.

More work by Loree and colleagues (1994b) analyzed the effect of changes in lipid composition on the mechanical properties of lipid pools. The dynamic shear modulus of model lipid pools (made up of mixtures of cholesterol monohydrate, phospholipid, and triglyceride) was measured using a torsion rheometer. The stiffness of the lipid pool was shown to depend on the concentration of cholesterol monohydrate crystals.

In our laboratory, Beattie et al. (1998) was the first to determine mechanical properties based on transmural deformation of whole, human atherosclerotic segments under biaxial, physiologic loading. Briefly, they coupled FE analyses with experimental data to determine the material properties of constituents in intact cross-sections of atherosclerotic human aortas. Hundreds of particles were air-brushed onto arterial cross-sections. A mechanical testing apparatus was then used to measure the positions of the particles at various pressures and to measure the radial deformation. Optimization methods were used to determine the material properties in the FEM which best fit the experimental data. Results revealed that the material properties of the lipid, fibrous tissue, calcification, and healthy tissue differ by orders of magnitude and are well characterized by bi-linear, three parameter models, where the parameters are the strain breakpoint, the initial modulus, and the modulus for strains exceeding the break point.

To test segments of whole human atherosclerotic aortoiliac artery, Topoleski et al. (1997) custom-built an experimental system that was fully computer controlled and had a broad range of loading conditions. Incorporated into the system was a temperature-controlled physiologic specimen bath. Uniaxial radial cyclic compressive testing revealed plaques display composition and history dependant nonlinear and inelastic responses under finite deformations. Using the same methods, it was shown that plaques exhibit significant composition dependent stress relaxation responses (Salunke et al., 2001) and that calcified plaques are distinctly different from other plaque types in terms of their maximum compressive stretch and hysteresis area (Topoleski and Salunke, 2000).

More recently, Holzapfel et al.(2004) tested human atherosclerotic iliac arteries to measure ultimate tensile stresses and stretches. Prepared arterial strips taken along the plaque underwent cyclic quasistatic uniaxial tension tests in the axial and circumferential directions. Results from individual samples revealed anisotropic and highly nonlinear tissue properties and substantial interspecimen differences.

Finite Element Models of Atherosclerotic Plaques

The finite element method has been used to analyze stress distributions within diseased arteries to provide insight into possible mechanisms of plaque rupture. Typically, simplifications of the true behavior are implemented in models examining the relationship between stress and strain fields in both healthy and diseased arteries. In the context of atherosclerotic vessels, various simplified models have been utilized including orthotropic linear (Loree, et al., 1992), isotropic bilinear (Beattie, et al., 1998; Kilpatrick, et al., 2001; Kilpatrick, et al., 2002), isotropic linear (Chau et al., 2004; Huang, et al.,

2001; Lee, et al., 1996), transversely isotropic linear (Cheng, et al., 1993; Ohayon, et al., 2001), isotropic nonlinear (Tang, et al., 2004), and isotropic nonlinear with residual strains (Williamson, et al., 2003). While such models do not account for the true mechanical properties of arterial tissue, important information is still provided even when simplifications are incorporated.

Two-Dimensional Analyses

Numerous studies have examined the distribution of stress in planar cross-sections of atherosclerotic vessels. The earliest study was based on idealized cross sections of diseased vessels (Loree, et al., 1992). This study examined the effects of stenosis severity and subintimal plaque structural features on the distribution of stress and found that decreasing the fibrous cap thickness considerably increased the peak circumferential stress, whereas increasing the stenosis severity decreased peak stress. It was suggested that these results explain why some plaques that rupture are not angiographically severe.

In a study by Cheng and colleagues (1993), the location of peak stress in ruptured atherosclerotic lesions was determined. Most plaque ruptures occurred very close to a region of high stress. However, the peak stress did not always coincide with the rupture site. As was acknowledged, it is possible that had the plane strain assumption not been utilized, peak stress and rupture site may have coincided.

Another study using heterogeneous, human atherosclerotic aortas found that the distributions of stress and strain energy were strongly influenced by lesion structure and composition suggesting that accounting for heterogeneities in mechanical analyses is of critical importance in the effort to link lesion morphology to susceptibility of plaques to rupture (Beattie, et al., 1998). An investigation in which diseased human carotid

endarterectomy specimens were used, likewise confirmed that the stress distribution within a lesion is highly nonuniform and directly dependant on lesion structure. In the parametric modeling studies of that investigation, a necrotic lipid core to calcification transition lowered the peak fibrous cap stress, while a transition from calcification to necrotic lipid core increased it. From a clinical standpoint, these results emphasize the need for diagnostic imaging modalities capable of identifying histologic features in plaques (Kilpatrick, et al., 2001).

Other studies have inspected the effect of distinct features on mechanical behavior in arteries. Finet et al. found that irrespective of plaque geometry and composition, a fibrous cap thickness of less than 60 μm results in stresses greater than 300 kPa. In vivo testing has shown that human atherosclerotic plaques fracture under such stresses (Lendon et al., 1991). Recall, however, that morphological data suggests that not all plaques with thin, fibrous caps should have high stresses.

Huang et al. (2001) found that, in human atherosclerotic coronary arteries, calcification does not decrease the stability of the plaque. This is in contrast to lipid pools, which drastically increase maximum stresses. However, Veress et al. (2000) found that, in idealized models of the same types of arteries, the location of calcification matters. While calcium deep in the lesion has little effect on stability, calcium near the surface promotes instability by increasing the shoulder stress and creating stress concentrations in the cap. Additional studies are needed to elucidate the effect of calcification on plaque stresses.

Lee et al. (1996) demonstrated the existence of a correlation between high circumferential stress regions and MMP-1 expression in human atherosclerotic coronary

arteries. The authors believe that weakening of the collagenous extracellular matrix at high stress regions may contribute to the pathogenesis of plaque rupture. Similarly, Kilpatrick et al.(2002) noted that strain, stress, and strain energy in MMP-1 regions in human atherosclerotic aortas correlated with lipid accumulation.

Idealized models of human coronary plaques were used to determine if age-related factors impact the stability of plaques. Results revealed that increases in stress are closely associated with decreases in the load-bearing capability of the lipid pools that develops with age (Veress, et al., 1998).

Williamson et al. (2003) analyzed the sensitivity of wall stresses in diseased human coronary arteries to variable material properties. They showed that stresses in the artery have low sensitivities for variation in elastic modulus and that such sensitivities are comparable between isotropic nonlinear, isotropic nonlinear with residual strains, and transversely isotropic linear models. However, they also showed that predictions in regions of stress concentration are more sensitive to the specific model used and can vary by up to 30% depending on the models.

Many of the discussed studies have relied on geometry from paraffin cross-sections to study stress distributions (Beattie, et al., 1998; Cheng, et al., 1993; Huang, et al., 2001; Kilpatrick, et al., 2002; Lee, et al., 1996; Tang, et al., 2004). Acrylic cross-sections have not been used, although Dobrin (1996) suggests that it is preferable to do so in order to minimize the effects of geometric distortions.

Some work has focused on the use of imaging techniques as bases for FE analyses. In one study, FE analysis based on pre-angioplasty IVUS images of human atherosclerotic coronary arteries was used to predict in-vivo plaque rupture sites.

Circumferential peak stress was shown to coincide with rupture locations on postangioplasty IVUS images (Ohayon, et al., 2001). In another study, stress and strain distributions computed from FE modeling based on OCT images were compared to those from modeling based on histologic images. While the magnitude of the maximum stress was higher in the histologic based model, the distribution of stress and strain between the two models was comparable (Chau, et al., 2004). In a similar investigation using human atherosclerotic carotids, MRI based FE model was compared to a histologic based model. Analyses comparing the stress distributions were not presented. However, the maximum and minimum stress values from the histologic based model were 28% and 69% higher than from the MRI based model respectively. These discrepancies were attributed to deformations in the histologic cross-sections caused by fixation (Tang, et al., 2004). While 2-D modeling served as a good starting point, as mentioned, results from 2-D models are inaccurate in cases in which even moderate longitudinal variations in geometry and mechanical properties are present. Three-dimensional models should therefore be developed.

Three-Dimensional Analyses

The development of 3-D FE models of atherosclerotic arteries has been reported in a few studies. Only the most recent (Ohayon, et al., 2005) examined stresses in a single diseased, human coronary artery. Mechanical analyses of these arteries are particularly relevant given plaque rupture and subsequent thrombus formation is responsible for the majority of myocardial infarctions. Imaging techniques were used to develop each of the existing 3-D models.

Using 3-D IVUS with FE analyses, Vonesh and colleagues (1997) developed a method to estimate the regional distribution of elasticity in human iliac and femoral arteries. Finite element models were created using 3-D IVUS reconstructions. An initial elastic modulus was assumed and the initial deformation due to pressure loading was computed. The error between the predicted deformation from the FEA and the actual deformation from IVUS images was calculated. To obtain the optimal elastic modulus, an optimization program was used to scale the assumed elastic modulus and minimize the displacement error. Results showed that the optimal elastic modulus for nondiseased tissue was statistically different from that for atherosclerotic tissue for both normotensive and hypertensive pressurization. Other studies have used MR images to develop 3-D FE models of atherosclerotic iliac arteries to simulate balloon angioplasty or study the interaction of arteries with stents (Holzapfel, et al., 2005; Holzapfel, et al., 2002).

Tang et al. (2004) developed a single 3-D fluid-structure interaction model from 3-D ex vivo MR images of a human atherosclerotic carotid artery. The 3-D geometry of the plaque was reconstructed from 64 MR images and a computational mesh was generated using the Visualization Toolkit (Schroeder et al., 1998). Simulations were conducted using the 3D FSI model under various steady and pulsating pressure conditions. Results indicated that pulsating pressure led to large cyclic stress and strain variations in the plaque cap. Tang and colleagues suggested such variations may lead to fatigue and possible plaque rupture. Additionally, in the same study, a single 2-D solid only model was developed and compared to the corresponding axial section of a 3-D solid only model. Stress results were overestimated in the 2-D model compared to the 3-D model.

In a more recent study, in vivo IVUS imagining of a human coronary atherosclerotic plaque was used to create a 3-D FE model to predict plaque rupture location (Ohayon, et al., 2005). Based on appearance, contours delimiting the lumen border, media, dense fibrosis, and cellular fibrosis were manually traced on 17 IVUS cross-sectional images obtained prior to angioplasty. Finite element analysis was performed on 2-D models developed from each of the 17 obtained segmentations. Additionally, FE analysis was performed on a 3-D model that was developed by piling up the segmentations following the trajectory of the center catheter. Plaque rupture was triggered using balloon angioplasty and rupture location was determined using post-angioplasty IVUS images. Results showed that peak stress and rupture location coincided in the 3-D model, but not in the 2-D models. Compared to the 3-D analysis, 2-D analyses consistently overestimated the magnitude of stress.

The works of Tang et al. and Ohayon et al. highlight the appropriateness of incorporating longitudinal variations. However, there is an obvious limitation associated with these studies. The models were based on MRI and IVUS images, which means that a thin fibrous cap could not be identified. Thus, a plaque which was not in danger of rupturing could have been analyzed.

To the best of our knowledge, all existing 3-D models are limited in that they are based on imaging modalities rather than histology. As discussed, imaging modalities are not able to identify vulnerable plaques. Three-dimensional models based on histologic sections are needed.

CHAPTER 2:

RESEARCH OBJECTIVES

Cardiovascular disease is the leading cause of death in the United States (Rosamond, et al., 2007). Most acute myocardial infarctions, a form of cardiovascular disease, are caused by coronary artery atherosclerotic plaque rupture with subsequent thrombus formation (Amarenco, et al., 1992). Because rupture is a mechanical event and the tendency of a plaque to rupture is due to increases in the mechanical stresses in the fibrous cap, mechanical analyses are important to understanding plaque stability. Results from mechanical analyses are capable of providing clinically relevant information pertaining to plaque stability assessments. A critical need exists to develop three-dimensional (3-D) mechanical models of human coronary atherosclerotic plaques based on minimally distorted histologic sections and to determine if correlations between stress results from these models and plaque features exist. Thus, the following central hypothesis of this research project was formulated:

Hypothesis

Stress results from morphologically correct, three-dimensional mechanical models of human coronary atherosclerotic plaques will provide additional insights related to the assessment of plaque stability.

To test this hypothesis, the following three specific aims were developed:

Specific Aim I

Quantify and correct for histologic distortions to achieve more accurate mechanical models of arteries.

To the best of our knowledge, histology is the only method capable of identifying plaque features that are associated with vulnerability. A challenge to constructing mechanical models based on histologic sections is that the preparation of slides induces distortions. Failure to correct for such distortions may result in misrepresentation of the actual stress distribution, render meaningless any correlation with plaque features, and lead to inaccurate plaque stability assessments. Previous work has suggested that it is preferable to embed in acrylic, more specifically glycol methacrylate (GMA), in order to minimize distortions. However, immunostaining of GMA embedded samples is limited, because GMA cannot be removed from the tissue following embedding. Methyl methacrylate (MMA) is an acrylic that can be removed.

In this work, a unique, strain-based approach to measuring and correcting for distortions in arteries embedded in MMA was developed. Micro-computed tomography was used to image arteries in the fresh and embedded states. Tissue blocks were sectioned, stained and imaged using a light microscope. Each section contained four registration marks used to determine strains introduced by sectioning and staining. Using these three image sets, geometric models were generated and distortions were measured. A uniform, equibiaxial area dilatation was applied to correct for shrinkage distortions and uniform strains were applied to correct for sectioning distortions. Because MMA, a less commonly used embedding media than paraffin, was used in this study, a comparison

between the effects of preparation related distortions on stresses in acrylic versus paraffin histologic sections is provided.

Specific Aim II

Develop three-dimensional mechanical models of human coronary atherosclerotic plaques based on minimally distorted histologic sections.

Although two-dimensional (2-D) mechanical models of atherosclerotic plaques are abundant, data acquired from such models may be inaccurate due to the assumption of plane strain and the use of paraffin cross-sections as bases for model development. Existing 3-D models are limited in that all are based on imaging modalities rather than on histology. Additionally, only one study modeled a diseased, human coronary artery (Ohayon, et al., 2005). Mechanical analyses of these arteries are particularly relevant given acute coronary syndromes are typically caused by plaque rupture and subsequent thrombus formation.

In this work, a methodology using MMA sections to create 3-D finite element models of human coronary atherosclerotic plaque was developed. Sections were imaged, aligned using markers, and then segmented such that areas in a stained section were classified as media, fibrous intima, lipid, or calcification. Finite element models created from surfaces were meshed and appropriate boundary and loading conditions were applied. The theory of constrained mixtures was used to assign mechanical properties for each element based on the area fractions of up to four constituents.

Specific Aim III

Determine whether correlations between stress results from 3-D mechanical models and plaque features exist and whether these stress results are consistent with results from 2-D mechanical models.

Studies have shown that morphological description of a plaque is not in itself enough to predict rupture. Given plaque rupture occurs in areas of high stress concentrations, it is well accepted that mechanical stresses affect plaque stability. Based on morphological data, not all plaques with thin, fibrous caps and large lipid pools should have high stresses. However, 2-D structural analyses do not support this finding.

In this work, the 3-D mechanical models developed in Specific Aim II were used to calculate stress distributions. The effects of longitudinal variations were then determined. Finally, relationships between various plaque features and stresses were examined. These features included lipid content, fibrous cap thickness, stenosis severity, calcification content, and longitudinal variations.

CHAPTER 3:

MATERIALS AND METHODS

The materials and methods used in this research are described in this chapter. The chapter is divided into three major sections, which correspond to each of the specific aims presented in the previous chapter. The methods developed to quantify and correct for histologic distortions are first presented. Next, the methods used to develop three-dimensional (3-D) mechanical models of atherosclerotic plaque are discussed. Finally, a description of the methods used to determine whether correlations between stress results from 3-D models and plaque features exist is given.

Specific Aim I:

Quantify and correct for histologic distortions to achieve more accurate mechanical models of arteries.

Tissue Preparation

Right coronary arteries (RCAs) from five porcine hearts were studied. The hearts from 2–3.5 year-old, 400–600 pound farm swine were obtained from an abattoir within one hour of sacrifice and transported to the laboratory on ice. After transport, a 25 mm long segment was excised and trimmed of excess tissue, starting about 40mm distal to the aorta.

The artery was mounted by securing a female Kynar (Attofina, Philadelphia, PA) Luer (I.D.=1.4 mm) to each end with size 0 suture and placing the artery and Luers in a polypropylene mounting tube (I.D.=9.75mm) as shown in Figure 3.1. The artery was

held in place at one end with a stainless steel pin (D=1.3mm). The other end was adjusted in the tube such that the length of the artery was restored to its in-situ, pre-excision length. This end was then secured with another pin. The mounted artery was immersed in room temperature PBS for less than 3 hours before scanning. For the fresh scan, PBS was replaced with a 5% gelatin and 10% barium sulfate solution. Testing revealed that these concentrations of gelatin and barium provided optimal contrast in the micro-CT images.

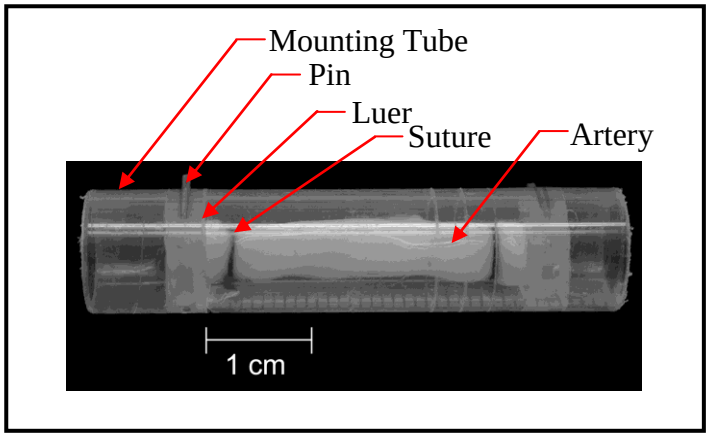

Figure 3.1. Photograph of the mounting system used. Luers were secured to each end of the artery with suture. The artery was then held in place in the mounting tube with two stainless steel pins.

Histologic Preparation

The mounted artery was rinsed in PBS. After removing the top pin, it was fixed in room temperature 10% neutral buffered formalin for approximately 36 hours. Removal of the pin enabled free axial movement during fixation.

The mounted artery was processed by dehydration and clearing. Infiltration was carried out in a solution made up of 75%(v/v) methyl methacrylate (MMA), 25%(v/v)

dibutyl phthalate, and 5%(w/v) benzoyl peroxide. The mounted artery was embedded in a radio-opaque block consisting of 74.1%(v/v) MMA, 24.7%(v/v) dibutyl phthalate, 5%(w/v) benzoyl peroxide, 1.2%(v/v) *N*, *N*-dimethyl-*p*-toluidine and 20%(w/v) barium sulfate.

Sections, 2.5μm thick, were cut using a retractable rotary microtome at a speed of 1.5 mm/sec. Every twentieth section was floated on a 45ºC water bath. The sections were mounted on gelatin glycerin coated glass slides and dried on a slide warmer at 60ºC for 30 minutes. Following deplasticization in acetone, the sections were rehydrated and stained with hematoxylin and aqueous eosin containing 1% calcium chloride. The detailed mounting, processing, embedding, and staining protocols are provided in Appendix A.

Micro-CT and Histologic Image Acquisition

Images were obtained at the fresh, embedded, and sectioned and stained states. Fresh and embedded state images were acquired with a microcomputed tomography (micro-CT) scanner (vivaCT 40, Scanco Medical, Switzerland) at a voxel resolution of 35.8μm (scan time= 9.2 minutes/29 slices). Stained sections were imaged using a light microscope (Eclipse E600W, Nikon Instruments Inc., Melville, NY). Phase contrast was used to help detect the registration marks.

Registration Marks

Registration marks were generated using nylon monofilament (D=0.25mm). Four 0.3-mm-diameter holes were drilled at consistent locations in each Luer. For each hole, the monofilament was threaded through the hole in the top Luer and the corresponding

hole in the bottom Luer. The monofilament was held taut within slits in the mounting tube. After embedding, the monofilament was removed and the remaining voids served as registration marks.

It was necessary to image the registration marks before and after sectioning and staining. The voids were apparent in micro-CT embedded state images and the microscope images. This is because barium sulfate adheres to the slides and is not removed when sections are deplasticized. Representative images are provided in the Results chapter.

3-D Reconstruction Techniques and Measurements

Using Amira 3.1 (TGS, Inc., San Diego, CA), images from the three states were segmented into binary images and three-dimensional reconstructions were generated. Segmentation refers to a process in which an image is partitioned into structures of interest that are separated from the background and from each other. Micro-CT images were segmented based on gray scale intensity. For each histologic image, the arterial wall was identified by tracing the lumen and the outer surface with a segmentation tool, which uses image gradients to complete the boundary between manually selected points. The histologic images were aligned using the registration marks.

Shrinkage in the longitudinal direction was determined by measuring length change between corresponding transverse segmentations from the fresh and embedded states. Corresponding cross-sections were identified using morphological landmarks, which were loose bits of adventitia, in sections near each end of the artery. The known distance between the two identified cross sections indicated the length of the artery. Multiple sections (n=10) were analyzed along the length and found to correspond based

on morphological landmarks. This correspondence validates the assumption that longitudinal shrinkage is uniform. Shrinkage in the transverse direction was determined by measuring arterial area change in a subset of cross sections (n=10/artery). These sections were more or less evenly distributed along the entire length of the artery.

The sectioning distortion was also analyzed in the same 10 cross-sections (per artery) by determining the location of the registration marks. Corresponding cross-sections from the embedded and sectioned and stained states were identified using morphological landmarks. The lengths in these states were approximately equal.

Cross-sectional images were imported into MatLab 6.5 (MathWorks Inc., Natick, MA) and the x and y coordinates of the centroid of each registration mark were obtained. Depicted in Figure 3.2, the program allows the user to zoom in and select registration marks.

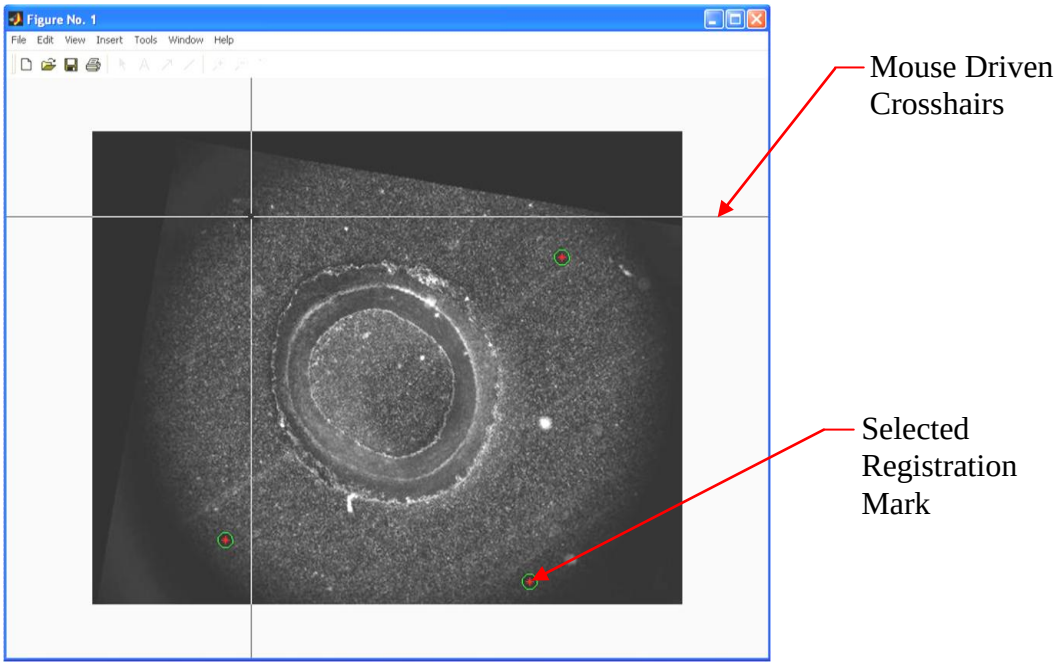

Figure 3.2. Graphic user interface used to select registration marks in a histologic image.

Testing revealed that identification of centroids was repeatable and was not user dependent. Four registration marks were identified in 5 images by two users. Comparing the locations determined by the users resulted in a mean absolute difference of 0.8 ± 0.7 pixels in the vertical direction and 0.7 ± 0.8 pixels in the horizontal direction.

From the two sets of data, an affine transformation matrix **A**, was obtained

$$\begin{Bmatrix} x \\ y \end{Bmatrix} = \begin{bmatrix} A_1 & A_2 \\ A_4 & A_5 \end{bmatrix} \begin{Bmatrix} X \\ Y \end{Bmatrix} + \begin{Bmatrix} A_3 \\ A_6 \end{Bmatrix} \qquad \text{Equation 3.1}$$

where x and y represent the deformed section and stained state hole coordinates and X and Y represent the undeformed embedded state hole coordinates. The fourth registration mark creates a redundancy in the data. Hence, a least squares approach was used to minimize the error. The matrix representation of the transformation is given by

$$\begin{bmatrix} x_1 & y_1 & 1 & 0 & 0 & 0 \\ 0 & 0 & 0 & x_1 & y_1 & 1 \\ x_2 & y_2 & 1 & 0 & 0 & 0 \\ 0 & 0 & 0 & x_2 & y_2 & 1 \\ x_3 & y_3 & 1 & 0 & 0 & 0 \\ 0 & 0 & 0 & x_3 & y_3 & 1 \\ x_4 & y_4 & 1 & 0 & 0 & 0 \\ 0 & 0 & 0 & x_4 & y_4 & 1 \end{bmatrix} * \begin{bmatrix} A_1 \\ A_2 \\ A_3 \\ A_4 \\ A_5 \\ A_6 \end{bmatrix} = \begin{bmatrix} X_1 \\ Y_1 \\ X_2 \\ Y_2 \\ X_3 \\ Y_3 \\ X_4 \\ Y_4 \end{bmatrix} \qquad \text{Equation 3.2}$$

Using the embedded state as the reference state for strain, Green strains were calculated for the sectioned and stained state using **A**

$$\begin{bmatrix} \varepsilon_x & \varepsilon_{xy} \\ \varepsilon_{xy} & \varepsilon_y \end{bmatrix} = \begin{bmatrix} 0.5*(A_1^2 + A_4^2 - 1) & 0.5*(A_1A_2 + A_5A_4) \\ 0.5*(A_1A_2 + A_5A_4) & 0.5*(A_2^2 + A_5^2 - 1) \end{bmatrix} \qquad \text{Equation 3.3}$$

where ε_x and ε_y are the extensional strains in directions x and y respectively and ε_{xy} is the shear stain. No attempt was made to orient the x and y axes with the cutting direction.

The principal strains, ε_1 and ε_2, and principal direction relative to directions x and y were also calculated (Dowling, 1999). The cutting direction was identified by grooves that are visible on the histologic sections. The Matlab programs used to calculate shrinkage distortions, obtain registration marks centroids, and calculate sectioning distortions are provided in Appendix B.

Distortion Correction

Coordinate data representing the lumen and outer boundary of 10 sectioned and stained and 10 embedded cross sections were obtained from the corresponding segmented images using Amira and imported into Matlab. Sectioning related distortions were then eliminated by applying the inverse of the affine transformation to the points from the sectioned and stained segmentations. Likewise, shrinkage related distortions were eliminated using a uniform, equibiaxial dilatation. This dilatation, which is mathematically equivalent to scaling about an arbitrary origin, was applied by multiplying the x and y coordinates of each point from the embedded segmentations to a common factor, f

$$f = \sqrt{1+s} \qquad \text{Equation 3.4}$$

where s is the percent shrinkage in cross-sectional area. The Matlab code used to correct for distortions is provided in Appendix B.

Error in Distortion Correction

Original segmentations and corrected reconstructions were registered using morphological landmarks. To determine the error associated with the sectioning correction, embedded segmentations were compared to sectioning artifact corrected

reconstructions (n=10/artery). Fresh segmentations were compared to shrinkage artifact corrected reconstructions to determine the error associated with the shrinkage correction (n=10/artery). Using Matlab, original segmentations were subtracted from corrected reconstructions. The error was taken as the number of pixels in the subtracted image as a percentage of the number of pixels in the original segmentation. The Matlab code is provided in Appendix B.

Comparison of Methyl Methacrylate and Paraffin

An additional artery was harvested, mounted, scanned in its fresh state, and fixed as previously described. The artery was then cut in half. One half was embedded in radio-opaque methyl methacrylate while the other half was routinely embedded in paraffin (Figure 3.3). The blocks were sectioned such that approximately consecutive sections were collected and stained.

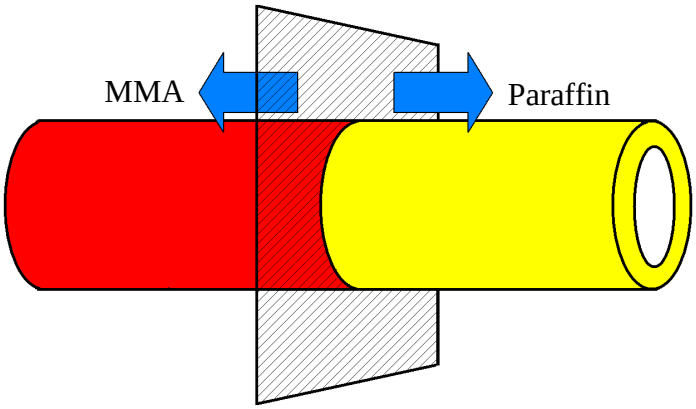

Figure 3.3. Schematic of the approach used to compare the effects of preparation related distortions on stresses in acrylic versus paraffin.

Finite element models were generated using Ansys 7.0 (Ansys Inc., Canonsburg, PA). The models were meshed using 4-node plane strain elements (Ansys Element

Number 42). Based on a previous isotropic incompressible model study, an elastic modulus of 100 kPa and a Possion's ratio of 0.49 for healthy artery were used (Lee, et al., 1996). A static pressure of 14.6 kPa (110 mmHg) was applied to the lumen and the maximum von Mises stresses were compared for each case.

Models of corresponding cross-sections and serial sections were generated. The models of corresponding cross-sections were generated using the abutting sections from the MMA and paraffin blocks. Both the micro-CT generated cross-section of the artery in its fresh state, and the corresponding MMA section corrected for distortion were used. Serial section models were generated using four additional uncorrected serial MMA and four additional serial paraffin cross-sections.

Statistics

Statistical analyses were performed using Minitab Release 12.23 (Minitab Inc., State College, PA). Given the data were normally distributed (as confirmed by Anderson-Darling normality testing), paired t-tests were used to assess differences. Differences were considered significant at values of $p < 0.05$.

Specific Aim II:

Develop three-dimensional mechanical models of human coronary atherosclerotic plaques based on minimally distorted histologic sections.

The five key steps associated with the development of any mechanical model, which include modeling of geometry, loads and boundary conditions, mechanical properties, and mechanical processes, served as a basis for the development of our

methodology. A schematic overview of the methods used to develop the mechanical models in this study is given in Figure 3.4.

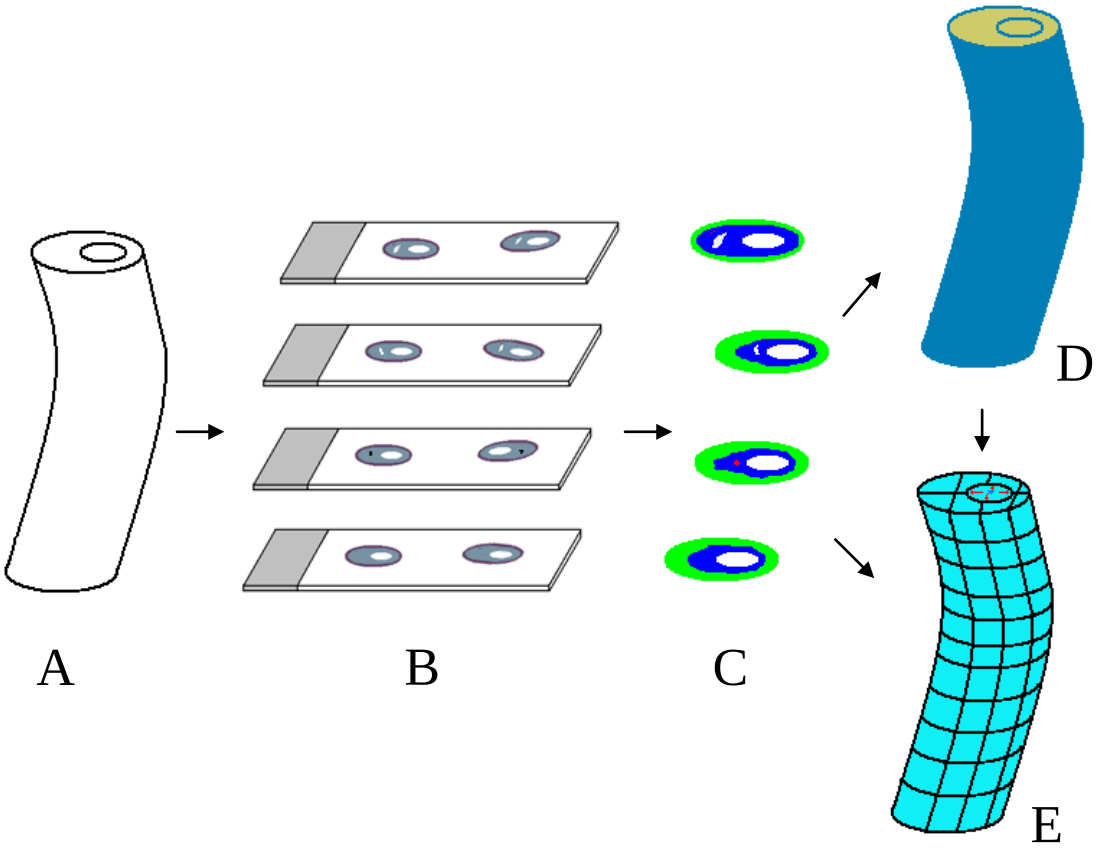

Figure 3.4. Schematic overview of methods used to develop 3-D FE models of plaques. A, Specimen is acquired. B, Minimally distorted histologic sections are generated. C, Images of histologic sections are acquired. Images are aligned and segmented. D, Aligned, segmented images are used to generate smooth 3-D surface reconstructions. E, Surface reconstructions are used to generate solid FE model. Aligned, segmented images are used to assign mechanical properties to elements of FE model. Boundary and loading conditions are applied to FE model.

Modeling of Geometry

As shown in Figure 3.4, the most involved modeling step in this study is the modeling of geometry. The reason for this relates to the novelty of many of our geometrical modeling methods.

Specimen Acquisition

Five explanted human hearts were studied. The hearts, which were obtained from cardiac transplant recipients, were acquired from Emory University Hospital. The age, sex, medication history, and medical history each recipient were recorded. A segment of the right coronary artery, located at about 20 mm from the aorta and approximately 40 mm in length after removal, was excised and trimmed of excess tissue. The artery was stored in PBS and placed on ice during transport back to the laboratory.

Histologic Preparation

In order to preserve the in vivo morphology of an artery, so that correlations of biological markers of disease with stresses are possible, an artery must be pressure-fixed. Pressure fixation minimizes histologic artifacts caused by postmortem collapse and contraction (Stary, et al., 1995). At physiologic lumen pressures near 80 mmHg, distinct difference in the structural organization of the arterial wall occur (Wolinsky and Glagov, 1964). Thus, this fixation pressure was used in our study. Because coronary arteries have many branches, pressure fixation can be challenging. Leaks that form during fixation must be stopped to ensure pressurization is maintained until geometrical changes due to fixation cease.

To determine the time needed for geometrical changes to cease, the outer diameter of a porcine carotid artery undergoing pressure fixation at 80 mm Hg was monitored for approximately 24 hours. Porcine arteries are comparable to human arteries in morphology and microscopic structure (Swindle, 1992). However, carotid arteries have fewer branches making pressure fixation less problematic. In addition, carotid arteries, which are thicker than coronary arteries, take longer to fix. For these reasons, it

is logical to assume the results obtained for porcine carotid arteries are extendable to human coronary arteries. As is shown Figure 3.5, changes in diameter of 3% take place during the first 2 hours of fixation. This result suggests that it is only necessary to maintain pressurization for 2 hours.

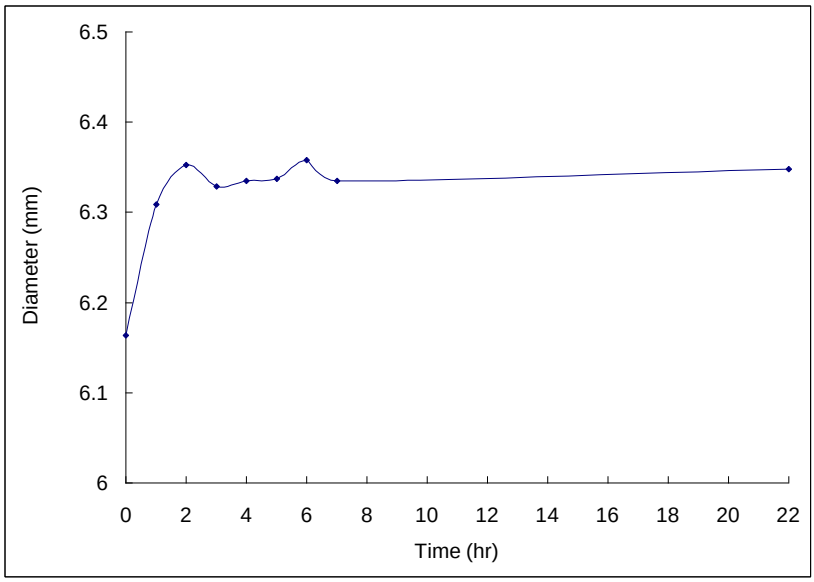

Figure 3.5. Change in pressurized diameter of a porcine carotid artery with respect to time due to pressure fixation at 80 mm Hg.

Therefore, within 2 hours of transplant surgery, the segment of RCA was pressure-fixed in room temperature 10% neutral buffered formalin at a physiologic lumen pressure of 80 mm Hg for approximately 2 additional hours. Pressurization was removed and the artery was kept in formalin for 36 hours, the time required to complete cross-linking (Helander, 1994). The artery was then stored in 70% alcohol until it was processed.

Arteries were processed by dehydration and clearing on a Thermo Shandon Pathcenter (Thermo Electron Corporation, Pittsburg, PA). Infiltration was carried out in a solution made up of 75% (v/v) methylmethacrylate (Acros Organics, Morris Plains, NJ),

25% (v/v) dibutyl phthalate (Aldrich Chemical Company, Inc., Milwaukee, WI), and 5% (w/v) benzoyl peroxide (Sigma-Aldrich, Inc. St. Louis, MO). The arteries were placed in a polypropylene tube with an inner diameter of 12.7 mm and embedded in acrylic blocks. Each block consisted of 74.1% (v/v) methylmethacrylate, 24.7% dibutyl phthalate (v/v), 5% (w/v) benzoyl peroxide, 1.2% (v/v) N, N-dimethyl-p-toluidine. The detailed processing and embedding protocol is provided in Appendix A.

Following polymerization, the polypropylene tubes were removed. The blocks were cut and ground to ensure that the top and bottom faces were perpendicular to the axis of the cylindrical block. Testing revealed that the sectioning of blocks longer than 10 mm produces sections of uneven thickness, with some sections being as thick as 6 μm. When a block is longer than 10 mm, the force of the blade on the block causes appreciable movement or bending of the block. Uneven section thickness results because the block is no longer perpendicular to the cutting plane. Therefore, all blocks were cut into segments no longer than 10 mm in length using a precision saw (Isomet 1000, Buehler Ltd., USA) prior to microtomy. The proximal face of each block segment was marked so that orientation was not lost.

Sections, 3 μm thick and collected at 150 μm intervals, were cut from the block at a specimen head speed of 1.5 mm/sec with a tungsten carbide blade (Delaware Diamond Knives, Wilmington, DE) using a retractable rotary microtome (Microm, Walldorf, GE). The proximal face of the block was aligned perpendicular to the cutting plane. The selection the sectioning interval is justified elsewhere. Sections were floated on a 45ºC water bath to reduce distortions due to cutting. To ensure section to slide adherence, the sections were mounted on glass slides coated with Poly-L-lysine (Sigma-Aldrich, Inc. St.

Louis, MO), pressed, and dried at 50ºC overnight. Following deplasticization in xylene and acetone, the sections were rehydrated and stained.

Masson's trichrome staining was used to detect smooth muscle and collagen. Von Kossa's staining was used to identify calcification. The protocols for these staining procedures are described in Appendix A. Once stained, the sections were dehydrated and coverslipped using a resinous mountant (Richard-Allan Scientific, Kalamazoo, MI).

Image Acquisition

Image stacks of the arterial sections in each slide were obtained before and after staining. The two image stacks facilitate axial alignment of sections as is further discussed. Slides were imaged using a slide scanner (Super CoolScan 9000 ED, Nikon Instruments Inc., Tokyo, Japan). Such a scanner is beneficial because the entire slide can be imaged all at once. The spatial resolution of the scanner was 19.05 μm/pixel. This resolution is 5 times better than the in-plane resolution of the images in all other 3-D studies that have previously been discussed.

Gross Alignment of Stained Slide Images with Unstained Slide Images

For purposes of axial alignment, the locations of the sections in the unstained and stained slide images must coincide. As is shown in Figure 3.6, this does not automatically occur upon scanning. Slides to be scanned are loaded into a tray fabricated by the manufacturer of the scanner. This tray was designed in such a way that the user is unable to repeatedly place slides in the same scanning position. Thus, following scanning, stained slide images had to be aligned with unstained slide images.

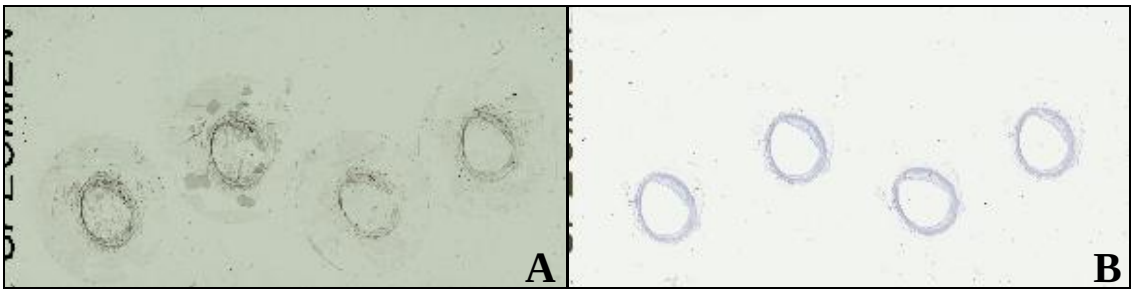

Figure 3.6. Representative image of a slide in the unstained (A) and stained (B) state. The locations of the sections do not coincide in the images because the origin of the images does not coincide.

To determine the amount of translational and rotational freedom associated with the positioning of a slide into the tray, a representative slide was positioned at opposite loading extremes and scans were obtained. The locations of a corresponding feature in each scan were used to calculate the maximum translation and rotation that may occur due to loading. While rotations were minimal (less than 1.5 degrees), translations of 410 pixels (7811μm) were observed. This implies that in order to align a stained slide image with the corresponding unstained slide image, it is only necessary to translate the stained slide image. To calculate each translation value, it is only necessary to identify a single, corresponding point in each set of stained and unstained slide images.

Stained slide images were aligned with unstained slides images using a program written in Matlab. Depicted in Figure 3.7, the program allows the user to zoom in and select a landmark that is present in both the unstained and stained images. The landmark used in each slide was the writing on the slide because staining has no effect on its size or location. Based on the locations of the selected landmarks, the stained images are moved accordingly. The Matlab code used to identify landmarks and align stained slide images with the unstained slide images is included in Appendix B.

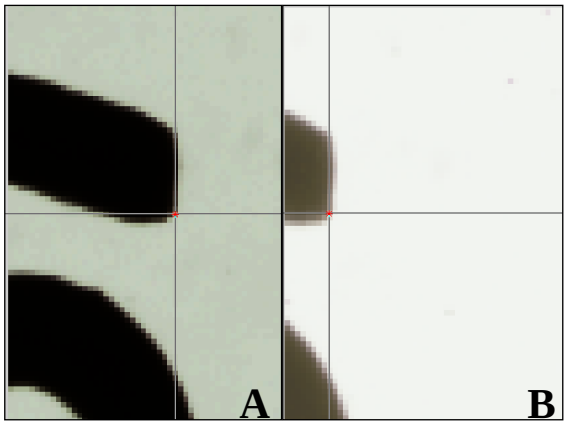

Figure 3.7. Selection of a landmark in an unstained (A) and stained (B) image.

Testing revealed that the landmark selection method is repeatable and is not user dependent. Landmarks were identified in fifteen sets of images by two users. Comparing the translation calculations of the users resulted in a mean absolute difference of 0.5 ± 0.6 pixels in the vertical direction and 0.6 ± 0.5 pixels in the horizontal direction.

After the stained slide images were aligned with unstained slide images, the unstained and stained images were identically cropped such that corresponding images of each section in its unstained and stained state were obtained. The Matlab code used to crop the images is given in Appendix B.

Axial Alignment of Sections

A method was developed to maintain artery curvature while axially aligning sections. Unstained serial sections were first axially aligned using markers present in the unstained images. These markers were the edge of the resin section and grooves due to imperfections in the microtome's blade (Figure 3.8). Because circular sections are generated, the resin edge could only be used to appropriately translate the sections. The scratch marks were required for rotational alignment purposes. Information obtained

from the alignment of the unstained sections was then used to axially align the stained serial sections.

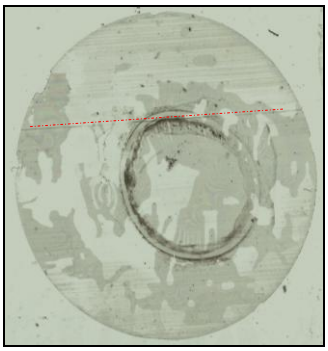

Figure 3.8. Representative image of an unstained section. The edge of the section is apparent and a cutting groove has been highlighted for emphasis.

The technique of using markers that do not change position along the length of the block allowed the curvature of the artery to be maintained. Consider the idealized case depicted in Figure 3.9. When sections are aligned using the resin edge and blade mark, curvature is maintained. However, when sections are aligned using the edge of the tissue, curvature is lost.

To axially align the image stack of unstained serial sections, each image was translated and rotated using Amira. In some cases, images also had to be flipped. This is because the section was flipped when it was placed on the water bath. The transformation information (that is how each image was translated and rotated and whether it was flipped) to align the unstained images was exported from Amira. In Matlab, the image stack of stained serial sections was aligned by translating, rotating, and flipping each stained image exactly as the corresponding unstained image was translated, rotated, and flipped. The alignment of the stained images in this manner was possible

because the original unstained and stained images were identically oriented. The Matlab code used to align the stained section images is included in Appendix B.

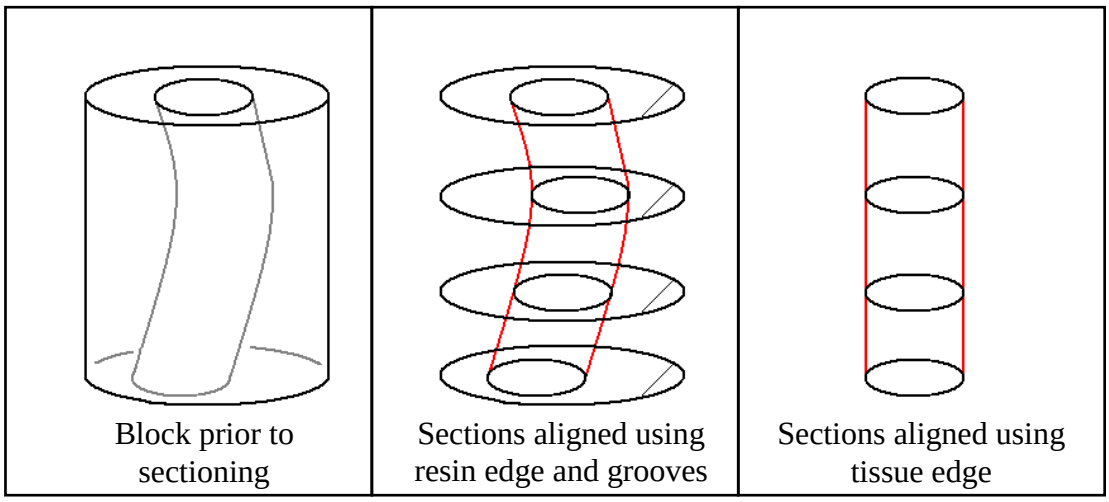

Figure 3.9. Alignment techniques applied to an idealized case. Curvature is maintained when sections are aligned using the resin edge and cutting grooves, but is lost when sections are aligned using the tissue edge.

Image Segmentation

A segmentation scheme was used to classify each pixel in a stained image as one of five components (Skrinjar, 2004). These components included media, fibrous intima, lipid, calcification, and background. Media and background were segmented automatically based on color differences. However, it was not always possible to use such an approach to segment lipid, fibrous intima, and calcification. Therefore, lipid and calcification were segmented using semi-automatic techniques. Pixels that were not identified as media, lipid, or calcification were characterized as fibrous intima.

To automatically segment the media and background, a representative image from each artery was first segmented manually in ImagePro Plus (Media Cybernetics Inc.,

Silver Springs, MD) based on visual inspection. In this manual segmentation, pixels were classified as background, media, or other tissue. Background and media were identified by manually defining and applying appropriate threshold ranges. All pixels not classified as background or media were classified as other tissue. A representative example of a manual segmentation is depicted in Figure 3.10.

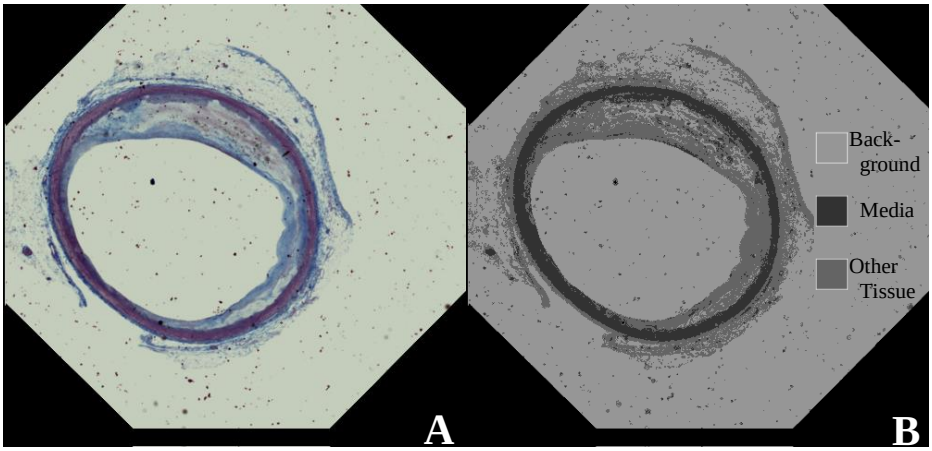

Figure 3.10. Representative image of a stained section (A) and the corresponding manual segmentation (B).

All of the stained images were then segmented automatically in Matlab. As with the manual segmentation, all pixels in the automatic segmentations were classified as background, media, or other tissue. To obtain the automatic segmentations, the average color of each of the 3 components, which is a point in RGB space, was first obtained from the manual segmentation. Then, for each pixel in every stained image, the distance between the pixel's color, also a point in RGB space, and each of the 3 component's average colors was calculated.

The equation used to calculate each of these distances, d, is given by

$$d = \sqrt{(R_c - R_p)^2 + (G_c - G_p)^2 + (B_c - B_p)^2} \qquad \text{Equation 3.5}$$

where R_c, G_c, and B_c represent the red, green, and blue color channel positions of a component (known from the manual segmentation), respectively and R_p, G_p, and B_p represent the red, green, and blue color channel positions of the pixel, respectively (Gonzalez and Woods, 2002). Once the three distances were calculated, the pixel was classified as the component that was nearest in RGB space. It is important to mention that it was possible to use this method because the colors of the components were distinct.

Table 3.1, which is based on the representative images in Figure 3.10, demonstrates that the variation in color within an individual component is small relative to the variations in color between components. Figure 3.11 shows an example of an automatic segmentation. The Matlab code used to generate automatic segmentations is included in Appendix B.

Table 3.1 Average color channel values of pixels in a stained image classified as either background, media, or other tissue in the corresponding manual segmentation (mean ± SD).

	Red Channel	Green Channel	Blue Channel
Background	84 ± 8	77 ± 9	110 ± 9
Media	192 ± 4	201 ± 4	186 ± 2
Other Tissue	120 ± 8	133 ± 8	151 ± 6

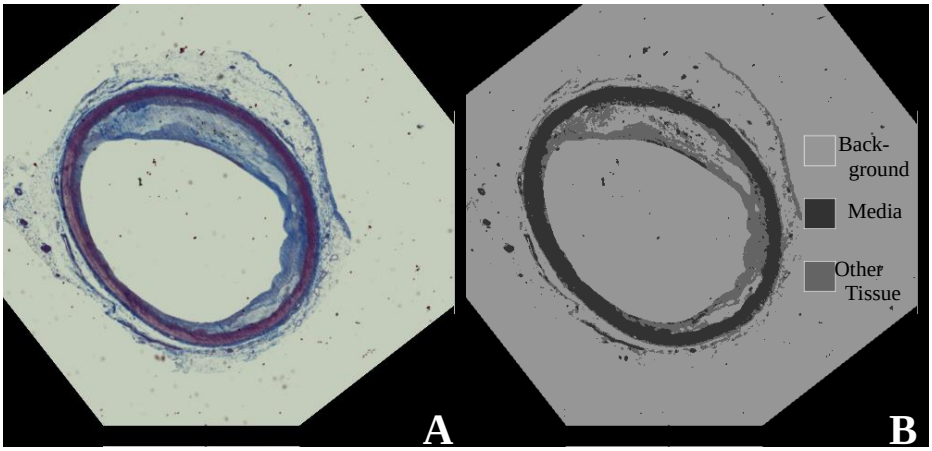

Figure 3.11. Representative image of a stained section (A) and the corresponding automatic segmentation (B).

Identification of the arterial wall was straight forward once the images had been automatically segmented. For modeling purposes, the adventitia of the artery was excluded. We are aware of the concept that functional changes in the adventitia lead to vascular pathology (Rey and Pagano, 2002). However, we, like others (Kilpatrick, et al., 2001), have found that the adventitia is a minor factor in determining fibrous cap stresses because the contribution of the connective tissues of the adventitia in load bearing is small. Thus, the outer wall boundary always coincided with the outer edge of the largest region of media. This region was identified by detecting the largest group of connected pixels. The region was isolated resulting in a binary image. Holes in this image were then filled. A hole is defined as a set of background pixels that cannot be reached by filling in the background from the edge of the image. The second largest background region, which is the lumen, was subtracted to produce an image of the arterial wall. An example of these image processing steps, applied to the segmentation in Figure 3.11, is presented in Figure 3.12. The Matlab code used to identify the arterial wall is given in Appendix B.

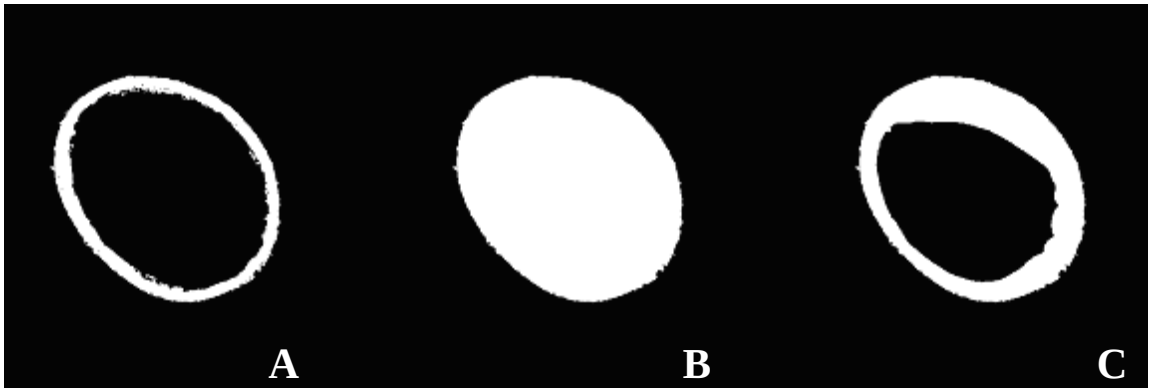

Figure 3.12. Steps used to identify the arterial wall. The largest region of media is isolated (A), the holes are filled (B), and the lumen is subtracted (C).

As mentioned, in sets of stained images it is not always possible to differentiate between lipid, fibrous intima, and calcification based solely on color differences. This is due to the occurrence of staining variability. Slide to slide variability typically occurs because all slides cannot be simultaneously stained. Variability within a section may be the result of slight non-uniformities in section thickness. For these reasons, lipid and calcification were identified using semi-automatic techniques in Amira. Lipid was identified by tracing its border with a segmentation tool. This tool uses image gradients to complete the boundary between manually selected points. Calcification was identified by thresholding regions in which calcification were present. Any inaccuracies that resulted in the regions were manually removed. Figure 3.13 shows the results of these semi-automatic procedures applied to the representative image in Figure 3.11. The segmentations obtained were finally combined in Matlab. Pixels within the arterial wall that were not identified as media, lipid, or calcification were characterized as fibrous intima. The final segmentation obtained for the representative image in Figure 3.11 is shown in Figure 3.14. Matlab code for the combination of binary images of components

into a single segmentation is included in Appendix B. For the five diseased arteries, a total of 345 images were segmented.

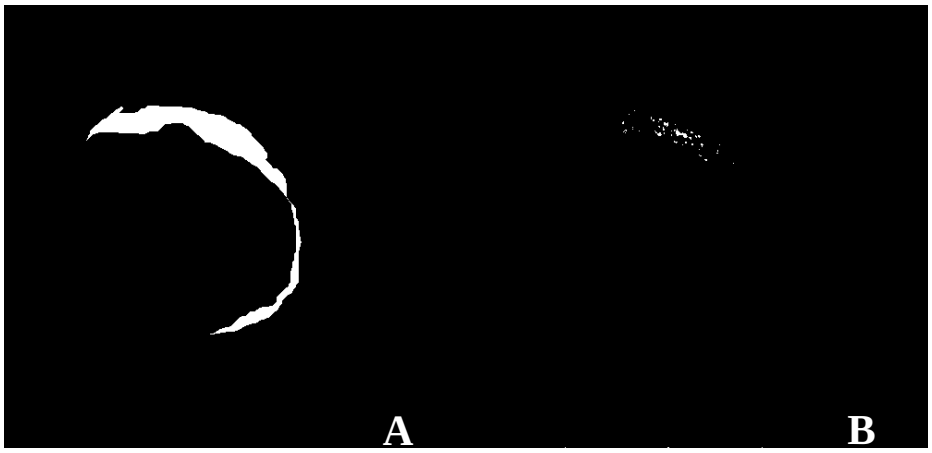

Figure 3.13. Representative semi-automatic segmentations of lipid (A) and calcification (B).

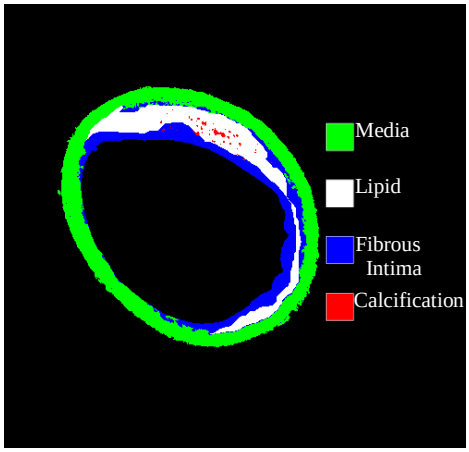

Figure 3.14. Representative segmentation of an image of a stained artery in which each pixel has been classified as media, fibrous intima, lipid, calcification, or background.

Smoothing and Three-Dimensional Surface Reconstruction

Surface noise and irregularities due to image processing artifacts cause stress concentrations in finite element models. To avoid such concentrations, smoothing must be applied to the segmented images before three-dimensional surfaces are reconstructed. However, the smoothing approach selected should gradually affect surface detail and avoid substantial geometric shrinkage. In the present context, cross-sectional area changes or volumetric changes greater than 5% are considered substantial.

While there are many different techniques for image smoothing, Gaussian smoothing is commonly used. It is applied to an image by convolving the image with a kernel having a Gaussian distribution. The equation of Gaussian distribution is given by

$$G(x, y, \sigma) = \frac{1}{2\pi\sigma^2} e^{-(x^2+y^2)/(2\sigma^2)} \qquad \text{Equation 3.6}$$

where $(x^2 + y^2)$ is the blur radius and σ is the standard deviation of the Gaussian distribution (Gonzalez and Woods, 2002). The Gaussian smoothing operator outputs a weighted average of each pixel's neighborhood. The original pixel's value receives the heaviest weight and neighboring pixels receive smaller weights. As the distance from a neighboring pixel to the original pixel increases, the weight that the neighboring pixel receives decreases. This is in contrast to a mean filter's uniformly weighted average. Because of this, a Gaussian provides gentler smoothing and preserves edges better than a mean filter.

A Gaussian smoothing operator was used to smooth the binary images of the arterial wall and thereby reduce surface noise and irregularities. To ensure that the smoothing did not cause substantial geometric shrinkage, cross-sectional area measurements were made before and after smoothing in 383 sections. Comparisons

revealed that for a kernel size of 5 x 5 pixels and a standard deviation of 3 pixels changes in outer and luminal cross-sectional area of 2.40 ± 0.15% and 3.27 ± 0.23%, respectively occurred.

In order to generate three-dimensional surface reconstructions, boundary pixels at the inner and outer boundaries of the arterial wall were first identified in the smoothed images and then reduced to point data. These three-dimensional sets of points are known as point clouds. The point cloud data was downsized in such a way that geometric changes were minimal. For 383 sections, downsizing by 75% resulted in outer and luminal cross-sectional area changes of 0.02% ± 0.02% and 0.02% ± 0.02%, respectively. Further downsizing was avoided so that the in-plane spacing between points was at least 2 times that of the out-of-plane spacing. This ensured surface detail was maintained. Matlab code for the application of Gaussian smoothing and the downsizing of the point clouds is provided in Appendix B.

Geomagic Studio 6 (Raindrop Geomagic Inc., Research Triangle Park, NC), a commercially available reverse engineering software, was used to convert the point clouds into non-uniform rational B-spline (NURBS) surfaces (Piegl and Tiller, 1997). A NURBS surface of degree (p,q) is defined as

$$b(t,s) = \frac{\sum_{i=0}^{n}\sum_{j-o}^{m} N_{i,p}(t)N_{j,q}(s)w_{i,j}b_{i,j}}{\sum_{i=0}^{n}\sum_{j=o}^{m} N_{i,p}(t)N_{j,q}(s)w_{i,j}}, 0 \le t,s \le 1 \qquad \text{Equation 3.7}$$

where $N_{i,p}$ and $N_{j,q}$ are the B-spline basis functions, $b_{i,j}$ are the control points, and $w_{i,j}$ are the weights of $b_{i,j}$. Control points are a grid of points used to describe a curved surface. Each point is similar to a magnet pulling on the curve. Therefore, each control point

affects the entire curve. The exact influence of a control point is determined by its weight; the greater the weight, the greater the influence.

A detailed description on the generation of arterial surfaces in Geomagic has been provided by Carnell (2005). Figure 3.15, which shows the luminal surface of an artery, depicts the steps followed in the generation of a NURBS surface from a set of point cloud data. Briefly, point clouds were first imported into the software and then subjected to a noise reduction operation. This operation, which reduces surface irregularities, decreases the variance in B-spline curves producing more normalized curves. Whereas the Gaussian blurring smoothed two-dimensional images of cross-sections, this approach smoothed the three-dimensional point cloud data. For 383 sections, noise reduction caused changes in outer and luminal cross-sectional area of 1.07 ± 0.80% and 0.86 ± 0.75%, respectively.

After de-noising, the point data was converted into a polygonal surface, a triangle-based surface in which all of the triangles are continuously connected by their edges. NURBS surfaces, with continuity in curvature between patches, were finally fitted to the polygonal surfaces. The NURBS surfaces were written as Initial Graphics Exchange Specification (IGES) files. In the past, others (Holzapfel, et al., 2005; Holzapfel, et al., 2002) have generated 3-D FE models using non-uniform rational b-spline (NURBS) surfaces. The use of such surfaces is preferable to other reconstruction techniques because smooth surfaces, which are present in arterial structures, are provided. In addition, NURBS surfaces are easily handled by FE analysis software and are well-suited for FE mesh generation.

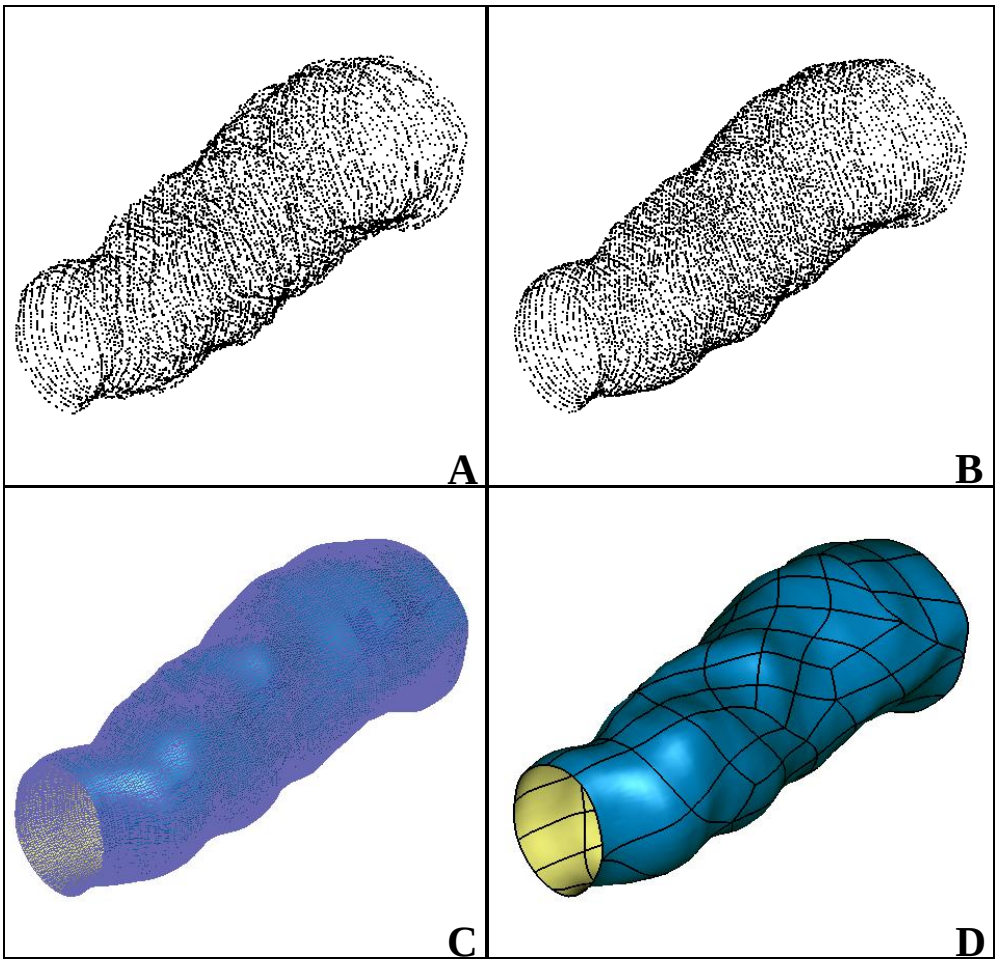

Figure 3.15. Steps followed to obtain a NURBS surface of the lumen of an artery. Point cloud data (A) is de-noised (B) and then converted into a polygonal surface (C). This surface is then fitted with a NURBS surface (D).

Three-Dimensional Solid Finite Element Model Generation

In order to determine the distribution of stress within the arterial wall, a three-dimensional solid finite element model based on surface reconstructions must be developed. Once the three-dimensional reconstructions of the outer and luminal walls are generated, the IGES files containing the surfaces can be imported directly into Ansys 9.0 (Ansys Inc., Canonsburg, PA), a commercially available finite element analysis software. Keypoints, lines, and areas are automatically assigned to the surfaces.

The steps followed to generate a solid model from NURBS surfaces are illustrated in Figure 3.16.

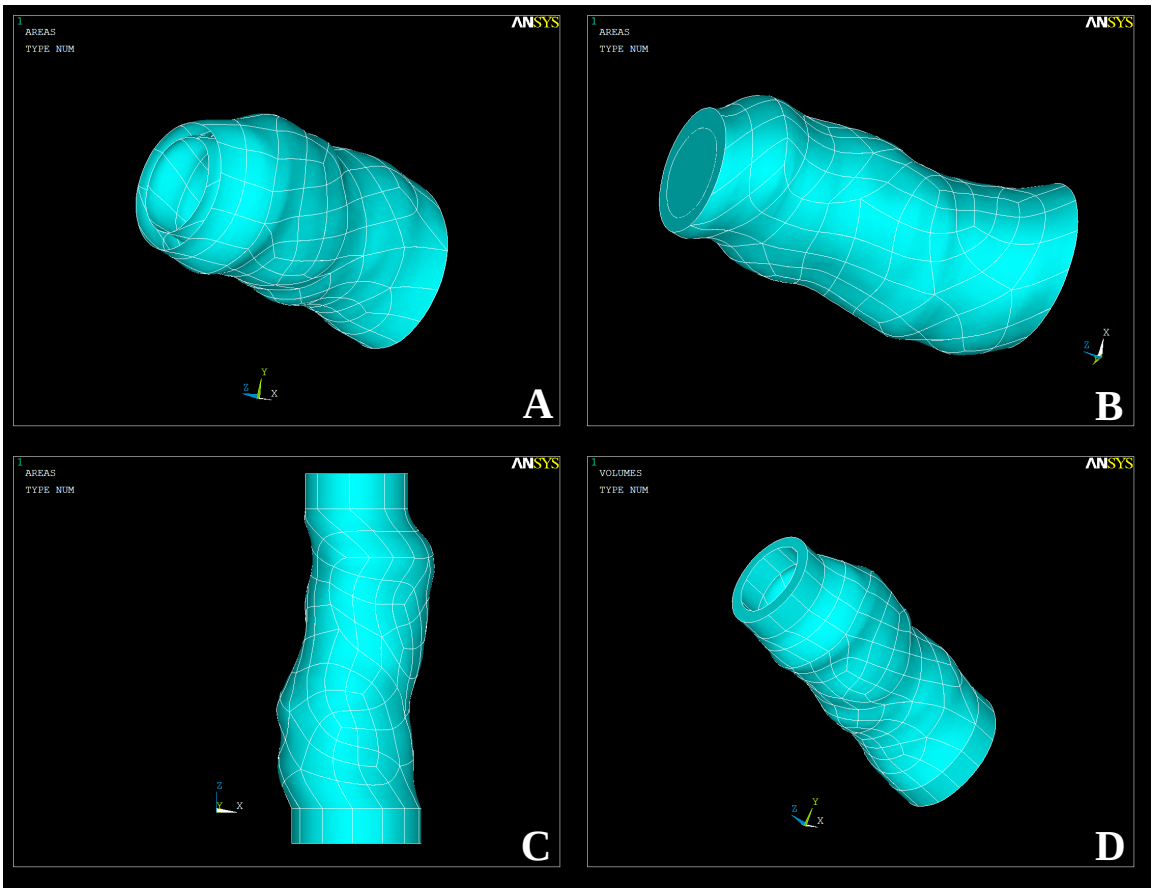

Figure 3.16. Steps followed to obtain a solid model of an artery. NURBS surfaces are imported into Ansys (A), both surfaces are capped off (B), volumes are created and the caps are extruded (C), and the luminal volume is eliminated (D).

The outer and luminal wall surfaces were first imported into Ansys. Cross-sectional areas which cap-off both ends of the outer and luminal wall surfaces were then generated. These caps were perpendicular to the surfaces' axial direction. Two volumes were then created: a volume made up of the outer surface and its caps and a volume made up of the luminal surface and its caps. For purposes related to the assignment of

boundary conditions, the caps of both volumes were extruded by a length approximately one quarter to one half that of the artery's inner diameter. Justification for this extrusion and a detailed description on the assignment of boundary conditions is provided later in this chapter. The resulting extruded volumes were added to the volume from which they originated. Finally, the luminal volume was eliminated using a Boolean operator.

Model Dimensions

The inner and outer diameters of each model were calculated at section intervals of 150 μm distributed uniformly along the length. The Matlab code used to calculate diameters is provided in Appendix B. Model length was calculated by multiplying the number of segmentations minus one by the sectioning interval.

Modeling of Mechanical Properties

Modeling of properties means that appropriate constitutive equations are selected for the arterial tissue that is being modeled. An important aspect in the development of the present methodology involved the selection of mechanical property modeling assumptions. Some assumptions were made in order to reduce modeling or computational complexities, while others were required because actual parameter data are unknown.

In this study, the models' properties were based on the following assumptions. To represent the heterogeneity of atherosclerotic plaques, the plaque was separated into four constituents, namely lipid, media, fibrous intima, and calcification. Each constituent was considered homogeneous and isotropic. Partitioning into four uniform components is obviously a simplification. However, we, like others (Beattie, et al., 1998; Cheng, et al., 1993; Kilpatrick, et al., 2001; Kilpatrick, et al., 2002; Lee, et al., 1996; Loree, et al.,

1992; Ohayon, et al., 2005), used this approach simply because more accurate heterogeneous and anisotropic constituent data are not available.

Further, based on the experimental findings in a study by Beattie et al. (1998), each constituent was considered linear elastic. That study found that over a physiologic range of pressures all constituents exhibit a linear mechanical response characterized by an elastic modulus. The average values for these moduli (n=7) are shown in Table 3.2. Others studies have also assumed plaque components exhibit linear elastic behavior, but used different and varied elastic moduli values (Cheng, et al., 1993; Lee, et al., 1996; Loree, et al., 1992; Ohayon, et al., 2005). Assuming that each constituent exhibits a linear mechanical response likely results in underestimations of the Young's moduli at high luminal pressures. However, one study (Williamson, et al., 2003) has suggested that stresses within the lipid, media, fibrous intima, and calcification have low sensitivities for variation in elastic moduli values.

Table 3.2. Average values of moduli (n=7) of plaque constituents (Beattie, et al., 1998).

Constituent	E (kPa)
Media	2.45×10^{2}
Fibrous intima	1.82×10^{3}
Lipid	3.88×10^{1}
Calcification	1.07×10^{4}

A more accurate nonlinear 2-D stress-strain relation for the media of human coronary arteries has been reported (Carmines et al., 1991). However, based on

Williamson's and our own findings, we did not use this relation for the media in our models. Changes in the elastic modulus of the media are unlikely to lead to substantial changes in fibrous cap stresses. This is due in part to the part to the spatial distribution of the media. We observed that the area fraction of media is small relative to the area fraction of the much stiffer fibrous intima within the bound of the internal elastic lamina. The largest area fraction of media is located at the outer periphery of the artery, where stresses are lowest.

We chose to use the properties of Beattie because they were collected on whole, human atherosclerotic segments using a biaxial, physiologic loading approach. Such an approach is preferable to uniaxial testing of isolated plaques in which results are difficult to interpret given the physiologic geometry is destroyed by excising the plaque from the vessel.

We used the available mechanical properties of human aortic atherosclerotic plaque, because to the best of our knowledge, no mechanical property data have been reported for human coronary atherosclerotic plaque. We are aware that the morphology and composition of an arterial wall varies with blood vessel type. The collagen to elastin ratio and distribution in healthy coronary arteries are different from those in healthy aorta. In healthy coronary arteries, which have a higher content of collagen, the elastin is localized mainly in the internal elastic lamina. In healthy aorta, the elastin is distributed throughout the media. However, histopathological analysis of the fibrous cap of diseased coronary and aorta has revealed that the two have similar morphology and composition (Marcu et al., 2001). Thus, use of the mechanical properties of aortic atherosclerotic plaque is justifiable. In addition, non-coronary atherosclerotic plaque properties have

been repeatedly used in other coronary artery plaque studies (Cheng, et al., 1993; Huang, et al., 2001; Lee, et al., 1996; Loree, et al., 1992; Veress, et al., 1998; Veress, et al., 2000).

Most biological tissues hardly change in volume when a load is applied, meaning they are almost incompressible. This is because they contain mostly water (approximately 70%), which is incompressible at physiologic pressures (Fung, 1993). In our study, each component was assigned a Poisson's ratio of 0.49, because the finite element algorithm used cannot tolerate nearly incompressible materials. In summary, only the elastic modulus (Table 3.2) and Poisson's ratio (0.49) of each constituent was needed to characterize the mechanical behavior of that constituent.

The models were meshed in Ansys using solid elements (Ansys Element Number 187: Figure 3.17). These three-dimensional tetrahedral elements are appropriate in light of the geometrical complexities associated with the model. The element is defined by 10 nodes each having three degrees of freedom: translations in the nodal x, y, and z directions. Additional information on Ansys Solid 187 elements is provided in the Ansys 9.0 Theory Reference Manual (2004b) and the Ansys 9.0 Elements Reference Manual (2004a).

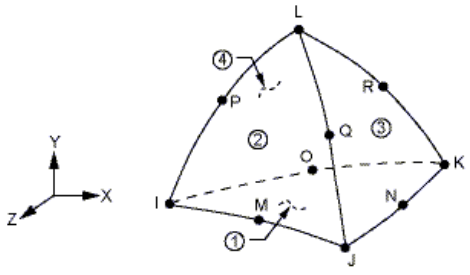

Figure 3.17. Ansys Solid 187 element geometry.

Two meshing methods were possible; either have each element contain a single constituent and corresponding elastic modulus value, or allow elements to contain multiple constituents and an averaged elastic modulus value. The former is problematic in that generated meshes may be irregular and contain skewed elements or elements with poor aspect ratios and result in inaccurate stress predictions. Therefore, the latter was used.

The arterial tissue was considered a constrained mixture (Humphrey and Rajagopal, 2002). Depicted in Figure 3.18, mixture theory states that an infinitesimal volume is represented by the coexistence of homogenized constituents.

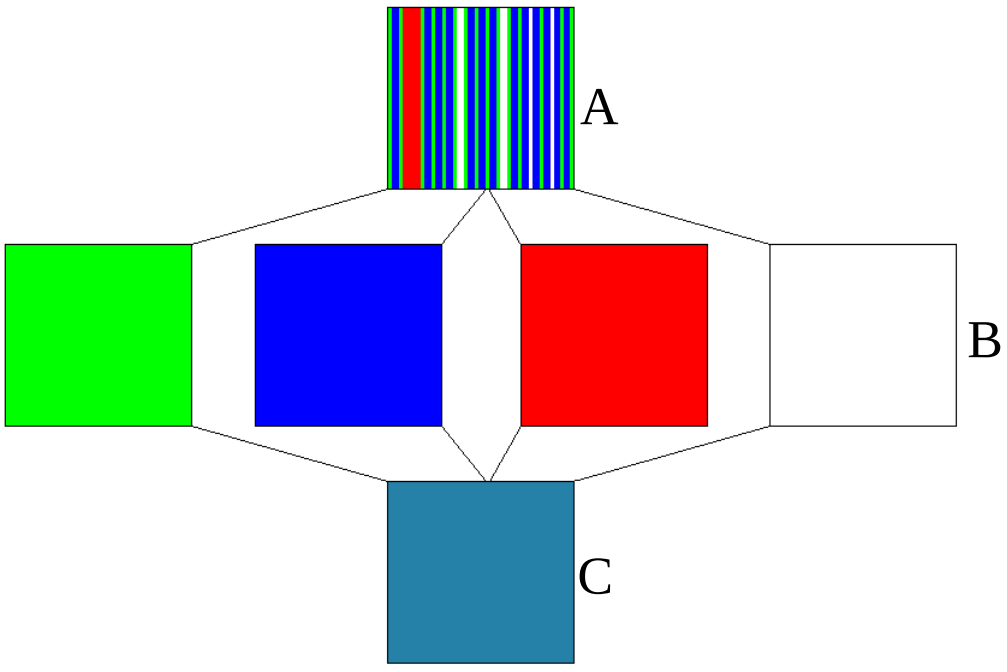

Figure 3.18. Schematic representation of mixture theory. An infinitesimal volume (A) is separated into homogenized constituents (B) and is then replaced (C).

The mass density of a constituent, ρ^i, is the mass of constituent i per volume of the mixture, whereas ρ is a mixture quantity defined by

$$\rho = \sum \rho^i \qquad \text{Equation 3.8}$$

The mass fraction for constituent i, ϕ^i, is defined as

$$\phi^i = \frac{\rho^i}{\rho} \qquad \text{Equation 3.9}$$

Thus,

$$\sum \phi^i = 1 \qquad \text{Equation 3.10}$$

In the case of a constrained mixture, each constituent has the same displacement and velocity as that of the mixture. Therefore, the Cauchy stress, T_{xy}, is given by

$$T_{xy} = \sum \phi^i T^i_{xy} \qquad \text{Equation 3.11}$$

where T^i_{xy} is the Cauchy stress for constituent i.

Obtaining constituent area fractions specific to each element is algorithmically complex. Therefore, circular areas in the two segmentations nearest each element were identified. First, the centroid locations of the elements in a model were exported from Ansys into Matlab and the average distance between centroids was calculated. Figure 3.19, which shows an idealized model, depicts the steps followed to obtain the regions of interest in segmentations used to calculate the mechanical properties for each element. The location of each element's centroid, (X_C,Y_C,Z_C), in the finite element model was obtained. The corresponding location within the stack of segmentations was then identified. Based on the z-coordinate location, the segmentation above the centroid, positioned at Z_A, and the segmentation below the centroid, positioned at Z_B, were located. Within these 2 segmentations a circular region of interest was identified. The center of

the circle in the segmentation above the centroid was located at (X_C,Y_C,Z_A) and the center of the circle in the segmentation below the centroid was located at (X_C,Y_C,Z_B). Notice that X_C and Y_C correspond to the x and y coordinate locations of the centroid, respectively. To ensure that the size of the discretization was of the same order as the radius of each circle, the radius was set equal to half of the average distance between all of the centroids in the model. In the event that the z-coordinate location of the centroid corresponded to the z-coordinate location of a segmentation, only the circular region in that segmentation was considered.

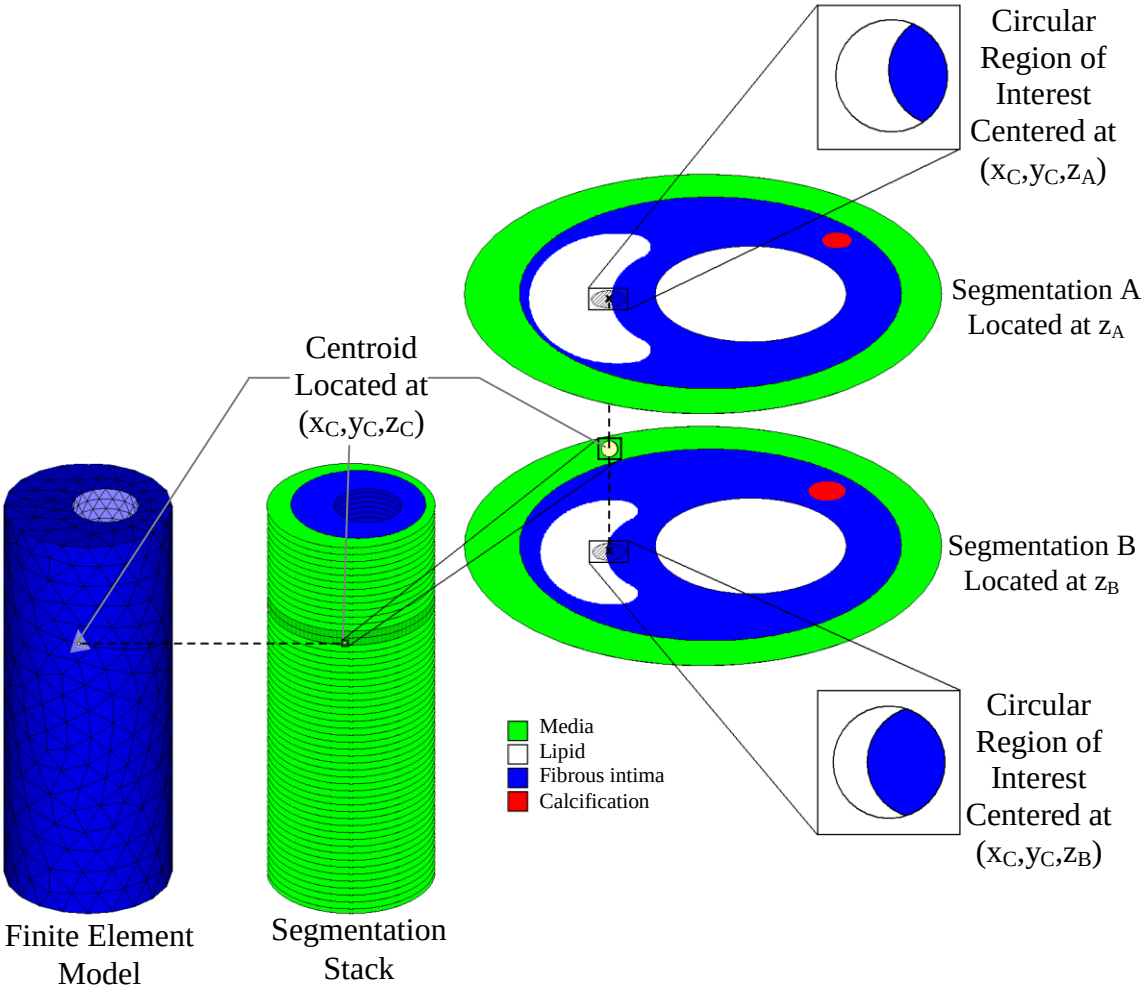

Figure 3.19. Steps followed to obtain regions of interest in segmentations used to calculate mechanical properties for each element.

Constituents were assumed to experience the same strains upon loading, meaning residual stresses in the no load state were neglected. Therefore, since the arterial tissue was considered a constrained mixture, the effective modulus in a circular region, E_O, was calculated based on

$$E_O = A_L E_L + A_M E_M + A_F E_F + A_c E_c \qquad \text{Equation 3.12}$$

where A_L, A_M, A_F, and A_C are the area fractions of lipid, media, fibrous intima, and calcification in a circular region, respectively and E_L, E_M, E_F, E_C are the elastic moduli of the lipid, media, fibrous intima, and calcification, respectively. Pixels classified as background were not included in the calculation of area fractions. Matlab was used to determine constituents' area fractions.

The elastic modulus for each element, E, was calculated using a linear interpolation scheme

$$E = \frac{(Z_C - Z_A)(E_O^B - E_O^A)}{Z_B - Z_A} + E_O^A \qquad \text{Equation 3.13}$$

where E_O^A and E_O^B are the elastic moduli of the circular regions in Segmentations A and B, respectively, Z_A and Z_B are the z locations of the two segmentations, and Z_C is the z-coordinate location of the element's centroid. After calculations were completed, the mechanical properties were imported into Ansys. The Matlab code used to calculate the distance between centroids and the elastic moduli of elements is included in Appendix B.

Modeling of Loading and Boundary Conditions

The mechanical property data used in our study are valid only over physiologic pressure ranges. Further, the deformation process over this range can be considered linear. Therefore, an incremental pressure increase of 40 mmHg was applied to the

luminal surface of the model (determined at the pressure-fixed configuration of 80 mmHg).

Due to geometrical non-linearity, the equations of equilibrium and boundary conditions must refer to the actual deformed configuration. Because of mechanical non-linearity, mechanical parameters such as linearized elastic moduli are strain dependent. In the adopted approach, the deformation process is considered a superposition of a relatively small deformation due to the pressure increase of 40 mmHg on a large deformation from the no-load state due to the transmural pressure of 80 mmHg. This study focuses on calculating stress resulting from the small deformation by accounting for the existing geometry and linearized moduli at 80 mmHg. The final stress, σ, due to the superposition of a small deformation on a large deformation is given by

$$\sigma = (E + 2\sigma')\varepsilon \qquad \text{Equation 3.14}$$

where E is the elastic modulus, ε is the final strain and σ' is the pre-stress due to the large deformation (Rachev et al., 2000). The effect of the stress due to the large deformation is neglected. Therefore, the pressure-fixed configuration was considered stress free. Neglecting the effects of existing stresses in this configuration when calculating stresses due to the applied pressure of 40 mmHg is justified given the constituents' elastic moduli are much higher than the wall stresses generated at a pressure of 80 mmHg.

Though the calculated stress field does not represent the true field existing at 120 mmHg, because the corresponding strains are relatively small (< 1%) and the mechanical response is linear, the stress field provides good information on stress distributions and relative magnitudes.

In this study, time-varying effects due to the viscoelasticity of constituents were

neglected and the deformation process was assumed to be quasistatic. The passive mechanical properties of arterial tissues have been shown to be practically insensitive to strain rate (Fung, 1993). Further, when arterial tissue undergoes physiologic deformations due to pulsatile pressure, inertial effects are negligible.

Also, shear stresses due to blood flow were neglected. This is justifiable given typical levels of fluid shear stress (approximately 1 to 1.5 Pa) are insignificant compared to typical wall stress levels (>10 kPa) (Huang, et al., 2001).

Boundary conditions must be applied in order to prevent rigid body motion. The model's extruded ends were constrained so that displacements and rotations were zero. Such an application of boundary conditions to extruded ends is beneficial because it provides good numerical stability, allows the complete reconstruction to be used, and reduces the high local stresses that are associated with constraining the model. This has been previously demonstrated by Carnell (2005).

Stress Calculations

After 3-D mechanical models were generated, stress distributions were obtained. Our interest focused on the distribution of von Mises stress in the arterial wall. This stress is commonly used and gives an appreciation of the overall magnitude of the stress tensor. The von Mises stress, σ_{vm}, is a stress-invariant and is a combination of components of both normal stresses (σ_x, σ_y, σ_z) and shear stresses (τ_{xy}, τ_{yz}, τ_{zx}). It is given by

$$\sigma_{vm} = \frac{\sqrt{(\sigma_x - \sigma_y)^2 + (\sigma_y - \sigma_z)^2 + (\sigma_z - \sigma_x)^2 + 6(\tau_{xy}^2 + \tau_{yz}^2 + \tau_{zx}^2)}}{\sqrt{2}}$$

Equation 3.15

In each 3-D model, stress distributions and magnitudes at axial locations distributed uniformly along the length at a spacing interval of 150 μm were considered. These axial locations, 345 in all, corresponded to the locations of the generated segmentations. Stresses at the axial locations were calculated using an interpolation scheme written in Matlab. Interpolation parameters, which were exported from Ansys into Matlab, included the stress values at the nodes in the 3-D model, coordinate locations of the nodes in the 3-D model, and coordinate locations of nodes from meshes generated at the axial locations of interest. Codes for importing Ansys files into Matlab and for interpolating data are provided in Appendix B. Stress distributions at axial locations were also plotted in Matlab and the code for this is likewise provided in Appendix B.

Once obtained, stresses at each axial location were tabulated and divided into quartiles by magnitude. The maximum stress was obtained and the average stress for the upper quartile was calculated. The Matlab code used to obtain maximum stresses and calculate upper quartile stress averages is provided in Appendix B.

Normalization of Stress

To facilitate comparison between different 3-D models, stresses in each 3-D model were normalized. For a given specimen, the maximum and average upper quartile stresses at axial locations distributed uniformly along the length at 150 μm intervals were normalized by the stress at the axial location in that specimen with the lowest severity of disease. Lowest lipid content and/or stenosis severity was equated to lowest disease severity.

Two-Dimensional Mechanical Modeling

For comparison purpose, 2-D FE models (n=345) were developed using the inner and outer boundaries from individual segmentations. Recall that these segmentations correspond to the axial locations considered in the 3-D models. The 2-D point clouds defining the boundaries in each segmentation were obtained, smoothed, and imported into Ansys as keypoints. Keypoints were used to define lines, which were used to define areas. These areas included the outer area and the lumen area. The lumen was eliminated using a Boolean operator.

Each 2-D model was meshed using plane strain elements (Ansys Element Number 42, Figure 3.20). The element is defined by 4 nodes having two degrees of freedom at each node: translations in the nodal x and y directions. Additional information on Ansys Plane 42 elements is provided in the Ansys 9.0 Theory Reference Manual (2004b) and the Ansys 9.0 Elements Reference Manual (2004a).

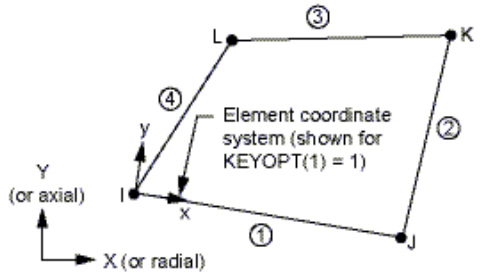

Figure 3.20. Ansys Plane 42 element geometry.

The theory of constrained mixtures was again used to assign an elastic modulus to each element. However, only one circular area was considered for each element. As with the 3-D model, boundary and loading conditions were applied and von Mises stress

distributions were obtained. For each 2-D model, the maximum von Mises stress was obtained and the average stress for the upper quartile was calculated.

Validation for Sectioning Interval

Histology's superior resolution makes possible the use of planar sections as a basis for constructing the most detailed three-dimensional computational models. One drawback, however, is that histologic procedures are time consuming with the most cumbersome steps being sectioning and staining. Thus, studies examining the appropriate sectioning interval were performed using models of a single specimen. These studies relied on methods previously discussed. Thus, it would have been inappropriate to present this validation discussion beforehand. In addition, because the studies were used in the development of our methodological approach, results and discussions of results specific to the validation approach are presented in this section as opposed to elsewhere in subsequent chapters.

Criteria were developed to determine the interval needed to generate surface reconstructions and the interval needed to generate finite element models. For surface generations, increases in the sectioning interval could not result in volumetric changes exceeding 5%. For finite element models, increases in the sectioning interval could not cause stress results to change by more than 10%.

Sections, 3 μm thick and collected at 30 μm intervals, were cut from a representative block. The sample embedded in this block had all of the constituents of interest present including healthy tissue, lipid, fibrous intima, and calcification. A total of 383 sections were sectioned and stained. The methods previously described were used to align and segment images of the stained sections. The aligned and segmented images

were analyzed to verify that relevant detail was not lost at an interval of 30 μm. The total number of pixels of each constituent were counted in every section. As is shown in Figure 3.21, variations took place gradually. Visual inspection confirmed that spatial changes likewise occurred slowly.

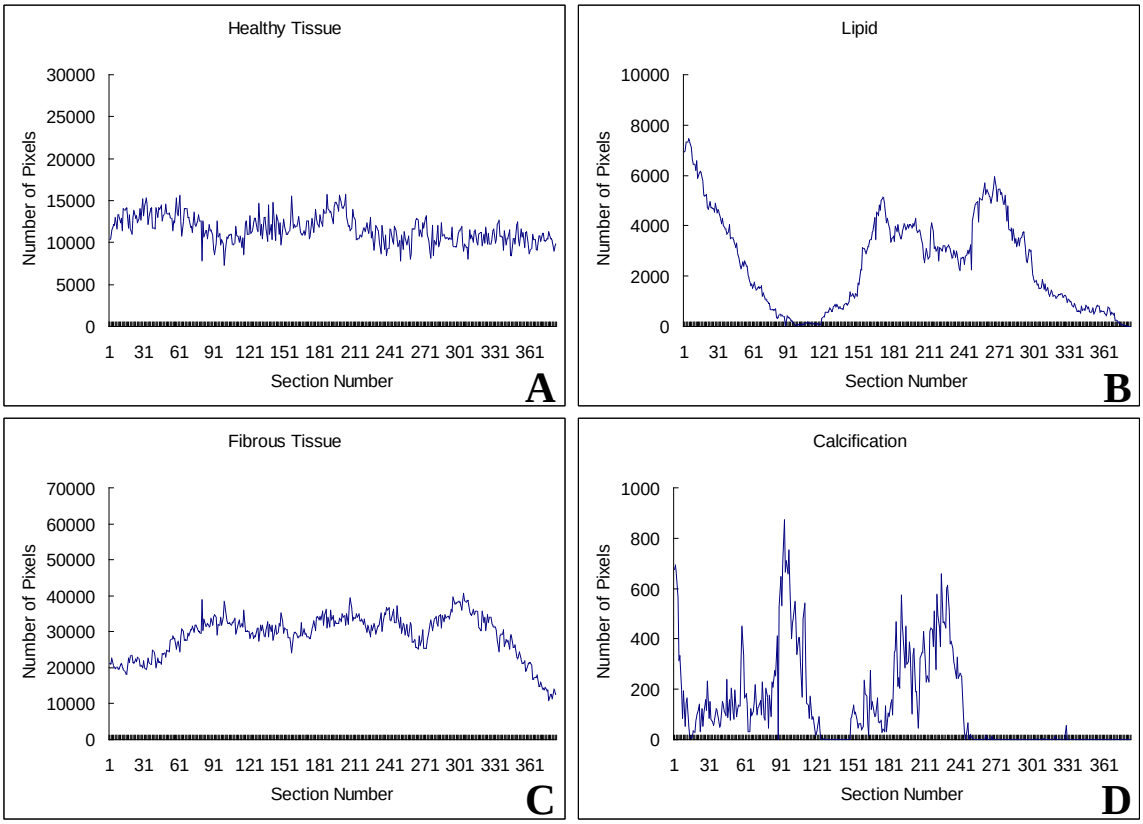

Figure 3.21. Total number of pixels of healthy tissue (A), lipid (B), fibrous intima (C), and calcification (D) in each section collected at an interval of 30 μm.

The interval needed to generate surface reconstructions was first determined. Luminal and outer wall surface reconstructions were created using the binary arterial wall images. Reconstructions were generated based on all sections, every 2nd section, every 3rd section, every 4th section, and every 5th section were generated. Downsizing beyond every 5th section was avoided. Such downsizing compromised the smoothness of

surfaces because too few points remained to perform noise reduction. To determine the effect of downsizing on geometric changes, the top and bottom of each surface were filled and the volumes were calculated. The volumes calculated based on all sections were compared to the volumes based on the downsized number of sections.

Table 3.3 shows that changes in volume of less than 2% occurred. Not only were changes in volume minimal, downsizing resulted in smoother surface reconstructions (Figure 3.22). Smoother surfaces are necessary because surface irregularities can lead to artificial stress concentrations in finite element models.

Table 3.3. Percent change in volume of outer wall and luminal reconstructions as a result of downsizing from all sections to every second, third, forth, or fifth section.

Comparison	Outer Wall (%)	Luminal (%)
All vs. Every 2nd	-0.07	0.42
All vs. Every 3rd	0.73	0.99
All vs. Every 4th	0.26	1.18
All vs. Every 5th	1.11	1.47

The interval needed to generate finite element models was next determined. Five finite element models were developed using the methods previously described and the von Mises stress results for each were compared. A solid model was created from the surface reconstructions based on every 5th section. The model was meshed with 35,070 elements and boundary and loading conditions were applied. From this model, five models each having unique mechanical properties were generated. Mechanical properties were calculated using segmentations of stained sections. Calculations were based on all sections, every 2nd section, every 3rd section, every 4th section, and every 5th section. The

models were solved and von Mises stresses were compared. Stresses at every element in each model were tabulated and divided into quartiles by magnitude. The quartile results based on all sections were compared to those based on the downsized number of sections.

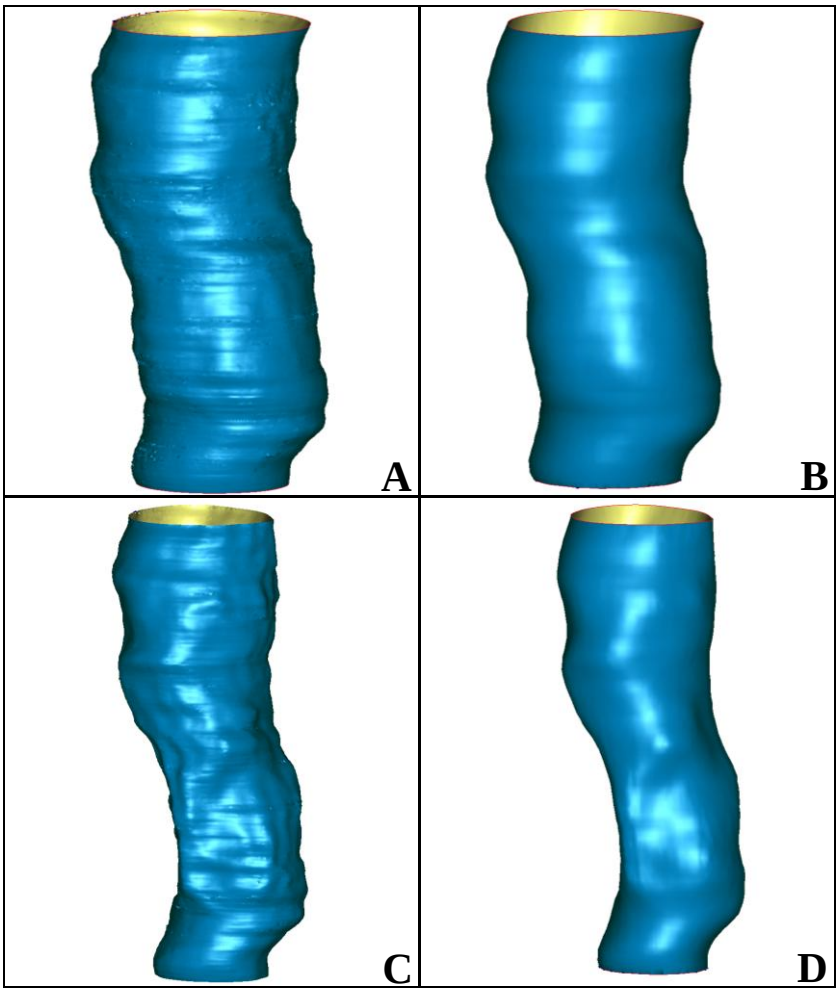

Figure 3.22. Reconstructions of the outer wall surface based on every section (A) and every 5th section (B) and of the luminal surface based on every section (C) and every 5th section (D).

Table 3.4 shows that the mean stress varied by no more than 1.8 ± 0.7%, the maximum by no more than 4.7%, and the minimum by no more than 1.3%.

Table 3.4. Percent change in mean, maximum, and minimum von Mises stress (35,070 elements). Quartile 1 (Q1) represents the highest stress values.

von Mises Stress Value	Percent Change in Stress due to Downsizing to Every: 2nd Section	3rd Section	4th Section	5th Section
Q1: Mean ± SD	1.0 ± 1.5	0.6 ± 0.1	0.6 ± 0.2	0.1 ± 0.5
Q2: Mean ± SD	0.1 ± 2.0	0.0 ± 1.8	-0.1 ± 1.2	-0.1 ± 1.7
Q3: Mean ± SD	-0.8 ± 1.4	0.9 ± 1.3	-0.9 ± 0.7	-0.8 ± 0.3
Q4: Mean ± SD	-0.4 ± 0.5	0.6 ± 0.3	1.0 ± 0.1	-1.8 ± 0.7
Q1: Maximum	-2.6	-3.7	-4.0	4.7
Q2: Maximum	0.9	0.6	0.4	0.4
Q3: Maximum	-0.4	-0.2	0.0	-0.2
Q4: Maximum	-0.3	-0.7	-0.7	-1.3
Q1: Minimum	0.9	0.6	0.4	0.4
Q2: Minimum	-0.4	-0.3	0.0	-0.2
Q3: Minimum	-0.3	-0.7	-0.7	-1.3
Q4: Minimum	0.0	0.0	0.0	0.0

Stress results were also analyzed in a cross-section located in the center of the model. As is shown in Figure 3.23, the distribution of stress in this corresponding cross-section was similar for each model. Stress magnitudes were likewise similar in the cross-section. Stresses at every element in this cross-section were tabulated and divided into quartiles. The quartile results based on all sections were compared to those based on the downsized number of sections.

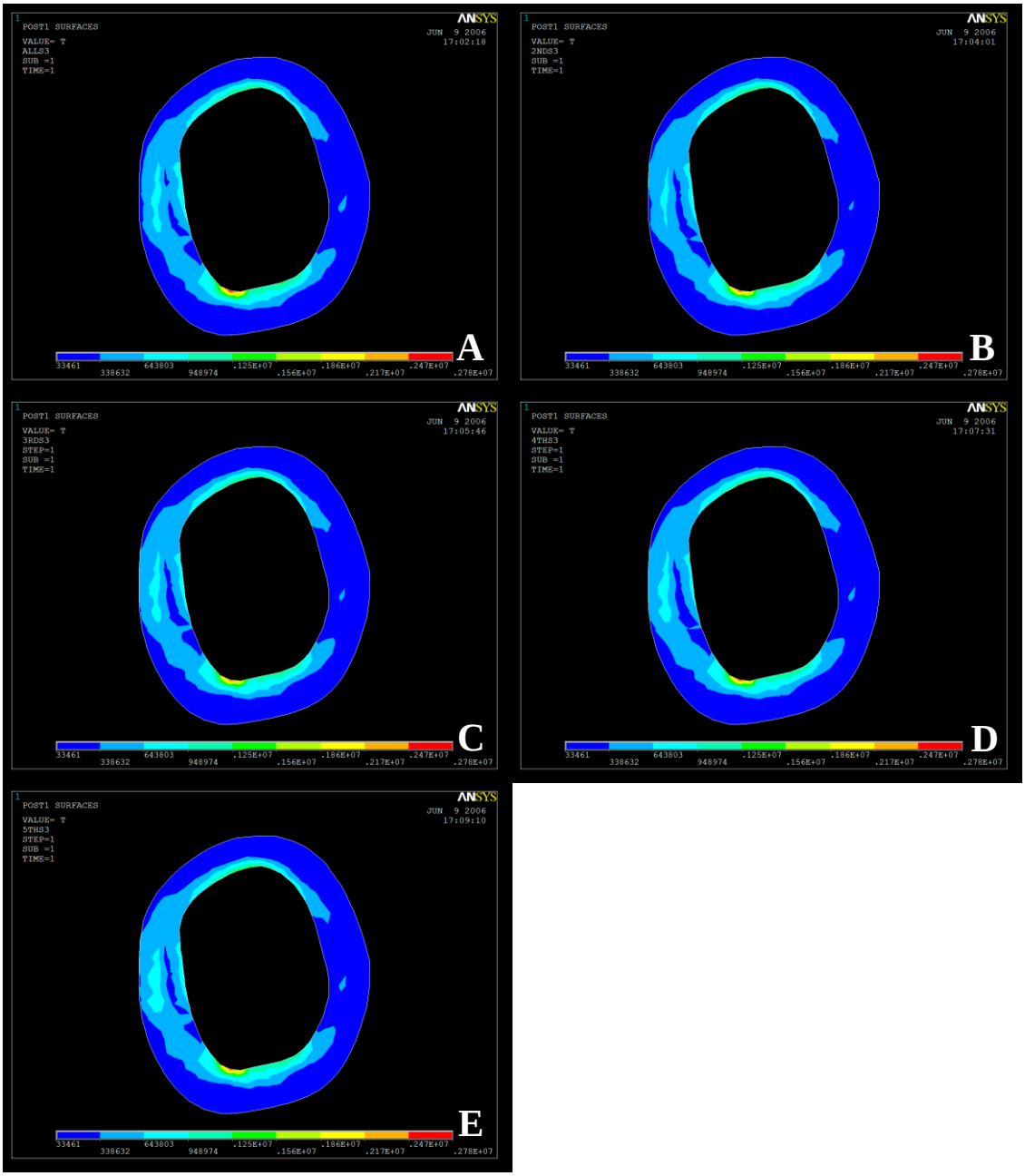

Figure 3.23. Von Mises stress distribution in a corresponding cross-section from models based on all sections (A), every 2nd section (B), every 3rd section (C), every 4th section (D), and every 5th section (E).

Table 3.5 shows that the mean stress varied by 2.8 ± 8.4%, the maximum by 7%, and the minimum by 2.8% in the most severe cases.

Table 3.5. Percent change in mean, maximum, and minimum von Mises stress (corresponding center cross-section). Quartile 1 (Q1) represents the highest stress values.

von Mises Stress Value	Percent Change in Stress due to Downsizing to Every: 2nd Section	3rd Section	4th Section	5th Section
Q1: Mean ± SD	3.1 ± 6.9	2.8 ± 8.4	2.9 ± 8.1	1.2 ± 5.9
Q2: Mean ± SD	2.3 ± 7.4	-1.1 ± 8.4	-1.9 ± 7.7	-3.1 ± 3.7
Q3: Mean ± SD	-0.5 ± 6.6	-1.9 ± 3	-1.1 ± 6.4	-3.5 ± 6.7
Q4: Mean ± SD	2.5 ± 0.3	2.0 ± 3.7	2.4 ± 4.5	-0.3 ± 0.8
Q1: Maximum	6.4	7.0	6.9	6.0
Q2: Maximum	2.5	-0.3	-1.0	-2.9
Q3: Maximum	0.6	-1.4	-0.7	-1.9
Q4: Maximum	1.0	0.5	0.4	-2.4
Q1: Minimum	2.8	0.0	-0.1	-2.1
Q2: Minimum	0.7	-1.5	-0.5	-1.8
Q3: Minimum	0.8	0.6	0.5	-2.5
Q4: Minimum	-0.2	0.4	2.2	1.3

To validate that mesh refinement would not affect the stress results, the mesh density was roughly doubled to 62,795 elements. Results from a model based on all sections were compared to those from a model downsized by the most extreme amount; that is a model based on every 5th section. Table 3.6 confirms that mesh refinement had little effect on percent changes. Collectively, these results suggested that a sampling interval of 150 μm was suitable not only for the generation of surface reconstructions, but also for the generation of finite element models.

Table 3.6. Percent change in mean, maximum, and minimum von Mises stress (62,795 elements). Quartile 1 (Q1) represents the highest stress values.

von Mises Stress Values	All vs. Every 5th (%)
Q1: Mean ± SD	0.1 ± 0.8
Q2: Mean ± SD	-0.2 ± 1.6
Q3: Mean ± SD	-1.2 ± 0.1
Q4: Mean ± SD	-3.3 ± 1.3
Q1: Maximum	0.6
Q2: Maximum	0.6
Q3: Maximum	-0.6
Q4: Maximum	-1.1
Q1: Minimum	0.6
Q2: Minimum	-0.6
Q3: Minimum	-1.1
Q4: Minimum	0.0

Specific Aim III:

Determine whether correlations between stress results from 3-D mechanical models and plaque features exist and whether these stress results are consistent with results from 2-D mechanical models.

While there are numerous plaque features that could have been investigated, in this study, we focused on five. Recall that the goal of determining whether correlations exist is to gain insights into plaque stability assessments. A major advantage of this study is that longitudinal variations are accounted for. Therefore, we first investigated the effect of longitudinal variations. We then studied the effects of fibrous cap thickness and lipid pool content. Both are morphological features associated with plaque rupture.

Finally, we investigated the effects of stenosis severity and calcification content. These features are associated with disease progression, but have not been linked to rupture.

Longitudinal Variation

To provide evidence that failure to account for longitudinal variations in geometry and mechanical properties leads to inaccurate stress predictions, differences between stress predictions from the 3-D FE models and 2-D models were compared.

Fibrous Cap Thickness

Fibrous cap thickness is defined as the minimum distance from the boundary of lumen to the inner border of the lipid pool (Zheng et al., 2005). Fibrous cap thickness values at axial locations distributed uniformly along the length at 150 μm intervals were determined. To accomplish this, in each segmentation the center of the lumen was first determined. Next, measurements of the distances between the lumen's boundary and the inner border of the lipid pool were taken in a radial direction from the center of the lumen. The minimum distance measurement was determined and equaled the fibrous cap thickness. The Matlab code used to calculate the fibrous cap thickness is included in Appendix B.

Based on the finding of Burke and colleagues (1997), we compared the differences between normalized stresses at axial locations in which the fibrous cap thickness was less than 65 μm and at axial locations in which the fibrous cap thickness was greater than 65 μm. We also tested for a correlation between the fibrous cap thickness and normalized stress levels.

Lipid Content

Lipid content values at axial locations distributed uniformly along the length at 150 μm intervals were determined. To accomplish this, the area fraction of lipid (A_L), or lipid content, in each segmentation was calculated using the following equation

$$A_L = \frac{P_L}{P_L + P_M + P_F + P_C} \qquad \text{Equation 3.16}$$

where P_L, P_M, P_F, and P_C represent the total number of pixels classified as lipid, media, fibrous intima, and calcification, respectively. The Matlab code used to count pixels and calculate lipid content is included in Appendix B.

We compared the differences between normalized stresses at axial locations in which lipid was present and at axial locations void of lipid. We also tested for a correlation between the amount of lipid and normalized stress levels.

Stenosis Severity

Stenosis severity values at axial locations distributed uniformly along the length at 150 μm intervals were determined. To accomplish this, the stenosis severity (percentage of stenosis) in each segmentation was calculated using the following equation

$$\text{percentage of stenosis} = \frac{A_{Le}}{A_{IEL}} \times 100 \qquad \text{Equation 3.17}$$

where A_{Le} and A_{IEL} represent the lesion area and the internal elastic lamina area, respectively (Glagov, et al., 1987). The internal elastic lamina area is defined as the lesion area plus the lumen area. In the presence of advanced disease, the internal elastic lamina is often discontinuous or absent. Therefore, in this study, it was assumed that the

internal elastic lamina coincided with the inner edge of the largest region of media. The Matlab code used to calculate the stenosis severity is provided in Appendix B.

Based on the finding of Glagov and colleagues (1987), we compared the differences between normalized stresses at axial locations in which stenosis severity was greater than 40% and at axial locations in which stenosis severity was less than 40%. We also tested for a correlation between stenosis severity and normalized stress levels.

Calcification Content

Calcification content values at axial locations dispersed uniformly along the length at 150 μm intervals were determined. To accomplish this, the area fraction of calcification (A_C), or calcification content, in each segmentation was calculated using the following equation

$$A_C = \frac{P_C}{P_L + P_M + P_F + P_C} \qquad \text{Equation 3.18}$$

where P_L, P_M, P_F, and P_C represent the total number of pixels classified as lipid, media, fibrous intima, and calcification, respectively. The Matlab code used to count pixels and calculate calcification content is included in Appendix B.

We compared the differences between normalized stresses at axial locations in which calcification was present and at axial locations void of calcification. We also tested for a correlation between the amount of calcification and normalized stress levels.

Statistics

All data are reported as mean ± one standard deviation unless otherwise stated. Statistical analyses were performed using Minitab Release 12.23 (Minitab Inc., State College, PA). The Anderson-Darling normality test was used to determine if data were

normally distributed. For two sets of data with normal distributions, an unpaired *t* test was used to determine differences. If normality tests failed, a Wilcoxon rank sum test was used. p values < 0.05 were considered significant for concluding that data sets had different means (*t* test) or medians (Wilcoxon rank sum test).

To test for a correlation between a plaque feature measurement (fibrous cap thickness, lipid content, stenosis severity, or calcification content) and normalized stress levels, the nonparametric Spearman rank correlation test was used. This test was selected since stress and plaque feature measurements were independent calculations that could not be controlled. A Spearman rank correlation coefficient of 0 signifies no correlation, of 1.0 signifies a perfect positive correlation, and of -1.0 signifies a perfect negative correlation. p values < 0.05 were considered statistically significant.

CHAPTER 4:

RESULTS

The goals of this research were to develop three-dimensional (3-D) mechanical models of human coronary atherosclerotic plaques based on minimally distorted, serial histologic sections and to use these models to determine the effects of plaque features on 3-D stress results. In this chapter, we show that these goals were accomplished by presenting the results that were obtained. As with the previous chapter, this chapter is divided into three major sections, which correspond to each of the specific aims.

Specific Aim I:

Quantify and correct for histologic distortions to achieve more accurate mechanical models of arteries.

Micro-CT and Histology Images

A representative example of a cross-section captured in its fresh, embedded, and sectioned and stained state is shown in Figure 4.1. The luminal boundary and the outer-wall boundary are apparent in each image. In addition, the four registration marks are identifiable in the embedded state and sectioned and stained state images.

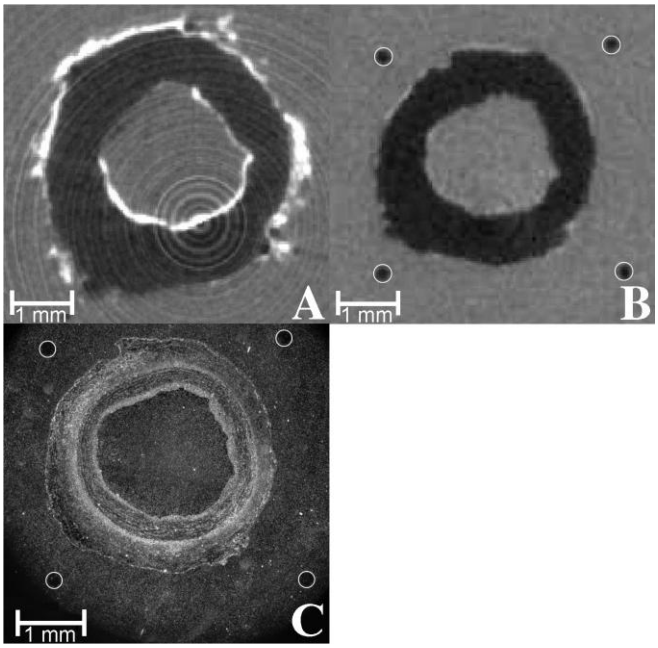

Figure 4.1. Cross-sectional images of an artery in its fresh (A), embedded (B), and sectioned and stained state (C). A and B are micro-computed tomography images and C is a light microscopy image. Registration marks have been highlighted for emphasis.

Shrinkage and Sectioning Distortions

Table 4.1 shows the lengths and cross-sectional area changes for the five arteries examined in this study. Tissue shrinkage due to fixation, processing, and embedding was significant. Comparing the fresh tissue to the embedded tissue, length decreased by 6.4 ± 2.3 % ($p = 0.009$, $n=5$) and cross-sectional area decreased by 35.4 ± 5.0 % ($p < 0.001$, $n=5$). The strains induced by sectioning were likewise obtained for the same 5 arteries. These data are shown in Table 4.1 as the principal strains. The angle between the principal direction and the cutting direction is also shown. The small magnitude of this angle shows that the sectioning direction and the principal strain direction were approximately aligned. Furthermore, knowledge of the angle and strains allowed for calculation of strain in the sectioning direction and perpendicular to the sectioning

direction. The strain in the sectioning direction was compressive and averaged 0.067 ± 0.011 (n=5) and the strain in the direction perpendicular to sectioning was compressive and averaged 0.023 ± 0.005 (n=5). The compressive result in both directions is not counterintuitive given that these strains are the outcome of distortions from cutting as well as from floating on the water bath.

Table 4.1. Summary of distortions due to histologic preparation including axial and cross-sectional area shrinkage, and principal strains (ε_1 and ε_2). Also included is the angle between the principal strain direction and the cutting direction (ϕ).

Artery No.	Axial Shrinkage (% of fresh)	Cross-Sectional Area Shrinkage (% of fresh)	ε_1	ε_2	ϕ
1	3.8	37.7 ± 3.1	-0.020 ± 0.011	-0.057 ± 0.025	-5.3 ± 8.4^o
2	6.9	33.4 ± 0.8	-0.023 ± 0.008	-0.072 ± 0.017	-5.3 ± 0.3^o
3	4.5	27.6 ± 7.4	-0.025 ± 0.005	-0.068 ± 0.010	-1.3 ± 3.9^o
4	7.1	38.1 ± 1.6	-0.022 ± 0.007	-0.059 ± 0.009	-1.7 ± 11.6^o
5	9.6	40.1 ± 1.7	-0.025 ± 0.021	-0.084 ± 0.026	-3.0 ± 3.0^o

Distortion Correction

A representative visual display of the correction of distortion in an arterial cross-section is shown in Figure 4.2. Segmented images of the artery in its fresh state, embedded state, and sectioned and stained state are shown. Reconstructions in which the sectioning artifact and the shrinkage artifact have been corrected are also presented. Table 4.2 shows the errors associated with the corrected reconstructions for each artery. Comparing the embedded images to the sectioning artifact corrected reconstructions gives an average error of +1.6 ± 0.5% (n=5) associated with the sectioning correction

while comparing the fresh images to the shrinkage artifact corrected reconstructions gives an average error of +4.0 ± 1.7% (n=5).

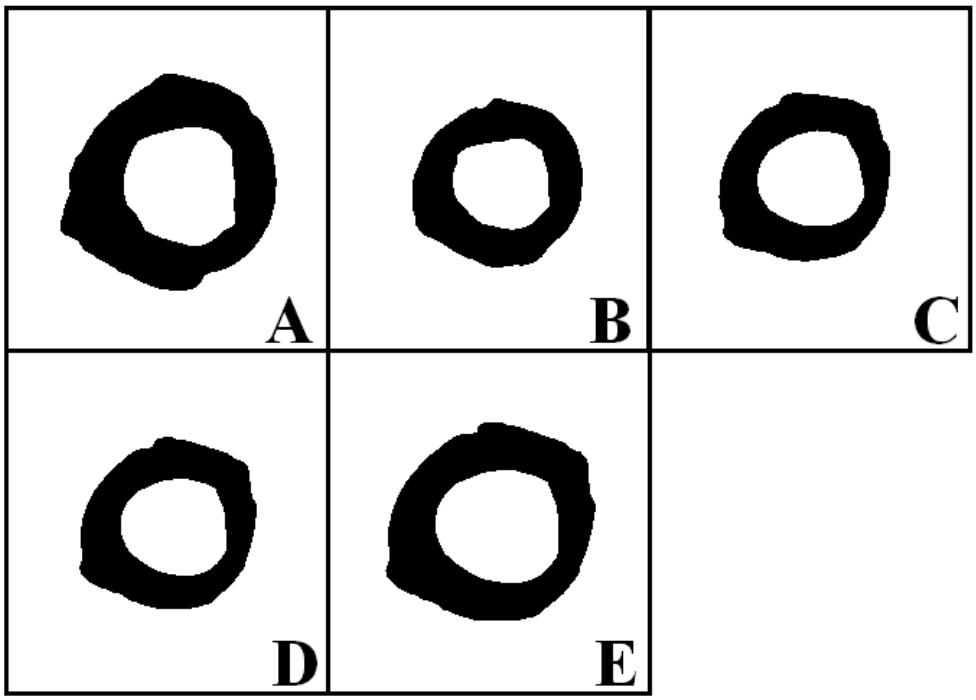

Figure 4.2. Corresponding segmented cross-sectional images of an artery in its fresh state (A), embedded state (B), and sectioned and stained state (C), and reconstructions of the sectioning artifact corrected state (D), and shrinkage artifact corrected state (E).

Table 4.2. Summary of sectioning and shrinkage correction associated errors.

Artery No.	Sectioning Correction Error (%)	Shrinkage Correction Error (%)
1	1.2 ± 0.8	2.5 ± 2.3
2	1.7 ± 1.3	2.6 ± 0.5
3	1.0 ± 1.1	6.7 ± 4.0
4	1.9 ± 1.0	4.1 ± 1.0
5	2.2 ± 0.6	3.9 ± 1.1

Comparison of Methyl Methacrylate and Paraffin

Recall that models of corresponding cross-sections and serial sections were generated. Table 4.3 summarizes the results for the corresponding cross-section models. Compared to the fresh case, the maximum stress was underestimated by 7% for the methyl methacrylate (MMA) case, overestimated by 3% for the distortion-corrected MMA case, and overestimated by 200% for the paraffin case. Table 4.4 summarizes the results for the serial section models. The average maximum stress in the paraffin models was 554.8 ± 113.2 and in the MMA models was 194.2 ± 13.6.

Table 4.3. Maximum stress in corresponding cross-section models.

Model	Max Stress (kPa)
Fresh	202.9
MMA	189.2
MMA-Corrected	208.8
Paraffin	608.9

Table 4.4. Maximum stress in serial MMA and paraffin cross-section models. Section 1 is approximately corresponding.

Section	Paraffin (kPa)	MMA (kPa)
1	608.9	189.2
2	462.5	180.9
3	503.2	214.5
4	471.1	185.4
5	728.4	201.0

Specific Aim II:

Develop three-dimensional mechanical models of human coronary atherosclerotic plaques based on minimally distorted histologic sections.

Specimens

Each of the five specimens was assigned a name. The age, sex, medication history, and medical history of each recipient from which the specimen was collected are given in Table 4.5 along with naming information.

Table 4.5. Characteristics of patients from which specimens were collected.

Specimen Name	Age	Sex	Medications	History
A	44	Male	Coreg K-Dur Aldactone Demadex Coumadin ASA Protonix	Congestive Heart Failure Atrial Fibrillation Hypercholesterolemia Dilated Cardiomyopathy
B	59	Male	Amiodarone Losartan Aspirin Coumadin Spironolactone Furosemide Ambien Milrinone Citalopram	Idiopathic Dilated Cardiomyopathy
C	44	Male	Milrinone Toprol Coumadin Demadex Amiodarone Lanoxin Zocor	Ischemic Cardiomyopathy Myocardial Infarction Coronary Artery Bypass Graft
D	43	Male	Amiodarone Elanapril Coumadin Prednisone Imdur Aldactone Singulair Advair Flovent Tessalon	Hypertrophic Cardiomyopathy Increased Abdominal Girth Weight Gain Acute Renal Failure
E	44	Male	-	Congestive Heart Failure Congenitally Malformed Trileaflet Valve

Additionally, the American Heart Association (AHA) classification (Stary, et al., 1995; Stary, et al., 1994) and modified AHA classification (Virmani, et al., 2000) of each specimen are provided in Table 4.6. This table shows that the sample population in our study reflected a broad range of disease severity.

Table 4.6. Classification of specimens.

Specimen Name	AHA Classification	Modified AHA Classification
A	Initial	Intimal thickening
B	Intermediate	Fibrous cap atheroma
C	Atheroma	Thin fibrous cap atheroma
D	Atheroma	Thin fibrous cap atheroma
E	Fibroatheroma	Fibrocalcific plaque

Three-Dimensional Mechanical Models

A summary of the geometric characteristics of the models of each specimen, including the average inner diameter, average outer diameter, and length (not including the extruded end lengths) is provided in Table 4.7. Figure 4.3 - Figure 4.7 show the models that were generated.

Table 4.7. Geometric characteristics of models.

Specimen Name	Inner Diameter (μm)	Outer Diameter (μm)	Length (μm)
A	2800 ± 100	3820 ± 100	9900
B	2220 ± 120	3280 ± 110	8250
C	3440 ± 190	4870 ± 120	13050
D	3650 ± 260	5030 ± 280	11100
E	3640 ± 400	5530 ± 320	12600

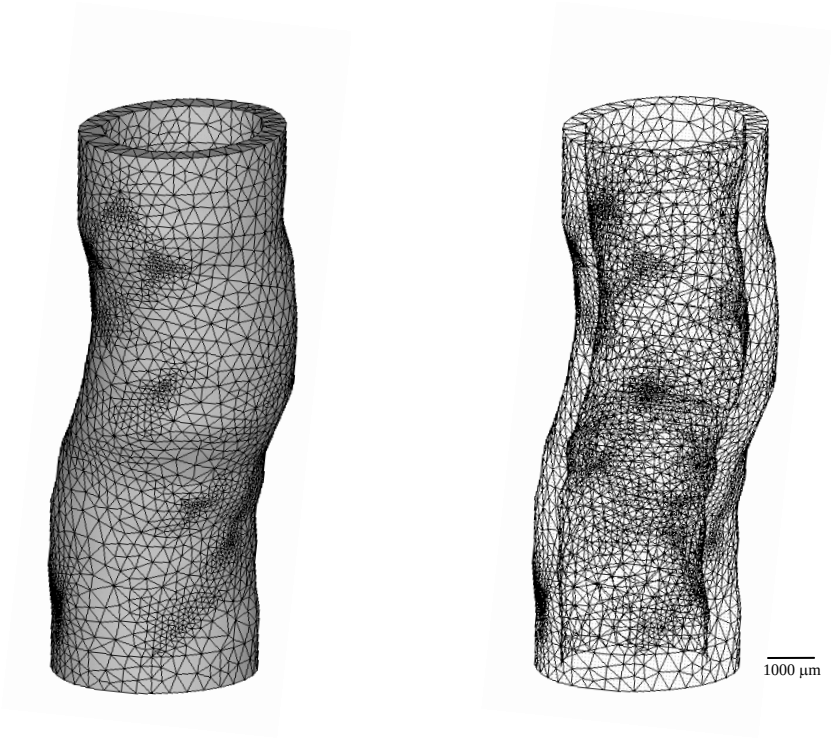

Figure 4.3. Solid and skeleton views of the model of Specimen A.

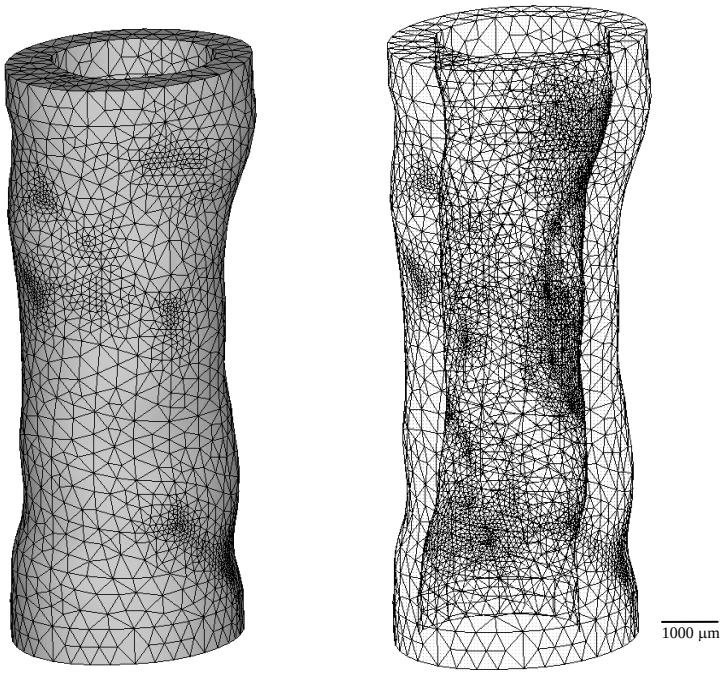

Figure 4.4. Solid and skeleton views of the model of Specimen B.

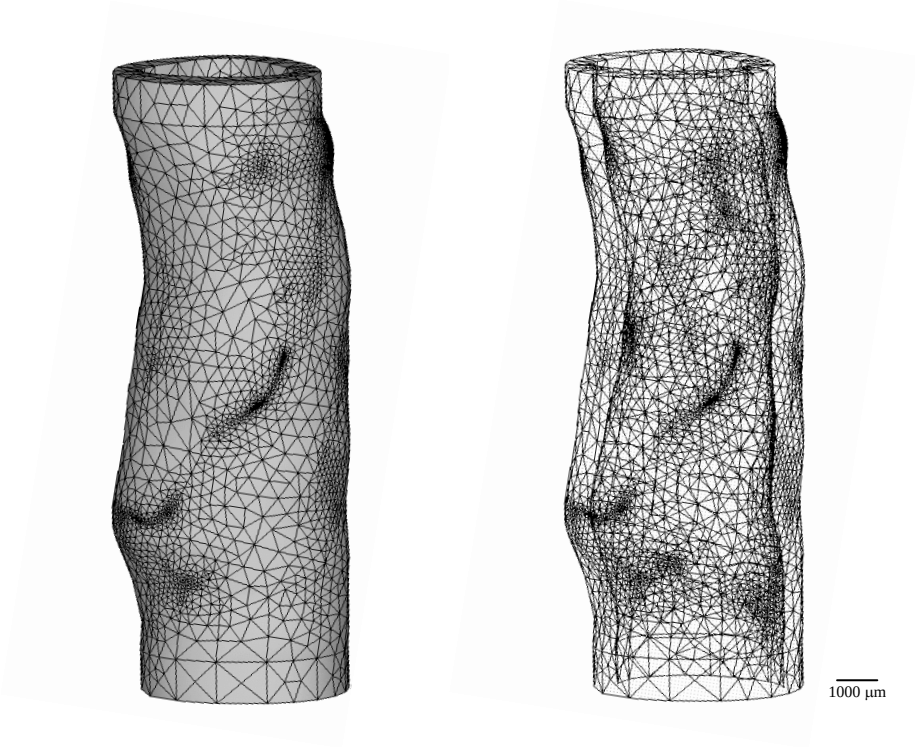

Figure 4.5. Solid and skeleton views of the model of Specimen C.

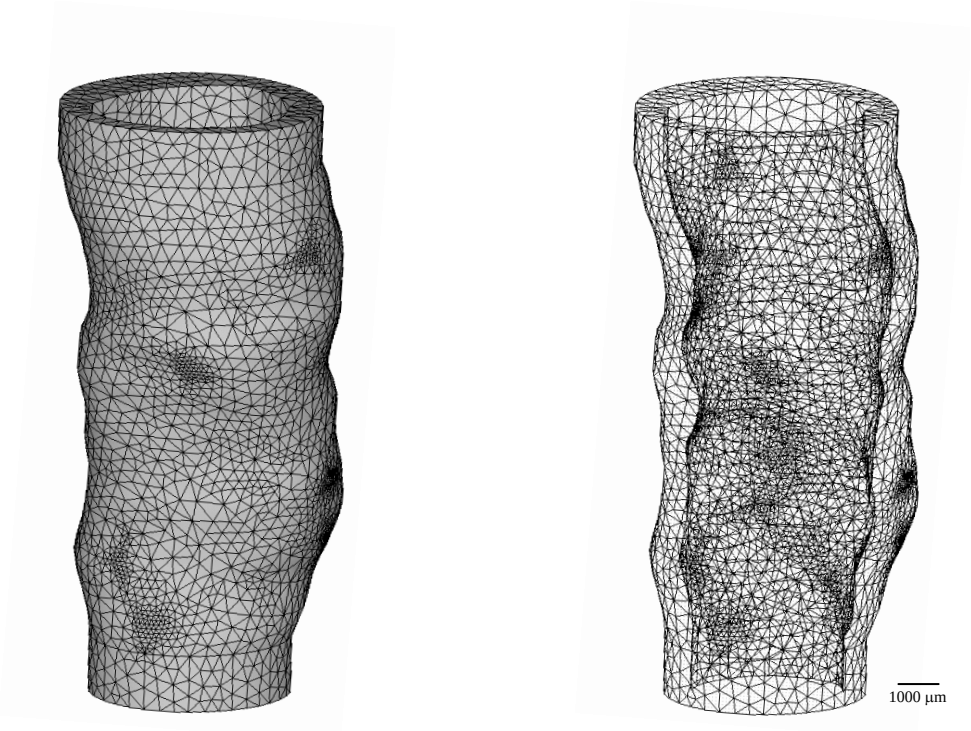

Figure 4.6. Solid and skeleton views of the model of Specimen D.

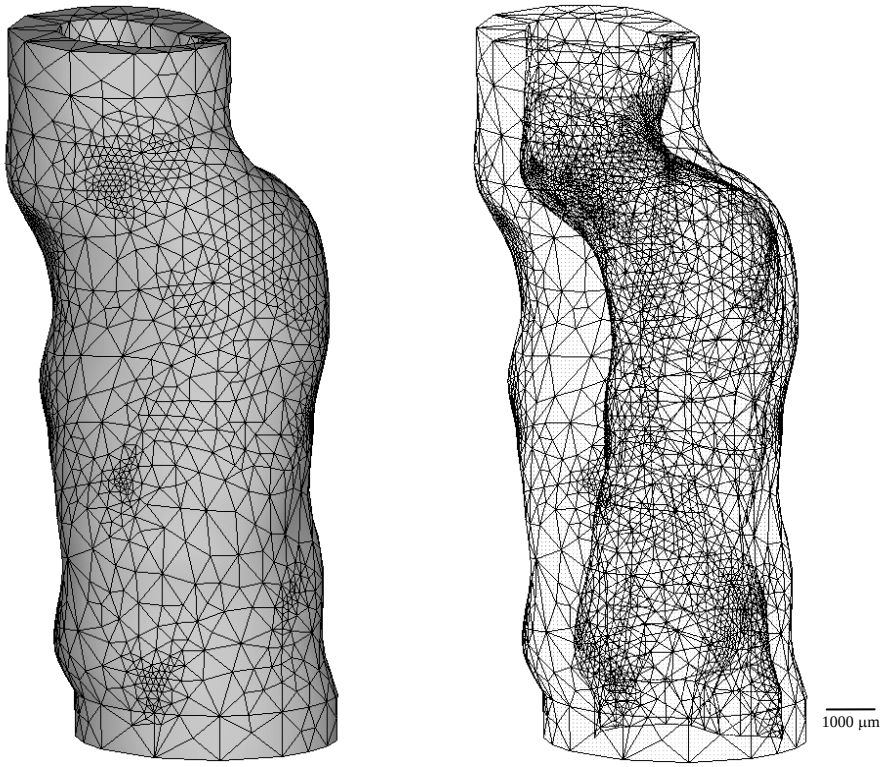

Figure 4.7. Solid and skeleton views of the model of Specimen E.

Specific Aim III:

Determine whether correlations between stress results from 3-D mechanical models and plaque features exist and whether these stress results are consistent with results from 2-D mechanical models.

In this section of the chapter, 3-D stress results for each specimen are presented in the first subsection. In the next, the results from 3-D models of individual specimens are compared to results from corresponding 2-D models. The following subsection presents results showing the effects of fibrous cap thickness, lipid content, stenosis severity, and calcification content on normalized stress predictions from 3-D models. In the final subsection, results on additional comparisons between stresses from 3-D models and 2-D

models are given. This time, the effects of those plaque features, which are specifically associated with plaque rupture, on 3-D model versus 2-D model stress predictions are considered.

Three-Dimensional Distribution of Stress

Figure 4.8 – Figure 4.12 show the von Mises stress distributions for each of the 3-D models. Each model was cut open to reveal distributions along the luminal surface. Therefore, the cutting plane is also depicted in these figures. In Specimen A (Figure 4.8), which had no fibrous cap, stresses were almost uniformly distributed. In Specimens B (Figure 4.9), C (Figure 4.10), and D (Figure 4.11), stress concentrations typically occurred in the shoulder regions of the plaques. In Specimen E (Figure 4.12), stresses were concentrated in the thinnest portions of the arterial wall.

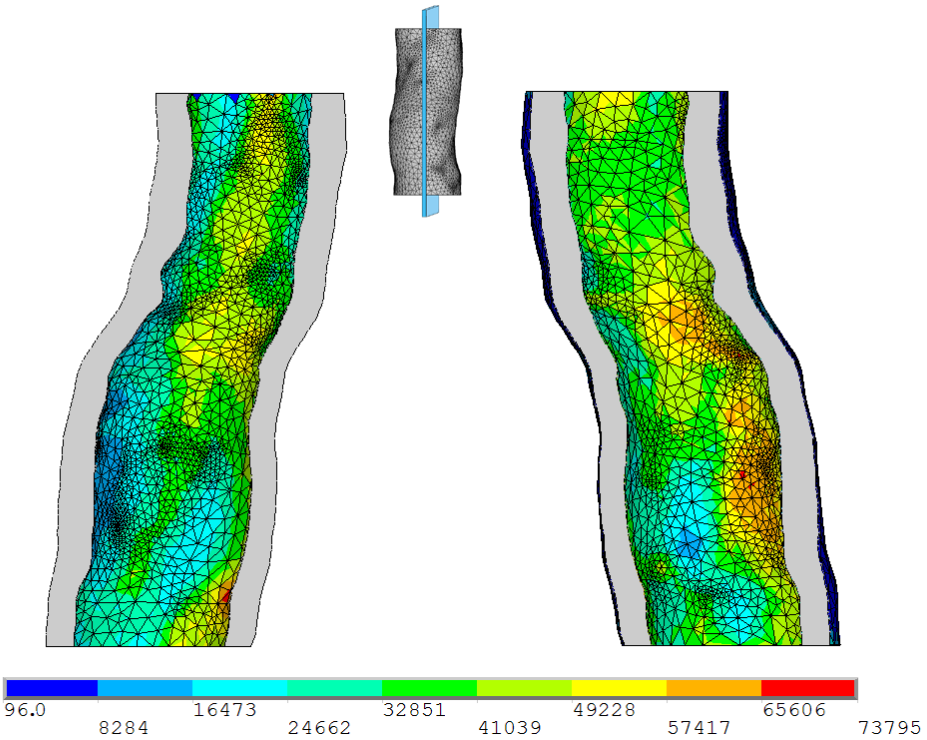

Figure 4.8. von Mises stress distribution in Pa for 3-D model of Specimen A. The cutting plane is depicted in the small model in the center.

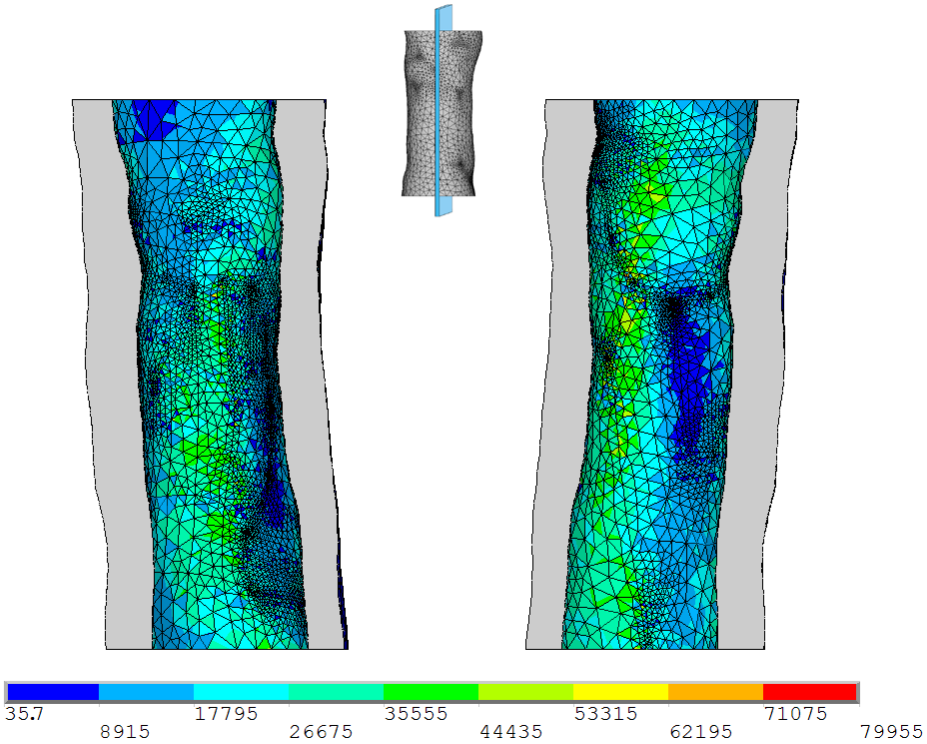

Figure 4.9. von Mises stress distribution in Pa for 3-D model of Specimen B. The cutting plane is depicted in the small model in the center.

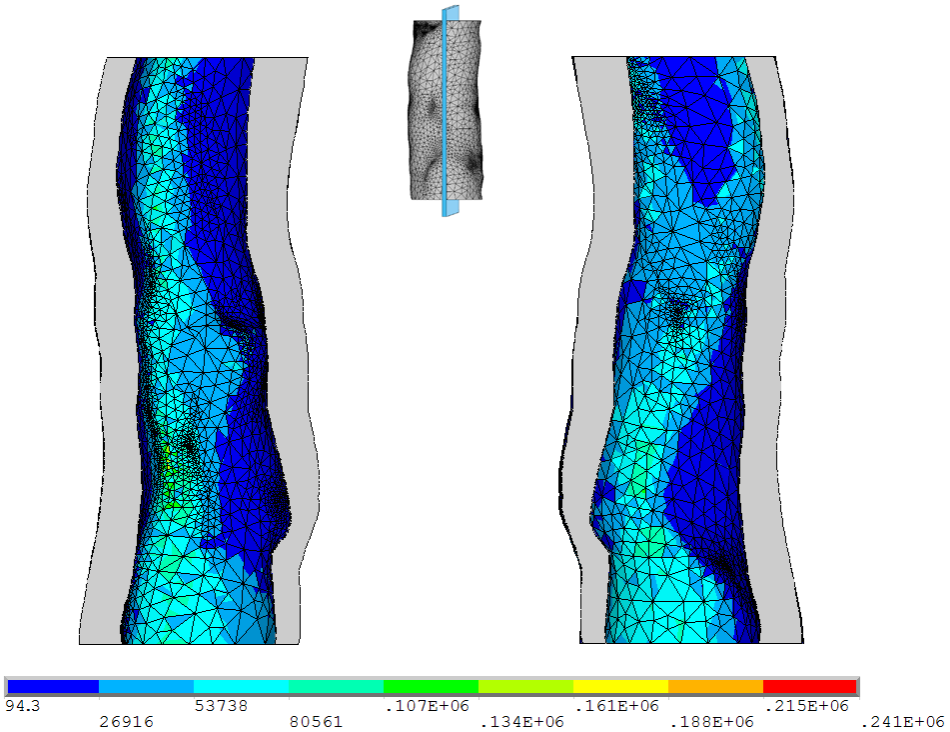

Figure 4.10. von Mises stress distribution in Pa for 3-D model of Specimen C. The cutting plane is depicted in the small model in the center.

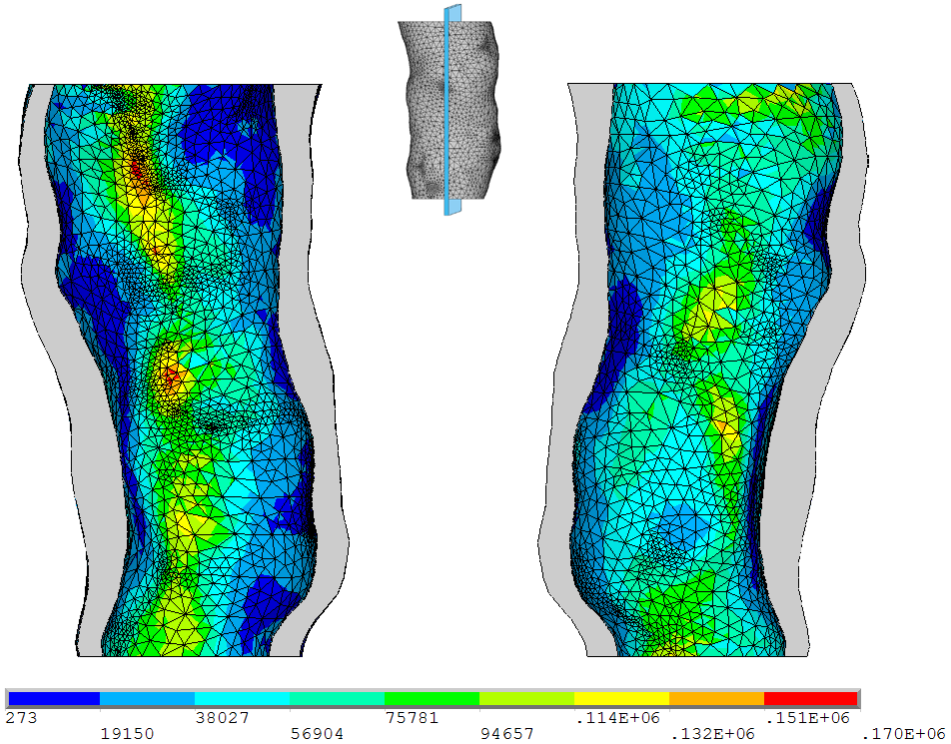

Figure 4.11. von Mises stress distribution in Pa for 3-D model of Specimen D. The cutting plane is depicted in the small model in the center.

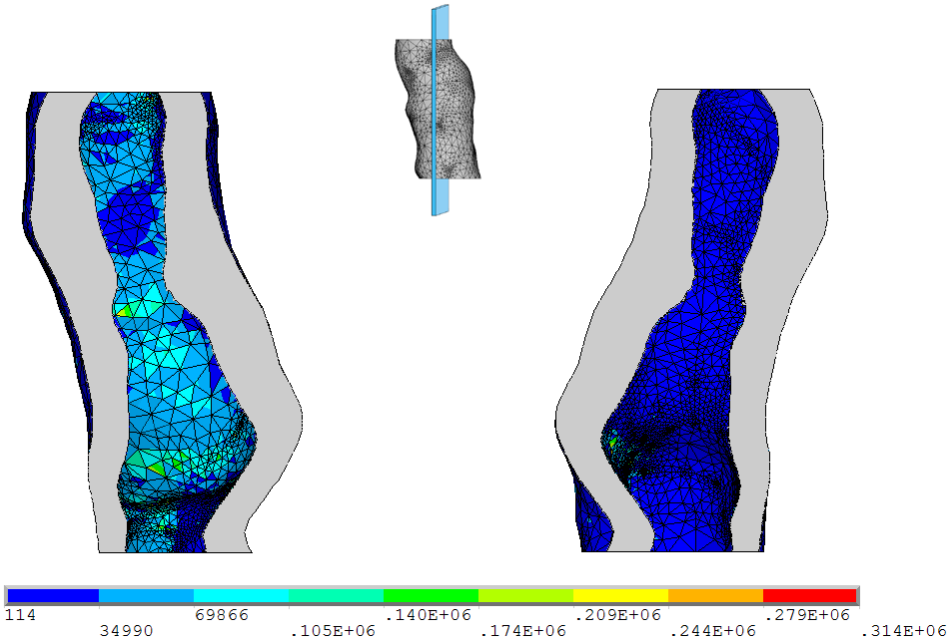

Figure 4.12. von Mises stress distribution in Pa for 3-D model of Specimen E. The cutting plane is depicted in the small model in the center.

Stress Predictions from 3-D versus Plane Strain Models

Stress predictions from each 3-D FE model were compared to predictions from 2-D, plane strain models based on individual histologic sections. Recall that stress results from 3-D and plane strain models were obtained at axial locations dispersed uniformly along the length of each specimen. At every axial location, the maximum stress was determined and upper quartile stress average was calculated. It was not necessary to normalize these stress results, because differences within a specimen rather that between specimens were being considered. Figure 4.13 shows a comparison between mean upper quartile stresses and Figure 4.14 shows a comparison between mean maximum stresses. For all five specimens, A (n=71), B (n=47), C (n=81), D (n=69), and E (n=77), stress predictions in the 3-D models were significantly lower ($p < 0.05$) than stress predictions in the plane strain models.

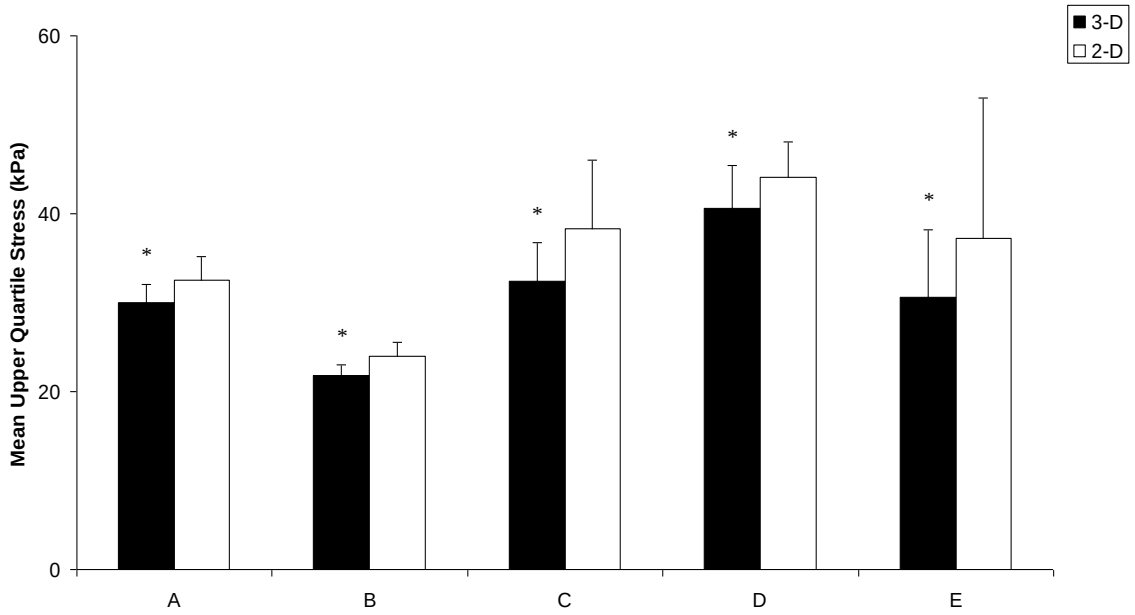

Figure 4.13. Mean upper quartile stress in 3-D versus plane strain models. * denotes a significance difference at $p < 0.05$.

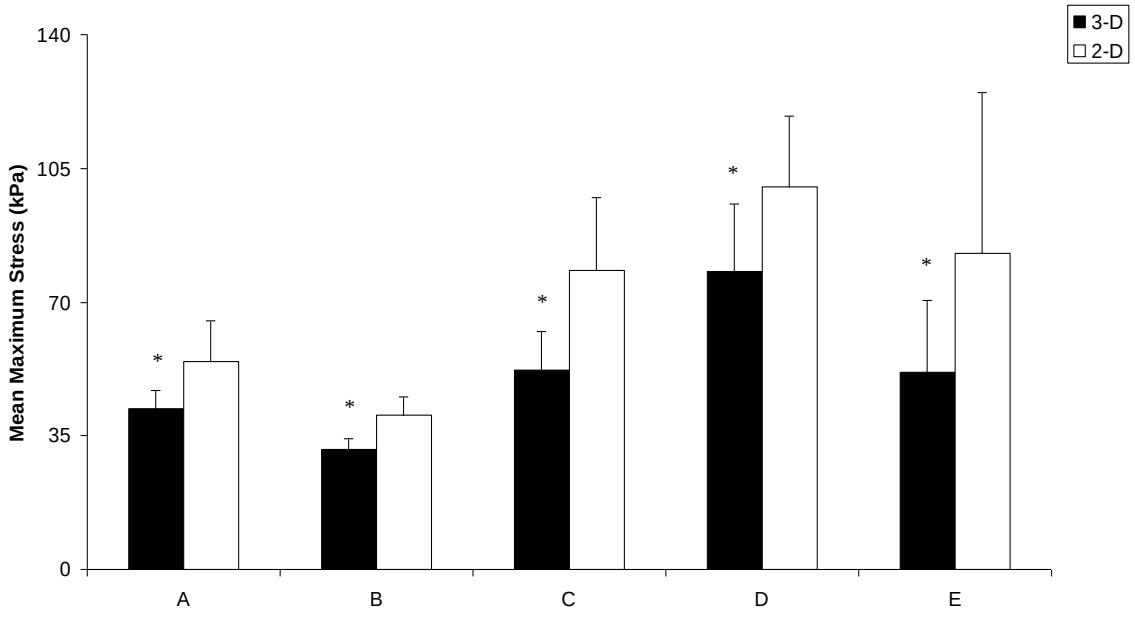

Figure 4.14. Mean maximum stress in 3-D versus plane strain models. * denotes a significance difference at $p < 0.05$.

To further compare 3-D models with plane strain models, the distributions of stresses in five axial locations dispersed approximately uniformly along the length of each specimen were plotted. Figure 4.15 shows the segmentations, as well as the von Mises stress distributions from the 2-D models and the 3-D model at the five axial locations considered for Specimen A. Segmentations and stress distributions are similarly shown for Specimens B, C, D, and E in Figure 4.16, Figure 4.17, Figure 4.18, and Figure 4.19, respectively.

These five figures demonstrate that for each specimen the distributions and magnitudes of stresses predicted in the 3-D models differed from those predicted in the corresponding 2-D models. In Specimens A and B, the maximum von Mises stress was higher at all five axial locations in the 2-D models (Figure 4.15 and Figure 4.16,

respectively), in Specimens C and E, it was higher in four of the five axial locations (Figure 4.17 and Figure 4.19, respectively), and in Specimen D, it was higher in three of the five axial locations (Figure 4.18). For Specimens A, B, C, D, and E, at these five axial locations, plane strain model predictions overestimated stresses by as much as 120%, 67%, 155%, 53%, and 140%, respectively.

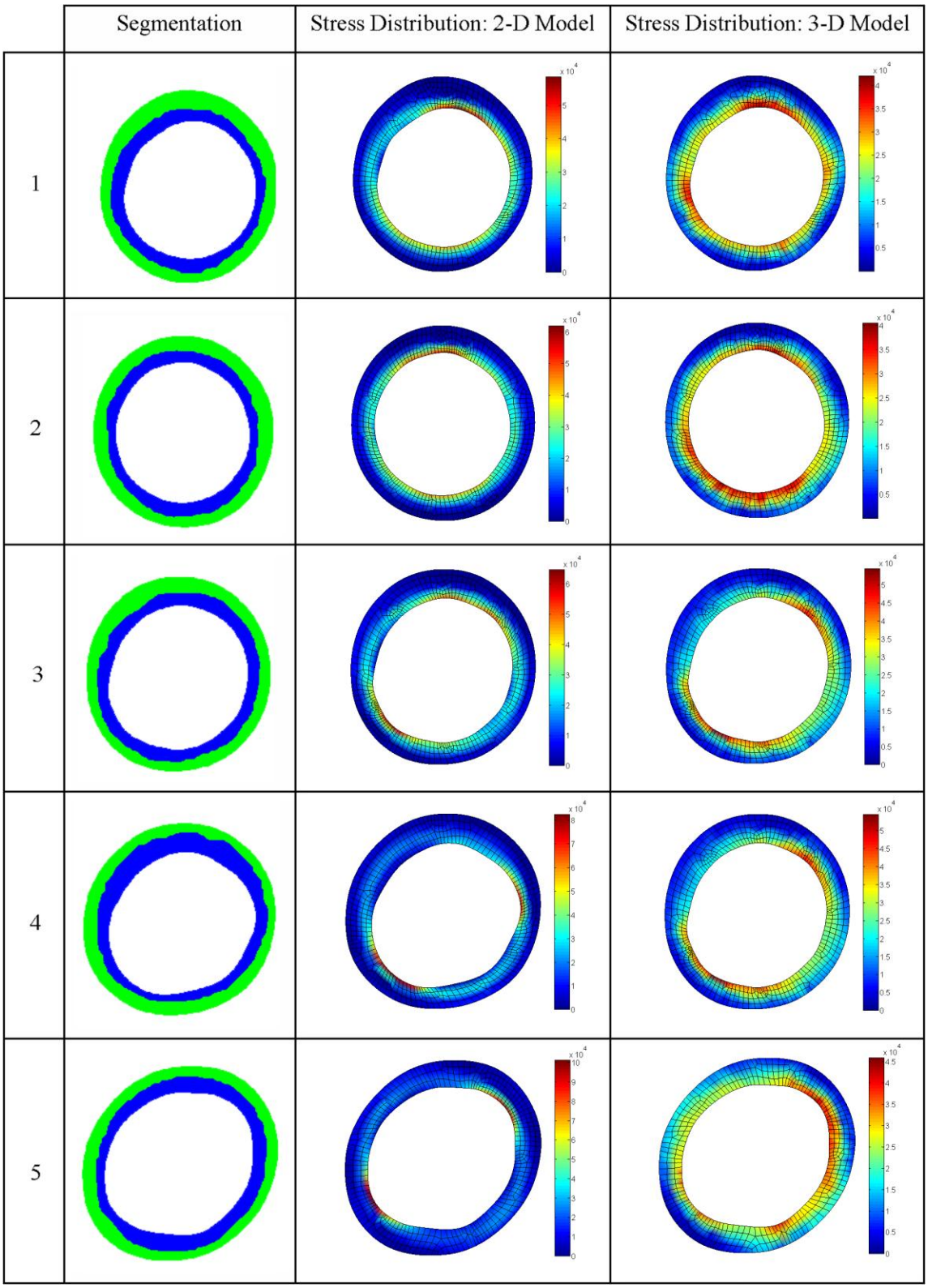

Figure 4.15. von Mises stress distributions in Pa for 2-D models and 3-D model of Specimen A. Also shown are the segmentations at the z-locations considered (green- media; blue- fibrous intima).

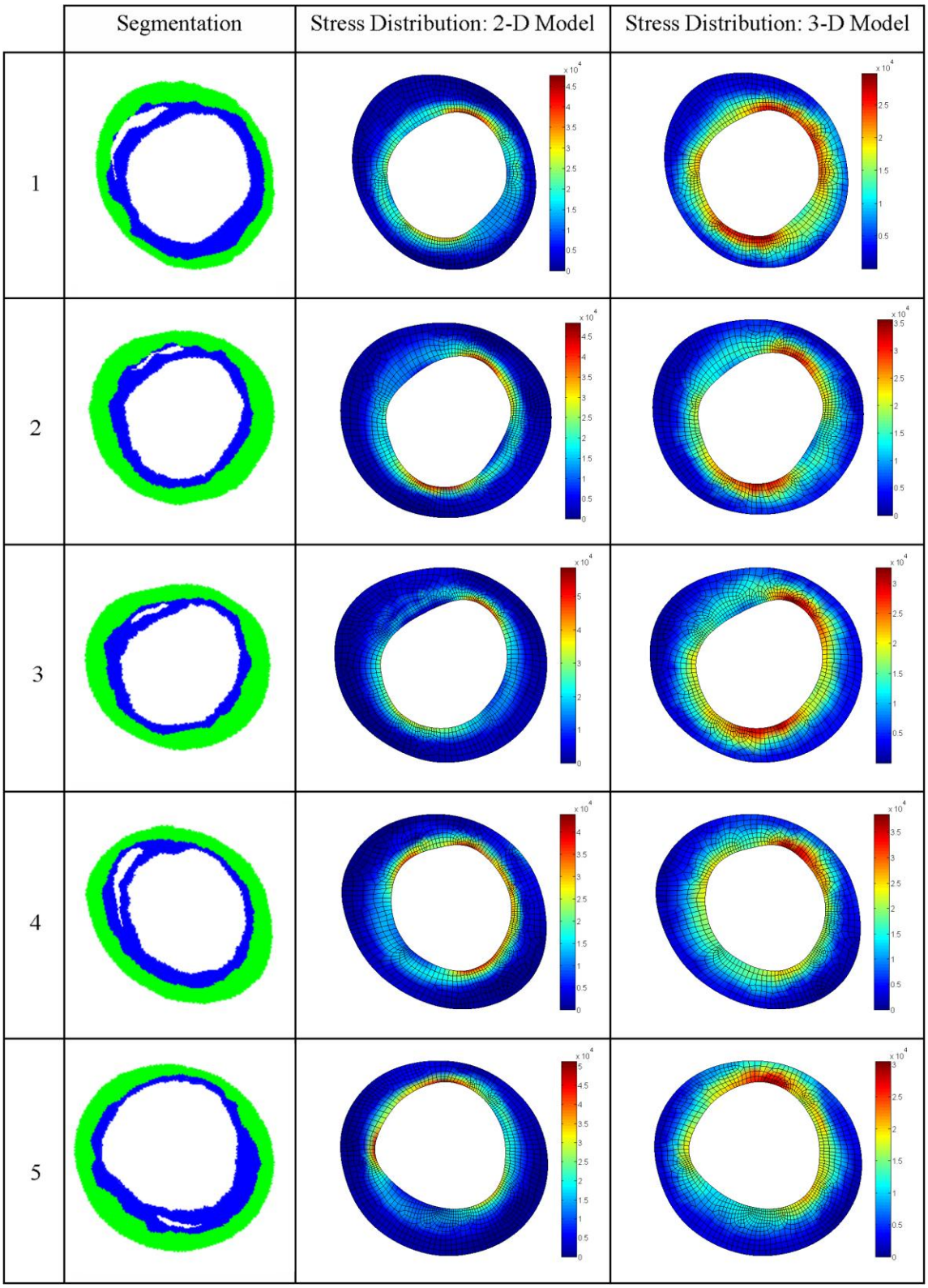

Figure 4.16. von Mises stress distributions in Pa for 2-D models and 3-D model of Specimen B. Also shown are the segmentations at the z-locations considered (green- media; blue- fibrous intima; white- lipid).

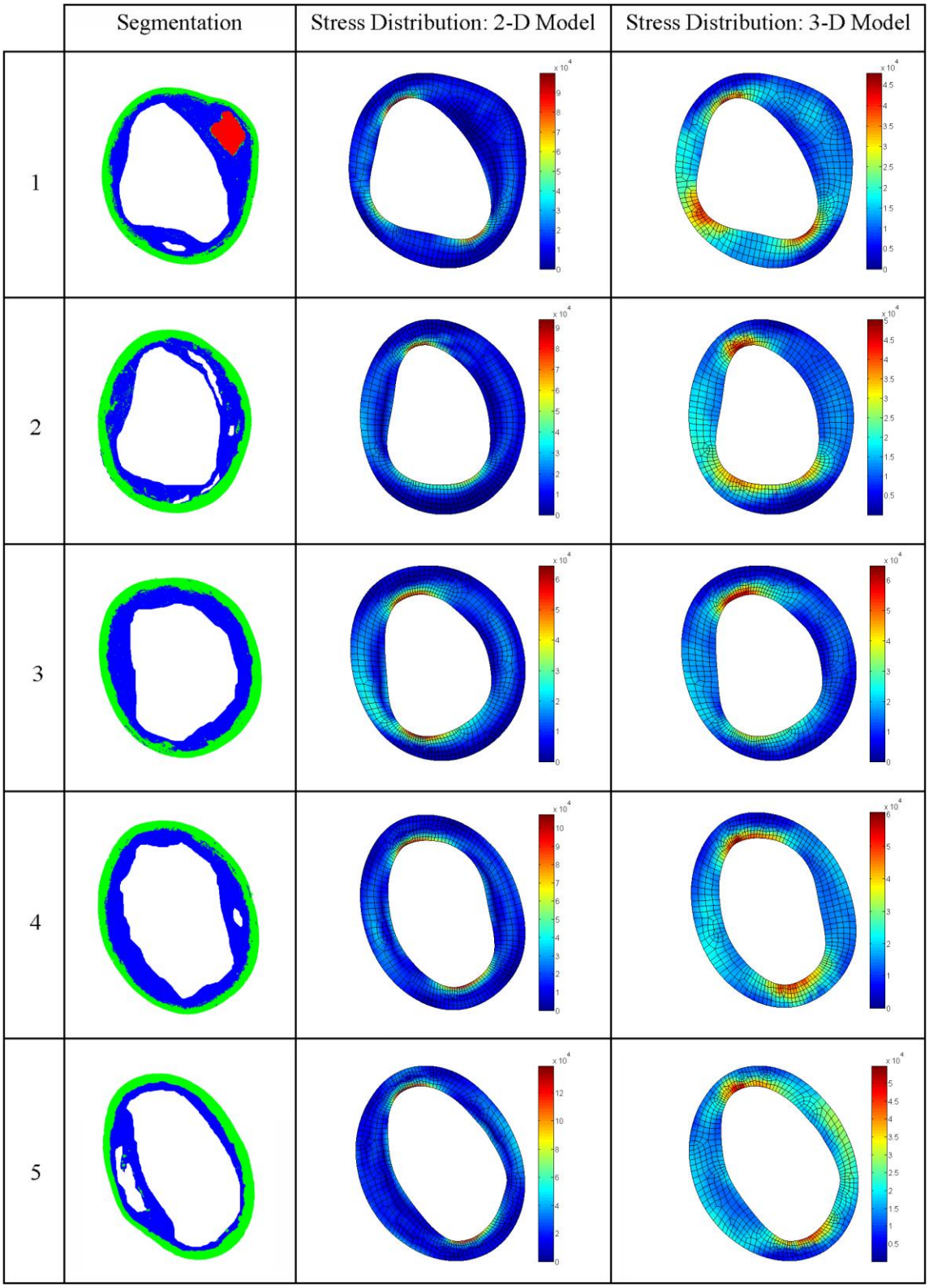

Figure 4.17. von Mises stress distributions in Pa for 2-D models and 3-D model of Specimen C. Also shown are the segmentations at the z-locations considered (green- media; blue- fibrous intima; white- lipid; red- calcification).

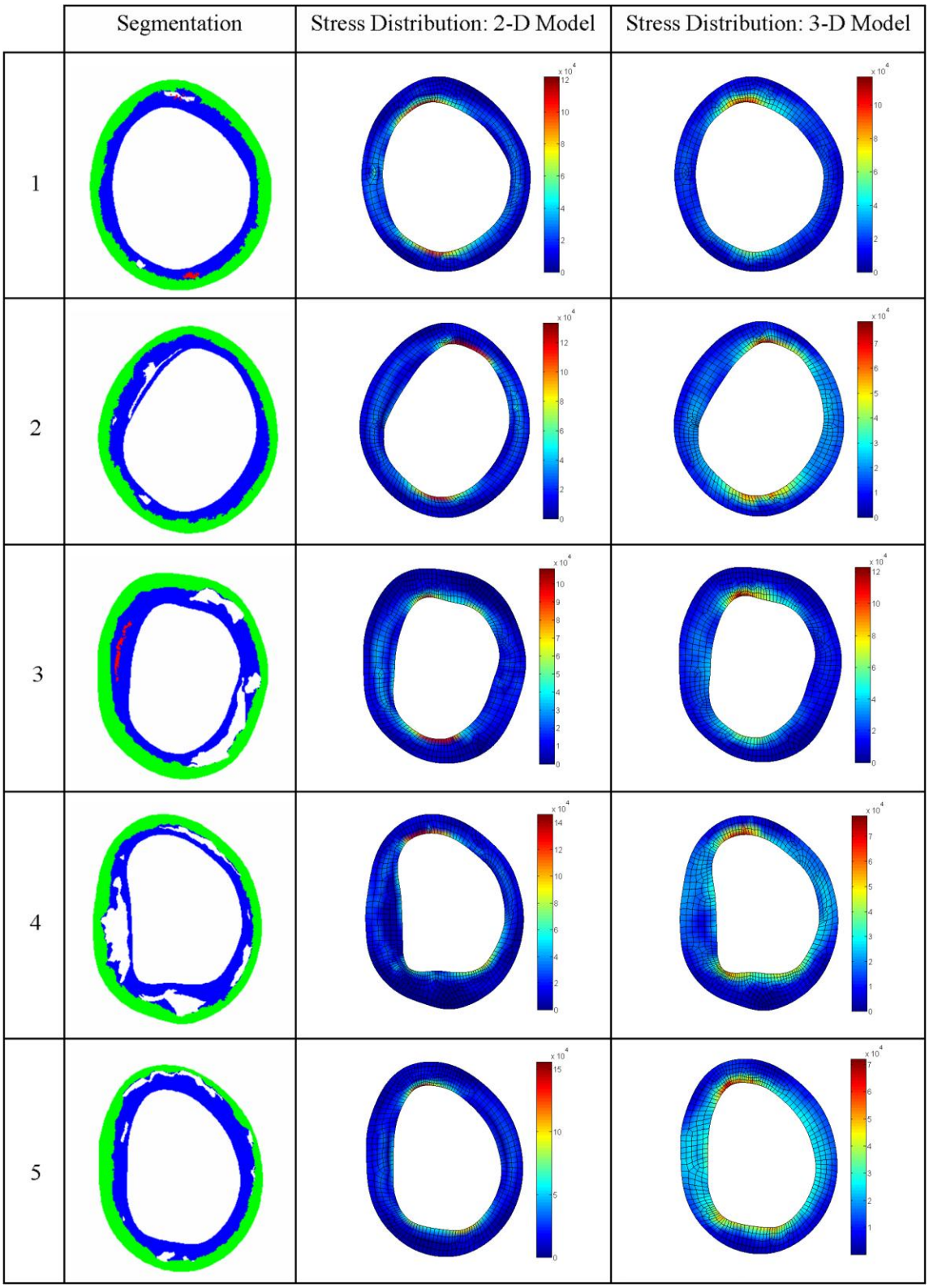

Figure 4.18. von Mises stress distributions in Pa for 2-D models and 3-D model of Specimen D. Also shown are the segmentations at the z-locations considered (green- media; blue- fibrous intima; white- lipid; red- calcification).

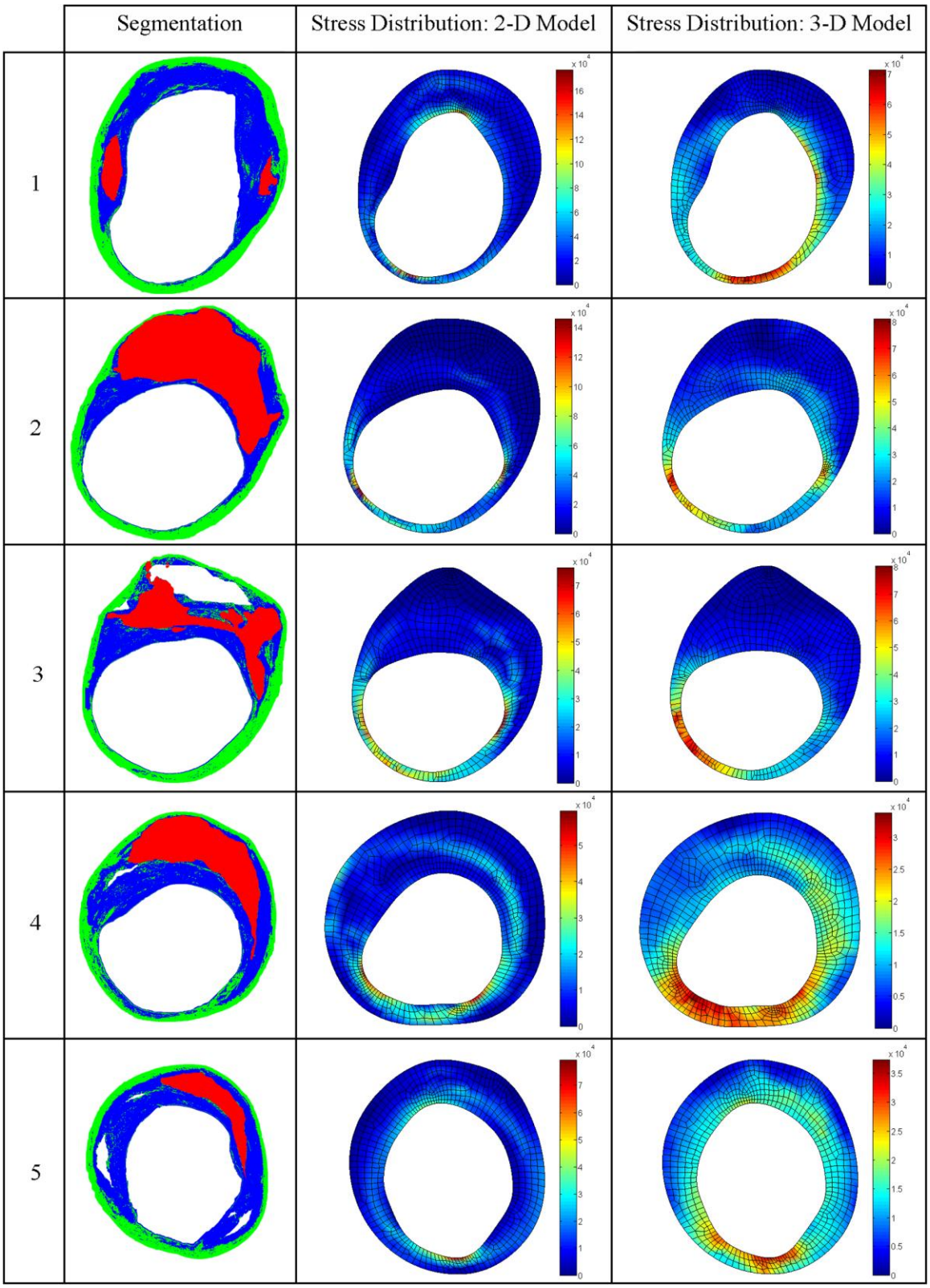

Figure 4.19. von Mises stress distributions in Pa for 2-D models and 3-D model of Specimen E. Also shown are the segmentations at the z-locations considered (green- media; blue- fibrous intima; white- lipid; red- calcification).

Effect of Plaque Features

To facilitate comparison between different 3-D models so that the effects of various plaque features on stress results could be determined, maximum stresses and upper quartile stress averages from the 3-D models did have to be normalized. The plaque features considered were fibrous cap thickness, lipid content, stenosis severity, and calcification content.

For each feature, two types of statistical analyses were performed. First, statistical differences between two groups of normalized stresses, which were divided based on the magnitude of a particular plaque feature measurement, were tested for. These comparisons are depicted in bar graphs. Second, correlative relationships between plaque features and normalized stress levels were tested for. Scatter plots did not provide visual evidence of correlations. Therefore, only Spearman rank correlation coefficients are presented.

Effect of Fibrous Cap Thickness

Figure 4.20 shows a comparison between normalized mean upper quartile stresses at axial locations with thin fibrous caps (< 65 μm, n=16) and at axial locations with thick fibrous caps (>65 μm, n=329). Normalized mean maximum stresses are similarly compared in Figure 4.20. There was no significant difference between normalized mean upper quartile stresses at axial locations with thick fibrous caps (0.87 ± 0.16) and at axial locations with thin fibrous cap (0.92 ± 0.10). Likewise, there was no significant difference between normalized mean maximum stresses at axial locations with thick fibrous caps (0.91 ± .26) and at axial locations with thin fibrous cap (0.97 ± 0.21).

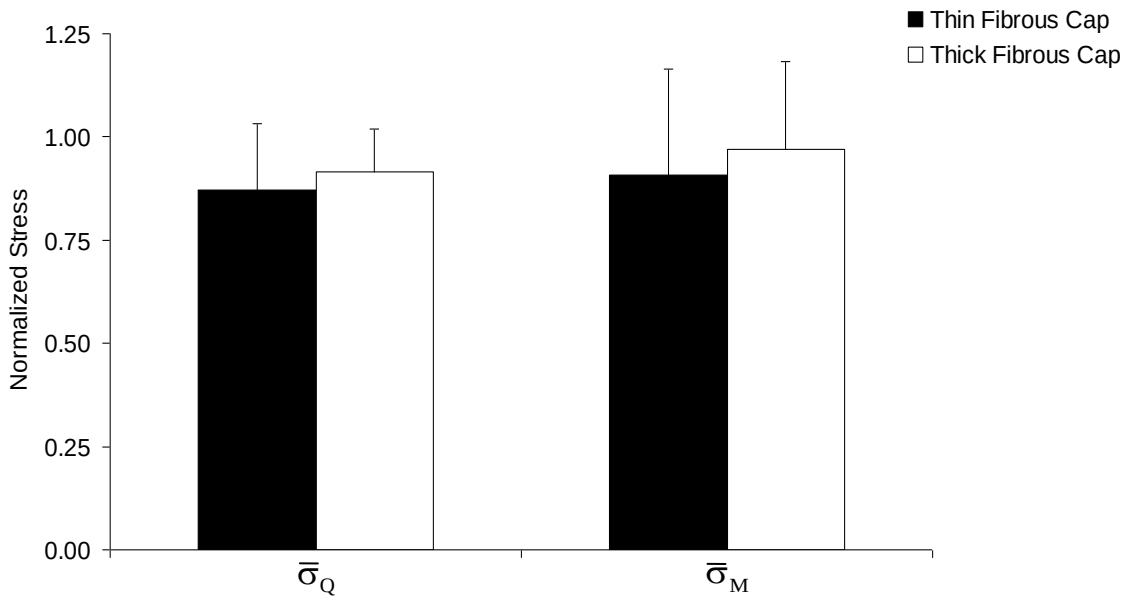

Figure 4.20. Normalized mean stresses at axial locations with thin (< 65 μm) versus thick fibrous caps. $\overline{\sigma}_Q$ represents the normalized mean upper quartile stress and $\overline{\sigma}_M$ represents the normalized mean maximum stress.

The correlations between normalized stresses and fibrous cap thickness are shown in Table 4.8. Both normalized average upper quartile stress and normalized maximum stress showed a significant negative correlation with fibrous cap thickness.

Table 4.8. Spearman rank correlations for normalized stresses versus fibrous cap thickness. σ_Q represents the normalized average upper quartile stress, σ_M represents the normalized maximum stress, and t_{FC} represents the fibrous cap thickness.

Comparison	Correlation Coefficient	p-value
σ_Q vs. t_{FC}	-0.37	<0.001
σ_M vs. t_{FC}	-0.17	0.002

Effect of Lipid Content

Figure 4.21 shows a comparison between normalized mean upper quartile stresses at axial locations with lipid (n=221) and at axial locations without lipid (n=124). Normalized mean maximum stresses are similarly compared in this figure. The normalized mean upper quartile stress was significantly higher ($p < 0.001$) at axial locations in which lipid was present (0.90 ± 0.17) compared to axial locations void of lipid (0.83 ± 0.14). No significant difference between normalized mean maximum stresses was observed at axial locations in which lipid was present (0.93 ± 0.26) and axial locations void of lipid (0.88 ± 0.24).

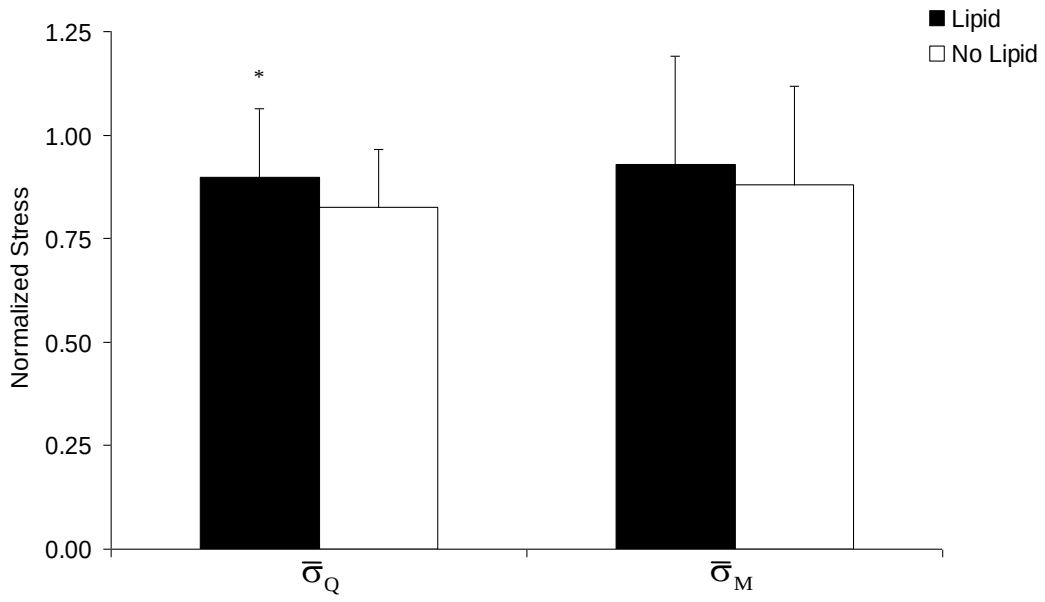

Figure 4.21. Normalized mean stresses at axial locations with lipid versus no lipid. $\bar{\sigma}_Q$ represents the normalized mean upper quartile stress and $\bar{\sigma}_M$ represents the normalized mean maximum stress. * denotes a significance difference at $p < 0.001$.

The correlations between normalized stresses and lipid content are shown in Table 4.9. Normalized average upper quartile stress showed a significant positive correlation with lipid content. However, no correlation between normalized maximum stress and lipid content was observed.

Table 4.9. Spearman rank correlations for normalized stresses versus lipid content. σ_Q represents the normalized average upper quartile stress and σ_M represents the normalized maximum stress.

Comparison	Correlation Coefficient	p-value
σ_Q vs. Lipid Content	0.22	<0.001
σ_M vs. Lipid Content	0.03	0.632

Effect of Stenosis Severity

Figure 4.22 shows a comparison between normalized mean upper quartile stresses at axial locations with high stenosis severity (n=98) and at axial locations with low stenosis severity (n=247). Stenosis severity greater than 40% was considered high and less than 40% was considered low. Normalized mean maximum stresses are similarly compared in Figure 4.22. The normalized mean upper quartile stress was significantly lower ($p < 0.001$) at axial locations with high stenosis severity (0.77 ± 0.17) compared to axial locations with low stenosis severity (0.91 ± 0.14). Likewise, the normalized mean maximum stress was significantly lower ($p < 0.001$) at axial locations with high stenosis severity (0.80 ± 0.30) compared to axial locations with low stenosis severity (0.95 ± 0.22).

The correlations between normalized stresses and stenosis severity are shown in Table 4.10. Both normalized average upper quartile stress and normalized maximum stress showed a significant negative correlation with stenosis severity.

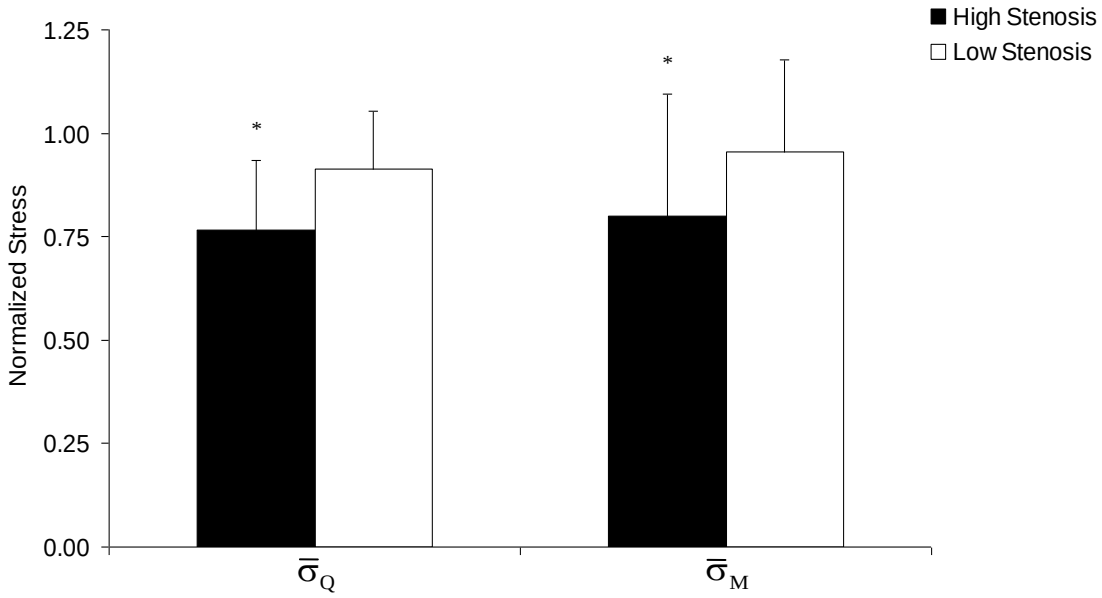

Figure 4.22. Normalized mean stresses at axial locations with high stenosis severity (> 40%) versus low stenosis severity (< 40%). $\overline{\sigma}_Q$ represents the normalized mean upper quartile stress and $\overline{\sigma}_M$ represents the normalized mean maximum stress. * denotes a significance difference at p < 0.001.

Table 4.10. Spearman rank correlations for normalized stresses versus stenosis severity. σ_Q represents the normalized average upper quartile stress and σ_M represents the normalized maximum stress.

Comparison	Correlation Coefficient	p-value
σ_Q vs. Stenosis Severity	-0.18	0.001
σ_M vs. Stenosis Severity	-0.12	0.029

Effect of Calcification

Figure 4.23 shows a comparison between normalized mean upper quartile stresses at axial locations with calcification (n=108) and at axial locations without calcification (n=237). Normalized mean maximum stresses are similarly compared in this figure. The

normalized mean upper quartile stress was significantly lower ($p < 0.001$) at axial locations in which calcification was present (0.80 ± 0.19) compared to axial locations void of calcification (0.90 ± 0.13). Likewise, the normalized mean maximum stress was significantly lower ($p < 0.001$) at axial locations in which calcification was present (0.78 ± 0.26) compared to axial locations void of calcification (0.97 ± 0.23).

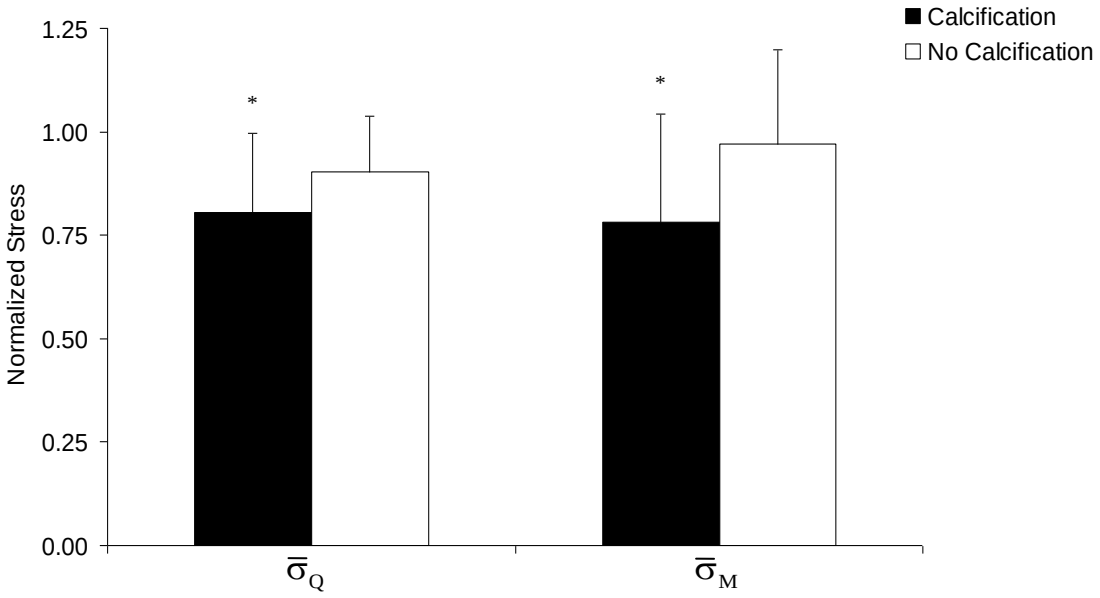

Figure 4.23. Normalized mean stresses at axial locations with calcification versus no calcification. $\bar{\sigma}_Q$ represents the normalized mean upper quartile stress and $\bar{\sigma}_M$ represents the normalized mean maximum stress. * denotes a significance difference at $p < 0.001$.

The correlations between normalized stresses and stenosis severity are shown in Table 4.11. Both normalized average upper quartile stress and normalized maximum stress showed a significant negative correlation with stenosis severity.

Table 4.11. Spearman rank correlations for normalized stresses versus calcification content. σ_Q represents the normalized average upper quartile stress and σ_M represents the normalized maximum stress.

Comparison	Correlation Coefficient	p-value
σ_Q vs. Calcification Content	-0.22	<0.001
σ_M vs. Calcification Content	-0.33	<0.001

Effect of Plaque Features on 3-D versus 2-D Model Stress Predictions

Cases were identified in which trends observed in 2-D models were not observed in 3-D models. Because differences are again within specimens, stress results are not normalized. Figure 4.24 shows the average upper quartile and maximum stress values at corresponding axial locations from the 3-D model and 2-D models for one segment (Segment 1) of Specimen D. Also shown are the fibrous cap thickness values at the same locations. This figure demonstrates an occasion in which the negative correlation between fibrous cap thickness and stress did not hold true for the 3-D model, but did for the corresponding 2-D models. Similar trends were observed for segments (Segments 1) of Specimens C and E (Figure 4.25and Figure 4.26).

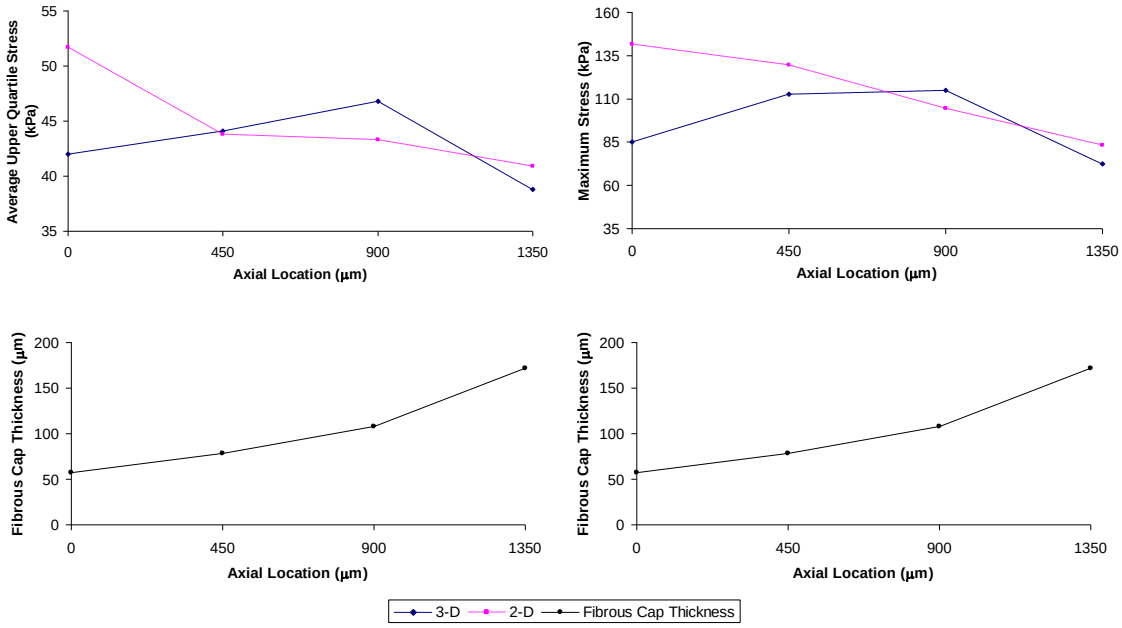

Figure 4.24. Stress values from the 3-D model, stress values from the 2-D models, and fibrous cap thickness at corresponding axial locations in Segment 1 of Specimen D. Axial locations have been shifted such that the first axial location corresponds to zero. Average upper quartile stress values are shown on the upper-left and maximum stress values are shown on the upper-right.

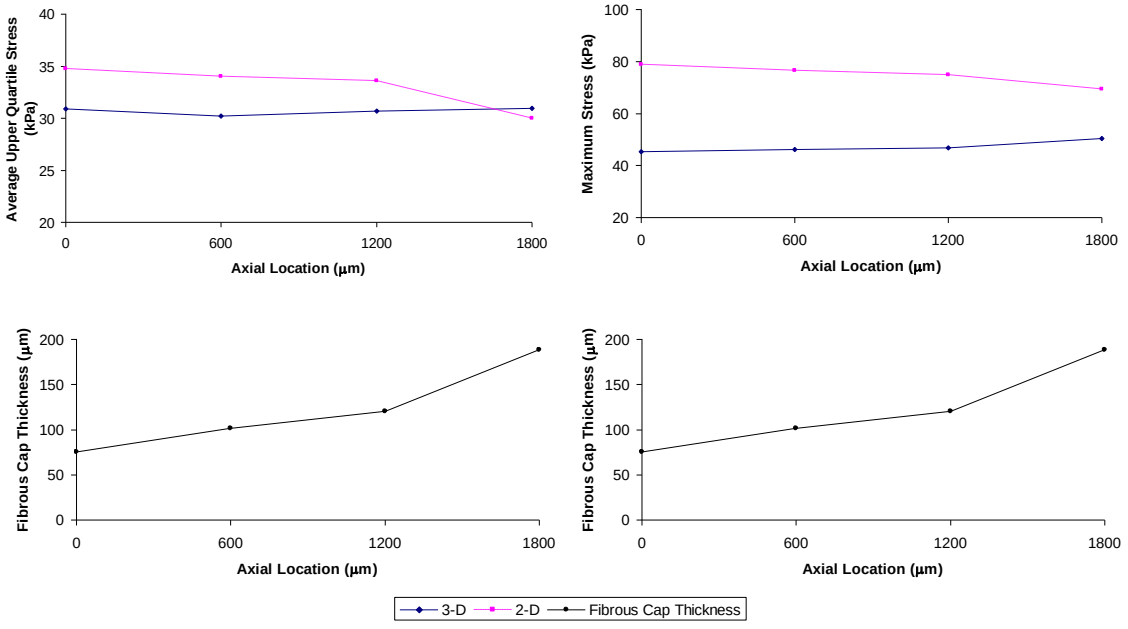

Figure 4.25. Stress values from the 3-D model, stress values from the 2-D models, and fibrous cap thickness at corresponding axial locations in Segment 1 of Specimen C. Axial locations have been shifted such that the first axial location corresponds to zero. Average upper quartile stress values are shown on the upper-left and maximum stress values are shown on the upper-right.

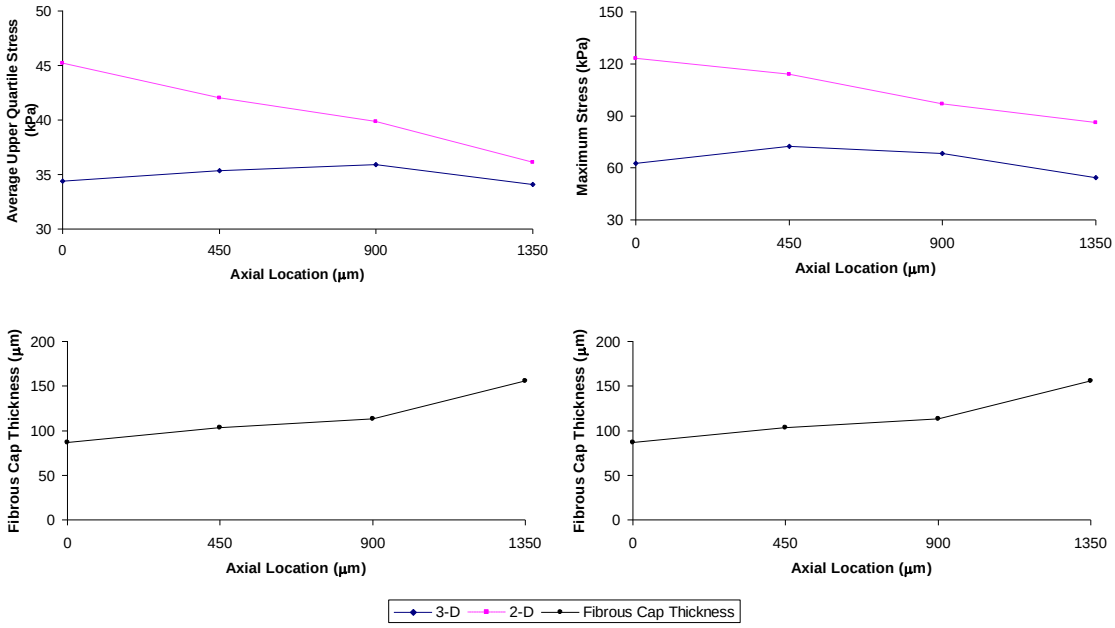

Figure 4.26. Stress values from the 3-D model, stress values from the 2-D models, and fibrous cap thickness at corresponding axial locations in Segment 1 of Specimen E. Axial locations have been shifted such that the first axial location corresponds to zero. Average upper quartile stress values are shown on the upper-left and maximum stress values are shown on the upper-right.

Figure 4.27 shows the average upper quartile and maximum stress values at corresponding axial locations from the 3-D model and 2-D models for another segment (Segment 2) of Specimen D. Also shown are the lipid contents at the same locations. This figure demonstrates that there was again a discrepancy between trends in 2-D models and trends in 3-D models. There was a direct positive correlation of stress with lipid content for the 2-D models, but not for the 3-D model. Similar trends were observed for other segments (Segments 2) of Specimens C and E (Figure 4.28 and Figure 4.29).

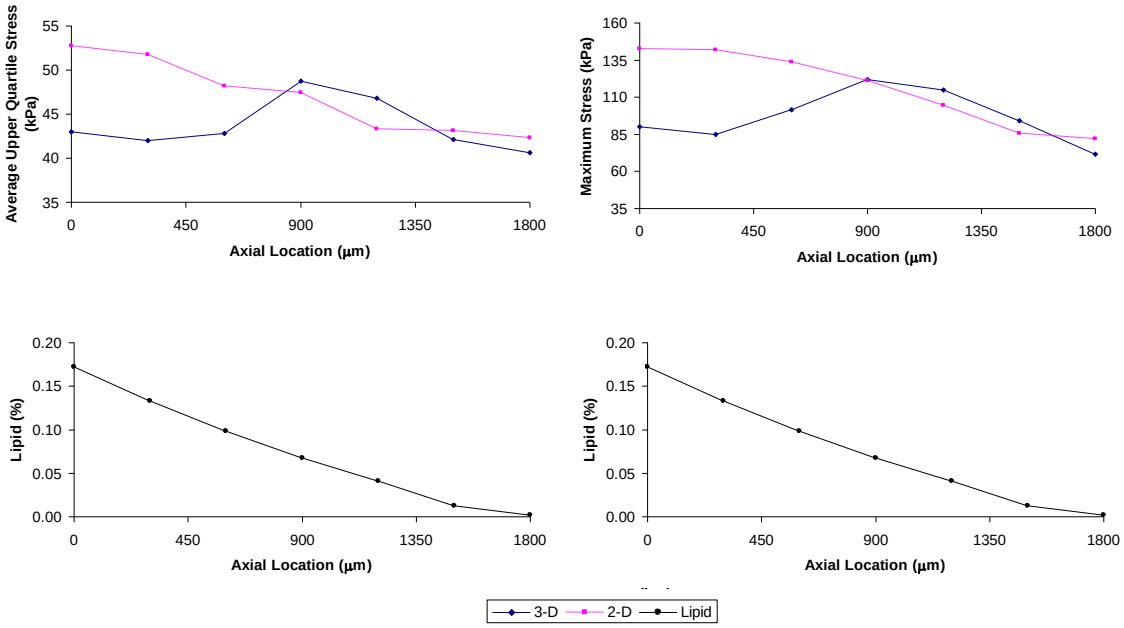

Figure 4.27. Stress values from the 3-D model, stress values from the 2-D models, and lipid content at corresponding axial locations in Segment 2 of Specimen D. Axial locations have been shifted such that the first axial location corresponds to zero. Average upper quartile stress values are shown on the upper-left and maximum stress values are shown on the upper-right.

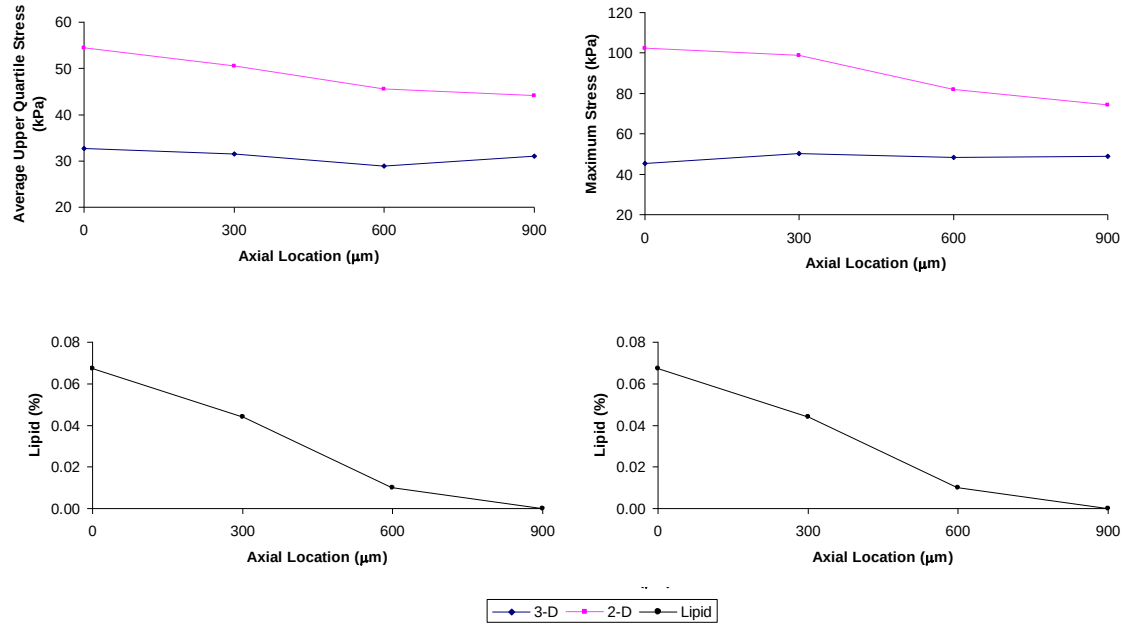

Figure 4.28. Stress values from the 3-D model, stress values from the 2-D models, and lipid content at corresponding axial locations in Segment 2 of Specimen C. Axial locations have been shifted such that the first axial location corresponds to zero. Average upper quartile stress values are shown on the upper-left and maximum stress values are shown on the upper-right.

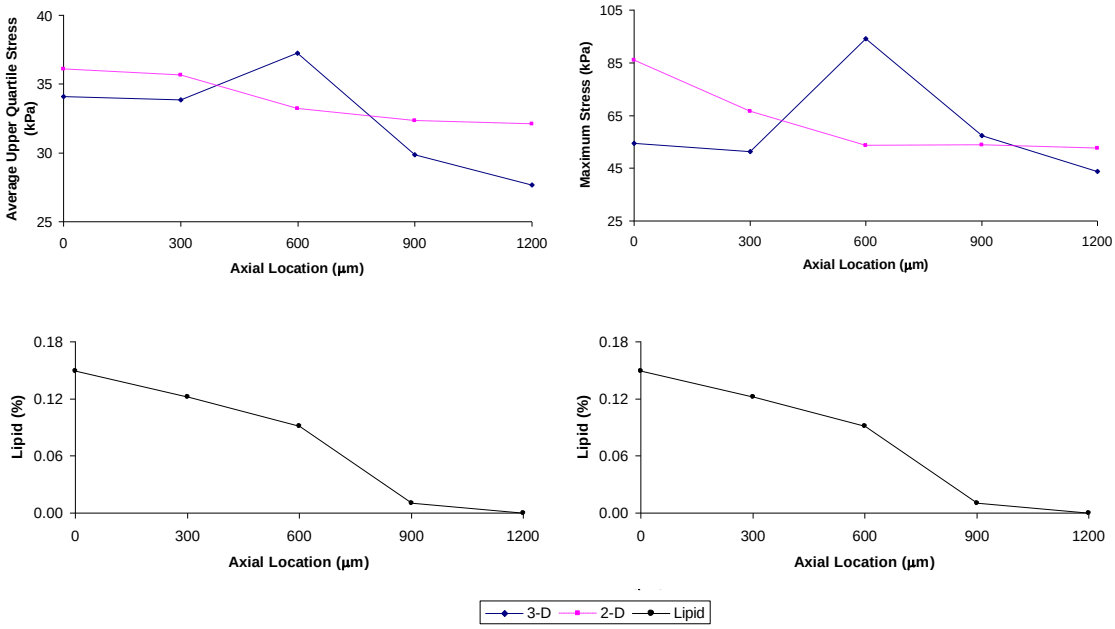

Figure 4.29. Stress values from the 3-D model, stress values from the 2-D models, and lipid content at corresponding axial locations in Segment 2 of Specimen E. Axial locations have been shifted such that the first axial location corresponds to zero. Average upper quartile stress values are shown on the upper-left and maximum stress values are shown on the upper-right.

CHAPTER 5:

DISCUSSION

In this chapter, the results presented in the previous chapter are discussed. Specifically, our novel results are discussed and compared with the previously reported results of others. Also, limitations associated with various aspects of our work are discussed and the clinical relevance of our findings is explained. This chapter is divided into four major sections. As with previous chapters, the first three major sections correspond to each of the specific aims. The final section relates to clinical relevance.

Specific Aim I:

Quantify and correct for histologic distortions to achieve more accurate mechanical models of arteries.

Measuring and Correcting for Histologic Distortions

Given failure to correct for distortions may result in misrepresentation of the actual stress distribution, one goal of our study was to measure and correct for histologic distortions. As mentioned in the Background chapter, a challenge to constructing three-dimensional (3-D) finite element (FE) models based on histologic sections is that the preparation of slides including fixation, dehydration, clearing, infiltration, embedding, sectioning, and staining, induces distortions in the tissue (Deverell, et al., 1989; Jones, et al., 1994). Little attention has been devoted to addressing this issue likely because it is difficult to measure and correct for distortions.

We developed a strain-based method to measure distortions. This method yields a limited set of parameters needed for a first order correction. Thus, corrections can be easily implemented using finite element methods.

A uniform, equibiaxial area dilatation was applied to correct for shrinkage distortions and uniform strains were applied to correct for sectioning distortions. Small errors were associated with these corrections (Table 4.2). The error associated with the shrinkage distortion correction likely arose from the uniformity assumption. It is possible that there is a gradient of shrinkage through the wall, which reflects the varying wall composition. If the adventitia actually shrinks to a greater degree than the media but is assumed to shrink by the same amount, an overestimate in cross-sectional area, as was seen in this study, would result.

Segmentation error was likely the main source of the small error associated with the correction of the sectioning distortion. Five individuals were asked to segment 5 images. These segmentations were then compared to segmentations by the primary investigators. Using Matlab, images segmented by the investigators were subtracted from images segmented by the individuals and the error was taken as the number of pixels in the subtracted image as a percentage of the number of pixels in the investigators' segmented image. The segmentation was overestimated in some cases and underestimated in others. There was an average error of 1.4 ± 0.8 % (n=5) associated with image segmentation. This is comparable to the total error associated with the sectioning distortion correction. In conclusion, we have shown that the developed method is relevant, reliable, and advantageous.

Distortions in Methyl Methacrylate versus Paraffin

Because we chose to work with methyl methacrylate (MMA), a less commonly used embedding media than paraffin, we decided to present a comparison. The findings in our study confirm that distortions occur as a result of histologic preparation and that the extent of distortions is dependent on the processing protocol utilized. We have shown that distortions can be substantially reduced by embedding in an acrylic medium as opposed to paraffin. The largest distortion of the MMA sections is the result of shrinkage. The shrinkage of the paraffin (Bancroft and Gamble, 2002) and MMA sections, as measured here, is comparable so the differences in distortions are the result of different cutting artifacts. Paraffin distorts more than MMA upon cutting because paraffin is much softer than MMA.

In this study, we also quantified the effects of distortions due to histologic preparation on the stress predictions of mechanical models (Tables 4.3 and 4.4). Recall that stress results are presented for a fresh section, a distortion-corrected MMA section, 5 uncorrected MMA sections, and 5 paraffin sections.

The distortion-corrected MMA case result was most similar to the fresh case result. This illustrates the utility of the correction method. However, the uncorrected MMA case also gave a comparable result to the distortion-corrected MMA case and the fresh case. This is expected, given that shrinkage is uniform and sectioning distortions are small.

Geometric distortions caused by sectioning results in a substantial overestimate of the peak stress for the paraffin case relative to the fresh case. In addition, the stress results from the 5 paraffin sections varied significantly while those from the 5

uncorrected MMA sections did not. This demonstrates that paraffin exhibits more section to section variability than does MMA.

Collectively, our results suggest that when developing two-dimensional (2-D) or 3-D mechanical models from histologic cross-sections, MMA should be selected as the embedding medium. Additionally, the results of this study suggest that interpretation of stress results based on paraffin cross-sections (Beattie, et al., 1998; Cheng, et al., 1993; Huang, et al., 2001; Kilpatrick, et al., 2002; Lee, et al., 1996; Tang, et al., 2004) may be misleading.

Limitation of Specific Aim I

A limitation of our approach is that healthy porcine coronary arteries, rather than diseased human coronaries, were used. However, porcine coronary arteries are readily available and have been widely used in the past since they are very similar in structure and function to human coronary arteries. By using healthy arteries, the complexities associated with developing the method were minimized. We acknowledge that histologic preparation is expected to cause non-uniform distortions in diseased arteries. However, by embedding the diseased arteries in MMA as opposed to paraffin the effects of histologic distortions on stress predictions is minimized.

Additional Applications

The methods developed to quantify and correct for distortions due to histologic preparation can be extended. Previous work has shown that the extent of histologic distortions is dependent on tissue type (Deverell, et al., 1989; Jones, et al., 1994). While distortions are measured and corrected for in arteries in our study, the novel methods developed can be extended to other tissue types. Furthermore, the radio-opaque

embedding media developed and utilized here could potentially serve as a contrast agent in other imaging studies.

Specific Aim II:

Develop three-dimensional mechanical models of human coronary atherosclerotic plaques based on minimally distorted histologic sections.

Modeling Approach

We have successfully developed a methodology to generate 3-D FE models of a human coronary atherosclerotic plaque based on acrylic histologic sections. First, the models developed using our approach are superior to models based on traditional imaging modalities because higher resolution histologic techniques are better able to identify lesion constituents and biological markers of disease. The in-plane resolution of the images in our study is at five to 15 times better than the in-plane resolution of the images in all other 3-D studies that have been discussed. To the best of our knowledge, ours is the only approach that allows for the detection of vulnerable plaques.

An additional advantage of the methodology used in this study relates to the developed segmentation techniques. In all other 3-D studies, medical images were segmented by manually tracing the borders of each arterial constituent. We used a semi-automatic segmentation approach that is not only less time-consuming and less subjective, but also results in the generation of a more realistic segmentation in which heterogeneous mixing of constituents is accounted for.

Another benefit of our modeling approach involves the use of non-uniform rational b-spline (NURBS) surfaces. Like some others (Holzapfel, et al., 2005; Holzapfel,

et al., 2002), we generated 3-D FE models using these surfaces. The use of NURBS surfaces is preferable to other reconstruction techniques because smooth surfaces, which are present in arterial structures, are provided. In addition, NURBS surfaces are easily handled by FE analysis software and are well-suited for FE mesh generation.

When modeling, assumptions are typically made in order to make the mathematical problem that has been formulated solvable. The implementation of different modeling assumptions in this study may have led to different stress results. However, an assumption's impact on stress predictions from 3-D models is expected to be similar to its impact on predictions from 2-D models. Thus, even if different assumptions had been made, comparisons of 2-D and 3-D model results would have led to the same conclusions.

Limitations of Specific Aim II

To the best of our knowledge, histology is the only technique capable of identifying vulnerable plaques. However, histology is a destructive technique. Because the tissue is sectioned, cross-sectional images must be aligned before a 3-D model can be generated. Although we have developed an approach that allows the curvature of an artery to be maintained, some small error may be introduced due to slight misalignment of sections. Future research should be devoted to the development of non-destructive imaging techniques that are capable of identifying vulnerable plaques.

An important issue in studying plaque rupture involves the selection of a reliable failure criterion. In our study, extreme values of von Mises stress were selected as the criterion. However, some have suggested that rupture is the result of fatigue of the plaque's fibrous cap (Bank et al., 2000; Versluis et al., 2006), but this has not been

proven. In fact, fatigue is only one of several theories that have been proposed. Further studies are needed to determine which failure criteria are appropriate. Once identified, these criteria should be evaluated in the context of the models developed in this study.

We used the available mechanical properties of human aortic atherosclerotic plaque in our modeling of diseased human coronary atherosclerotic plaque. To the best of our knowledge, there is no work, which using a physiologic loading approach reports the mechanical properties of human coronary atherosclerotic plaque. This may be in part due to the difficulty associated with isolating coronary arteries for in vitro testing (Humphrey, 2002). Isolation requires extensive dissection including the ligation of many perforating branches.

Further, in our study, the plaque consisted of lipid, media, fibrous intima, and calcification. Partitioning into four uniform components is obviously a simplification. In such a case, spatial or interspecimen variations within a particular constituent, which may affect stress predictions, are neglected. Still, we, like others (Beattie, et al., 1998; Cheng, et al., 1993; Kilpatrick, et al., 2001; Kilpatrick, et al., 2002; Lee, et al., 1996; Loree, et al., 1992; Ohayon, et al., 2005), used this approach simply because more accurate anisotropic mechanical property data are not available. There is a pressing need to quantify the anisotropic mechanical properties of diseased human coronary arteries.

One disadvantage of pressure fixing an ex vivo sample is that wall stresses cannot be calculated from the zero stress state. Justification for neglecting the effects of stresses existing in the pressure-fixed configuration was provided in the Materials and Methods chapter. The approach is suitable when relative stress distributions are of interest, as was the case in the present study. However, the approach is unacceptable in cases in which

actual stress distributions are required. The effect of pressure-fixing at another pressure, as opposed to 80 mmHg, should be studied. Pressure-fixing at a pressure closer to 0 mmHg would lead to more accurate stress results, but may also lead to unacceptable histologic artifacts caused by postmortem collapse and contraction.

In our study, residual stresses due to differences in the strains of the constituents, which may affect stress results, were neglected because they have not been quantified. The method used to characterize healthy arteries' residual stress-states (Fung, 1993) is not extendable to diseased arteries given most of the plaque constituents are not ring-shaped and longitudinal variations cannot be neglected. Similarly, axial in situ stretch ratios, which cannot be measured independently for each constituent, were neglected. Techniques to quantify residual stresses and axial in situ stretch ratios in diseased arteries should be developed.

Specific Aim III:

Determine whether correlations between stress results from 3-D mechanical models and plaque features exist and whether these stress results are consistent with results from 2-D mechanical models.

Distribution of Stress

In the present study, in Specimens B (Figures 4.9 and 4.16), C (Figures 4.10 and 4.17), and D (Figures 4.11 and 4.18), stress concentrations typically occurred in the shoulder regions of the plaques. These concentrations reflect the large differences in stiffness between the fibrous cap and underlying lipid pool and are in agreement with autopsy data that have indicated that plaque rupture typically occurs in the shoulder

regions of a plaque. In Specimen A (Figures 4.8 and 4.15), which had no fibrous cap, stresses were more uniformly distributed due to the circumferential uniformity of this artery. In Specimen E (Figures 4.12 and 4.19), stresses were concentrated in the thinnest portion of the arterial wall. Due to the complex geometry and mechanical property distributions associated with this particular model, it is not possible to provide a qualitative explanation for the stress distribution that occurred.

Effect of Longitudinal Variation

In the present study, we have shown that 2-D models, in which longitudinal variation in plaque geometry and mechanical properties is neglected, lead to different stress predictions than do 3-D models (Figures 4.15 – 4.19). As has been discussed, the distribution of stress has been studied extensively in 2-D models of atherosclerotic plaques, but not in 3-D models. The abundance of 2-D studies, as opposed to 3-D, is attributed to the associated simplification of geometrical complexity and reduction in computational time. Two-dimensional models are based on the assumption of plane strain, which is valid only when there are no longitudinal variations in geometry and mechanical properties. Our study has shown (segmentations in Figures 4.15 – 4.19) that this assumption is not always valid.

Recall that in the 2-D study by Cheng and colleagues (1993), plaque ruptures occurred very close to a region of high stress, but did not always coincide with the rupture site. In one 3-D study (Ohayon, et al., 2005), rupture location and peak stress did coincide. Our finding that 2-D and 3-D models lead to different stress results provides further evidence suggesting that had the plain strain assumption not been utilized, peak stress and rupture site may have coincided in the Cheng study.

Consistent with previous studies (Ohayon, et al., 2005; Tang, et al., 2004), in our study, 2-D analyses overestimated the magnitude of stress in all five arteries when compared to corresponding 3-D analyses (Figures 4.13 and 4.14) . The previous studies evaluated maximum principal stresses, while our interest focused on von Mises stresses. However, correlation analyses revealed significant positive correlations between von Mises stresses and maximum principal stresses from 3-D models of Specimens A, B, C, D, and E (correlation coefficients equal 0.92, 0.74, 0.78, 0.77, and 0.71, respectively) and from 2-D models of the same specimens (correlation coefficients equal 0.97, 0.98, 0.83, 0.85, and 0.83, respectively). Thus, it is expected that 2-D analyses would have overestimated the magnitude of maximum principal stresses.

With this in mind, our study provides a plausible explanation to an existing discrepancy between in vivo testing and 2-D finite element analysis results. In vivo testing has shown that human atherosclerotic plaques fracture under stresses in excess of 300 kPa (Lendon, et al., 1991). However, 2-D FE analyses suggest that much higher maximum principal stresses (545 ± 160 kPa) are associated with ruptured plaques (Cheng, et al., 1993).

Another important finding in our study was that the plane strain assumption can lead to erroneous conclusions, which connect plaque features to plaque stresses (Figures 4.24 – 4.29). Collectively, our results show that failure to account for longitudinal variations in geometry and mechanical properties may lead to inaccurate stress predictions and thereby to incorrect stress-based plaque stability assessments.

Effects of Fibrous Cap Thickness and Lipid Content

The present study, like previous studies, investigated the influence of fibrous cap thickness on biomechanical plaque stresses. Consistent with prior studies (Finet et al., 2004; Loree, et al., 1992), we found that decreases in fibrous cap thickness lead to increases in cap stresses (Table 4.8). Recall that fibrous cap thickness is a morphological characteristic specifically associated with plaque rupture. The fibrous cap, composed predominately of collagen, is the major load-bearing constituent of an atherosclerotic plaque. Thus, our result is rational given decreases in fibrous cap thickness equate to decreases in the load-bearing abilities of the arterial wall.

We found that axial locations in which the cap thickness was less than 65 μm did not have significantly higher stresses than axial locations in which the cap thickness was greater than 65 μm (Figure 4.20). This result differs from the result of one 2-D study that found that stresses consistently exceeded stability ranges in plaques with fibrous cap thicknesses below 65 μm (Finet, et al., 2004).

In the present study, quartile stresses were significantly higher at axial locations in which lipid was present compared to axial locations void of lipid, but maximum stresses showed no statistical difference (Figure 4.21). Furthermore, while increases in normalized upper quartile stress averages correlated with increases in lipid content, normalized maximum stresses showed no correlation (Table 4.9). Recall that our motivation for investigating the effects of lipid content is based on the observation that lipid-rich lesions are more likely to rupture and cause myocardial infarctions than lipid-poor lesions. Our results, which were taken from 3-D rather than 2-D models, contradict the results of previous 2-D parametric studies (Kilpatrick, et al., 2001; Loree, et al., 1992)

and of a 2-D study based on histologic sections (Huang, et al., 2001), which found that the more lipid a plaque contains, the higher the maximum stress.

In summary, we have shown that stresses may be relatively low in a plaque that, based on a morphological description alone, would be termed vulnerable. Recall that vulnerable plaques are defined as plaques with large lipid pools and thin fibrous caps. The terminology was formulated based autopsy data that have shown that the majority of ruptured plaques possess these features. However, as we have pointed out, morphological studies also indicate that detection of a vulnerable plaque is not in itself enough to predict rupture; meaning not all plaques with a large lipid pool and thin, fibrous cap rupture. Accepting the finding that the tendency of a plaque to rupture is due to the mechanical stresses in the fibrous cap, our study offers a plausible explanation for this.

It is likely that previous mechanical analyses were unable to arrive at this result due to the implementation of the plane strain assumption. Figures 4.24 – 4.26 show that in the 3-D models developed in this study there were occasions in which the negative correlation between fibrous cap thickness and stress did not hold true. Such was not the case in the corresponding 2-D models. Figures 4.27 -4.29 show that there were instances in which there was a direct positive correlation of stress with lipid content for the 2-D cases, but not for the 3-D cases. Our results suggest that the 3-D stress field within a vulnerable plaque must be known in order to assess plaque stability.

Effect of Stenosis Severity

In this study, as in a previous parametric study (Loree, et al., 1992), the effect of stenosis severity on plaque stresses was examined. Results were consistent and showed that increases in stenosis severity correlate with decreases in stresses (Table 4.10). Given an increase in stenosis severity can be likened to a decrease in radius to thickness ratio, this result is logical. In general, stresses are expected to be lower in an artery that has a smaller radius to thickness ratio compared to an artery that has a larger radius to thickness ratio.

In our study, axial locations in which the stenosis severity was less than 40% had significantly higher stresses than axial locations in which the stenosis severity was greater than 40% (Figure 4.22). Recall that positive remodeling occurs once stenosis severity exceeds 40%. Although positive remodeling is advantageous in terms of preventing luminal stenosis, it is also thought of as harmful. Our results provide an explanation for previous morphological studies findings, in which most lesions responsible for myocardial infarction were positively remodeled, but were minimally occlusive (< 50% stenosis) (Giroud, et al., 1992; Little, et al., 1988).

Effect of Calcification Content

As was done in a previous study (Huang, et al., 2001), our study examined the influence of calcification on biomechanical stresses. Results were in agreement and showed that decreases in calcification content correlate with increases in plaque stresses (Table 4.11). Our study further showed that stresses were significantly lower at axial locations in which calcification was present compared to axial locations void of calcification (Figure 4.23).

Of all of the plaque constituents, calcification is the stiffest. The results presented here suggest that calcification may impart stability on an atherosclerotic plaque, which is reasonable since stiffer materials will undergo smaller deformations, which will produce smaller stresses. Although calcification is indicative of the presence of disease, calcification content is not associated with plaque instability. Our result provides an explanation for findings from a previous morphological study, in which ruptured plaques had relatively low amounts of calcification (Burke, et al., 2001).

Limitation of Specific Aim III

Because of the intraspecimen and interspecimen variations in the sample population in this study, we were not able to quantify the effect that the abruptness of change in plaque constituents, in the longitudinal direction, has on stress results. Obviously, a plaque that gradually changes morphology over a long distance will have a different impact on stress than a plaque that changes rapidly over a short distance. Parametric studies that examine the effects of such scenarios may be warranted. However, such studies will not negate our finding that failure to account for longitudinal variations in plaque geometry and mechanical properties can lead to inaccurate stress predictions and thereby to incorrect stress-based plaque stability assessments.

Clinical Relevance

The purpose of this research was to analyze the three-dimensional distribution of stress in human coronary atherosclerotic plaques. We acknowledge that this was primarily a basic science study. At this stage, there is not a clinical application focus that

is immediately relevant to cardiologists. However, we expect that our results will serve as a basis for future clinical applications.

We have shown that morphological description of a plaque is not sufficient to predict plaque rupture; the 3-D stress field within a plaque must be known in order to assess plaque vulnerability. The mechanical stresses in the fibrous cap arise from a combination of the mechanical properties of the plaque as well as the distribution of lesion constituents. As has been shown here, extensive intraspecimen and interspecimen variations exist in atherosclerotic plaques. This means it would not be possible to use the results from a series of developed models to predict stresses based on morphological visual inspection. Thus, unique, patient specific models must be developed if the 3-D stress field within a plaque is to be determined. Provided imagining techniques, in the future, are able to yield high resolution, in vivo images with sufficient details, the novel methods presented in our study could be used to develop patient specific FE models that identify plaques which are prone to rupture. Once identified, appropriate medical interventions can be prescribed to preemptively treat these vulnerable plaques prior to a clinical event.

CHAPTER 6:

CONCLUSIONS AND FUTURE WORKS

Conclusions

Cardiovascular disease is the leading cause of death in the United States. In 2007, direct (health expenditures) and indirect (lost productivity due to morbidity or mortality) costs associated with this disease are expected to exceed $400 billion. Coronary heart disease (CHD) accounts for the majority of deaths from cardiovascular diseases (Rosamond, et al., 2007). Most acute myocardial infarctions, a form of CHD, are caused by coronary artery atherosclerotic plaque rupture with subsequent thrombus formation. Given its devastating impact, significant research pertaining to plaque rupture is warranted.

Plaque rupture is a mechanical event. As discussed in previous chapters, until now, a critical need has existed to determine the distribution of stress in morphologically correct, three-dimensional mechanical models of human coronary atherosclerotic plaques. Results from such models can be used to determine whether correlations between plaque features and stresses exist.

Several significant conclusions arose from this research project. Our results confirm that morphological description of a vulnerable plaque is not sufficient to predict plaque rupture. Our findings suggest that in many cases the three-dimensional (3-D) stress field within a vulnerable plaque must be known in order to assess plaque stability. Moreover, the results of this study show that patient specific models must be developed if the 3-D stress field within a plaque is to be determined.

To the best of our knowledge, histology is the only technique capable of identifying vulnerable plaques. However, the preparation of histologic slides induces distortion. In this research, a method to measure and correct for distortions caused by acrylic processing was first developed. It was then applied it to intact, healthy porcine coronary arteries. The devised strain-based method yields a limited set of parameters needed for a first order correction. Thus, corrections can be easily implemented using finite element methods.

Because methyl methacrylate (MMA), a less commonly used embedding media than paraffin, was used in this study, the effects of preparation related distortions on stresses in acrylic versus paraffin histologic-based models were compared. Distortions and the effects of distortions on stresses were substantially reduced by embedding in an acrylic medium as opposed to paraffin. Our results suggest that when developing two-dimensional (2-D) or 3-D mechanical models from histologic cross-sections, MMA should be selected as the embedding medium. Otherwise, interpretation of stress results from models based on paraffin cross-sections may be misleading and lead to incorrect plaque stability assessments.

Building on these findings, a methodology to create 3-D finite element (FE) models of human coronary atherosclerotic plaques was next developed. This methodology accounts for longitudinal variations in geometry and mechanical properties and uses stable acrylic histologic sections as a basis for model construction. Five models of plaques ranging in disease severity using the developed methodology were generated.

Finally, the distributions of stress in these models were obtained and the effects of plaque features on stresses were determined. To determine the effects of longitudinal

variations, stress predictions from 3-D FE models were compared to predictions from corresponding 2-D models. Stress predictions from 3-D mechanical models were significantly different compared to stress predictions from 2-D models. This result provides a plausible explanation as to why plaque rupture and peak stress do not always coincide in 2-D FE models. Further, it helps explain why stresses associated with ruptured plaques are higher than expected in these same 2-D models. Our results suggest that neglecting longitudinal variations in geometry and mechanical properties may lead to inaccurate stress predictions and thereby to incorrect stress-based plaque stability assessments.

In addition to the effects of longitudinal variations, the effects of fibrous cap thickness and lipid content on stresses were examined. Decreases in fibrous cap thickness led to increases in stresses, but axial locations with thin fibrous caps did not have significantly higher stresses than axial locations with thick fibrous caps. Upper quartile stresses were significantly higher at axial locations in which lipid was present compared to axial locations void of lipid. Additionally, increases in upper quartile stresses correlated with increases in lipid content. However, maximum stresses showed no statistical difference and no correlation. Our results provide a plausible explanation for the finding that morphological description of a vulnerable plaque is not in itself enough to predict rupture. Analyses of 3-D versus 2-D model predictions showed that previous 2-D mechanical analyses were likely unable to provide this explanation due to the implementation of the plane strain assumption.

The effects of stenosis severity and calcification content on stresses were also examined. Increases in stenosis severity and calcification content correlated with

decreases in stresses. Further, stresses were lower at axial locations in which stenosis severity was greater than 40% compared to axial locations in which stenosis severity was less than 40%. Finally, stresses were lower at axial locations in which calcification was present compared to axial locations void of calcification. These results help explain prior morphological studies which found that the majority of ruptured plaques are minimally stenosed and have relatively low amounts of calcification.

Future Works

The overwhelming clinical relevance of plaque rupture motivated this research and will continue to serve as a motivation for future investigations. Based on the limitations and findings of our work, there are several recommendations for future studies.

In the present study, some modeling assumptions were made in order to reduce modeling and computational complexities. Other assumptions were necessitated by lack of data. In the future, revision of some of our modeling assumptions may be appropriate.

Related to the modeling of geometry, healthy porcine coronary arteries were used to create an approach to quantify and correct for histologic distortions. By using healthy arteries, the complexities associated with developing the method were minimized. However, histologic preparation is expected to cause non-uniform distortions in diseased arteries. Methods to quantify and correct for histologic distortions in such arteries should be developed.

In this study, the mechanical properties of constituents from diseased human aorta were used. Further, residual stresses due to differences in the strains of the constituents were neglected. Mechanical properties of coronary artery plaque constituents and the residual stress-states of these constituents are unknown. If these data become available,

they should be integrated into the mechanical modeling aspect of our approach. Their effects on stress predictions should then be determined.

The arteries utilized in this study were pressure fixed at 80 mmHg. In future studies, the effect of pressure-fixing at a lower pressure on histologic artifacts should be investigated. Pressure-fixing at a pressure closer to 0 mmHg would lead to more accurate stress results. If it is found that arteries can be fixed at a lower pressure, only our modeling of loading conditions will need to be changed.

Additional work is needed to determine which plaque rupture failure criteria are appropriate. Although maximum von Mises stresses were used as the criteria in our study, studies may emerge revealing this is not best. If that is the case, our modeling technique should be appropriately revised. For example, if fatigue is found to cause rupture, the pulsitility of blood pressure should be incorporated into our modeling of loading conditions.

In this work, the effect that the manner of change in plaque constituents, in the longitudinal direction, has on stress results was not determined. In the future, parametric studies using the FE models generated in this study should be conducted to elucidate such effects.

Increases in stenosis severity were shown in our study to be associated with reductions in stresses. Similarly, increases in calcification content were associated with reductions in stresses. Extensive lumen narrowing occurs in some, but not all diseased arteries. Analogously, some plaques calcify while others do not. The precise reasons for this are unknown. Research identifying the causes for these occurrences could potentially help us to better assess the stability of plaques and is therefore warranted.

In this study, we did not correlate biological markers of disease with stress predictions from our 3-D mechanical models. However, because our models are based on histologic sections, this is possible. Subsequent studies should correlate biological markers of disease with stress predictions.

APPENDIX A:

HISTOLOGY PROTOCOLS

Specific Aim I:

Quantify and correct for histologic distortions to achieve more accurate mechanical models of arteries.

Mounting, Processing, and Embedding of Porcine Tissue

(This protocol is a modified version of an original obtained from Tracey Couse.)

Purpose: Radio-opaque methyl methacrylate embedding of soft tissue for CT scanning and histology purposes.

References: Edited by Bancroft, J.D., Gamble, M. *Theory & Practice of Histological Techniques*, Fifth Edition. Churchill Livingstone, 2002.

Fixation: 10% neutral buffered formalin, 10% formal calcium, or 10% formal-saline.

Tissue Size: 10 x 5 x 2 mm

Hazards: **Reagents used in this procedure are carcinogenic, neurotoxic, and explosive. User should wear gloves, goggles, and perform all work under a fume hood. Care must be taken to limit the addition of the catalyst and activator. Do not place solutions with catalyst and activator at temperatures greater that 37°C.**

- Mount the sample as shown below:

1) Secure luers to each end of the artery with suture. Using a stereomicroscope, measure the length of the artery.
2) Insert fishing line into a hole in the top luer and through the corresponding hole in the bottom luer. Thread the line through the bottom luer in the hole 180º from the first bottom hole. Pull the line through the corresponding hole in the top luer.
3) Repeat Step 2 for remaining holes with another piece of fishing line.
4) Place the sample, including luers and lines, into the mounting tube.
5) Hold the bottom of the sample in place in the mounting tube by inserting a pin through the tube into the bottom luer. Using the stereomicroscope, adjust the top luer so that the length of the artery is as it was out of the tube.
6) Secure the top luer with a pin. Insert the ends of the fishing line into the slits at the top of the mounting tube.
7) Store the mounted sample in a tube containing PBS until scanning.

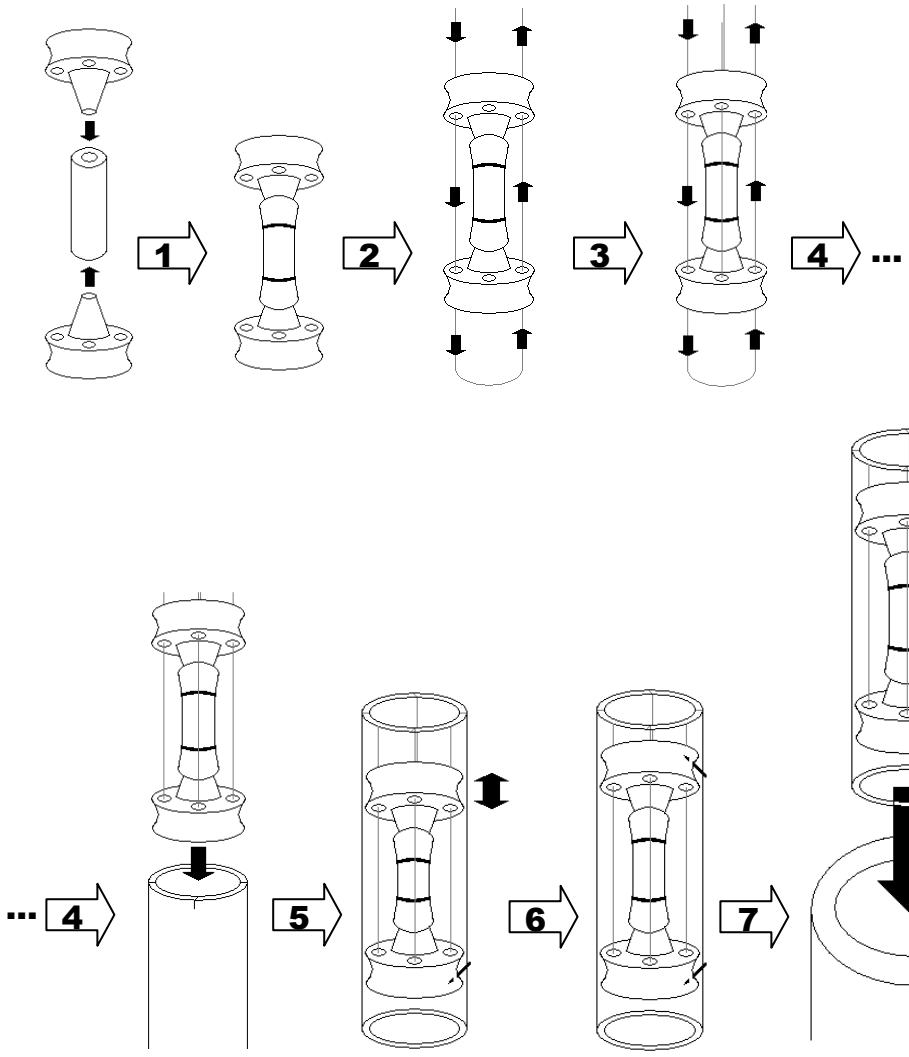

- Following scanning remove mounted sample from tube containing the scanning solution. Rinse with PBS until any remaining scanning solution has been washed away.
- Remove the pin holding the top luer in place. This will allow the tissue to shrink.
- Place mounted sample in 10% neutral buffered formalin. (Fixative volume should be approximately twenty times that of tissue volume.) Fix for approximately 48 hours. (Fixation rate is approximately 1mm per 24 hours.)
- Once fixed, dehydrate and clear tissue on Shandon Pathcentre. Tissue will be dehydrated and then cleared under pressure and vacuum via the following schedule: 80% alcohol for 1 hour, 95% alcohol for 45 minutes, 95% alcohol for 1 hour, 100% alcohol for 45 minutes, 100% alcohol for 1 hour x 2, xylene substitute for 45 minutes x 2. Prepare infiltration solution a minimum of 30 minutes prior to completion of dehydration.
- Remove sample from processor and place into 10mL of MMA infiltration solution:

Infiltration Solution	30mL
MMA (monomer)	22.5mL
Dibutyl phthalate (softener)	7.5mL
Benzoyl peroxide (catalyst)	1.5g

Mix solution for at least 30 minutes before adding sample.

- Infiltrate in two 10mL changes of infiltration solution each for 1 hour. Infiltrate in a further change of infiltration solution overnight. The infiltration steps are performed on a rotator at room temperature.
- To complete, infiltrate for 45 minutes under vacuum at 10 inches of mercury.
- Prepare the embedding solution:

Embedding Solution	15 mL
MMA (monomer)	11.25 mL
Dibutyl phthalate (softener)	3.75 mL
Benzoyl peroxide (starter)	0.75 g
Barium Sulfate	3 g
N,N-dimethyl-p-toluidine (activator)	188 μL

- Combine the first 4 ingredients of the embedding solution, vortex, and place on shaker for a minimum of 30 minutes.
- Add activator and mix by hand for 1 minute.
- Remove the mounted sample from the tube containing the infiltration solution. Pour a portion of the embedding solution into a tube. Place the mounted sample in this tube and add embedding solution until the tube is full.
- Invert by hand for 30 minutes alternating between 3 minutes on ice and 3 minutes off of ice.
- Place the tube under vacuum to free any bubbles that may be trapped and then allow sample to polymerize. Polymerization should occur in 4-6 hours.
- Cut the sample from the tubes.
- Pull lines out of polymerized block. (The remaining voids will act as registration marks.)
- Ensure ends are flat using the grinder. Superglue block to a base.

Notes:

a. Reagents used in this procedure are carcinogenic, neurotoxic, and explosive.
b. Care must be taken to limit the addition of the catalyst and activator.
c. Do not place solutions with catalyst and activator at temperatures greater that 37°C.
d. Heat causes rapid polymerization. Boiling may result and therefore bubbles will become trapped in the polymerized block.
e. Avoid contamination of MMA solutions with water, as they are incompatible.
f. For optimal processing use agitation.
g. Polymerization is enhanced under anaerobic conditions.

Reagents:
10% Neutral buffered formalin: Fisher #SF100-20
Methyl methacrylate: Fisher # AC127140025
Dibutyl phthalate: Aldrich #15,243-9
Benzoyl peroxide: Sigma #17,998-1
Barium Sulfate: Sigma #B3758
N,N-dimethyl-p-toluidine (aka N-N, dimethylaniline): Aldrich #D18900-6

Hematoxylin and Eosin Staining

(This protocol is a modified version of an original obtained from Tracey Couse.)

Purpose:	A basic morphology stain.
Reference:	Edited by Bancroft, J.D., Gamble, M. *Theory & Practice of Histological Techniques*, Fifth Edition. Churchill Livingstone, 2002.
Microtomy:	2-5 um sections using a tungsten carbide blade. The slides require drying horizontally on a hot plate for a minimum of 30 minutes at 60ºC.
Fixation:	10% neutral buffered formalin.
QC:	Any native tissue.
Hazards:	Alcohol and xylene. These reagents are flammable and toxic. Use under a fume hood with gloves and goggles. All dyes are potential carcinogens and toxic. Wear gloves and goggles.

Method:
This is performed on the Leica Autostainer as program 12. The details are as follows:

1/ Deplasticize sections in xylene twice for 20 minutes and in acetone for 5 minutes.
2/ Continue deplasticization and rehydration to distilled water using the following schedule:
- Xylene x 3 for 3 minutes each.
- 100% alcohol x 3 for 2 minutes each.
- 95% alcohol x 2 for 2 minutes each.
- 75% alcohol x 1 for 2 minutes.

3/ Rinse in distilled water for 2 minutes.
4/ Stain in hematoxylin for 30 minute.
5/ Rinse in tap water until excess dye is removed, about 2 minutes.
6/ Differentiate in 0.5% acid alcohol (0.5% HCl in 70% alcohol) for 1 dip (1 second).
7/ Quickly transfer to water and rinse for 1 minute.
8/ Blue slides in Scott's tap water for 30 seconds.
9/ Rinse in water for 15 minute.
10/ Stain in 1% aqueous eosin in 1% calcium chloride for 30 seconds.
11/ Rinse in water for 20 seconds.
12/ Rinse in 95% alcohol for 20 seconds.
13/ Dehydrate in 100% alcohol x 2 for 20 seconds each.
14/ Clear in xylene x 3 for 1 minute each.
15/ Coverslip and mount in permanent mounting medium.

Results:
Nuclei blue-purple
Erythrocytes and eosinophilic granules bright pink to red
Cytoplasm and other tissue elements various shades of pink

Notes:
Avoid drying of sections.

Reagents:
Gill's III Modified Hematoxylin: Harleco #65067
Eosin Y, Fisher #E-511
CaCl, EMS#12340

1% Calcium Chloride:
CaCl 5g
Deionized water 500ml
Stir to dissolve.

1% Aqueos Eosin:
Eosin 5g
1% CaCl 500ml
Stir to dissolve. Filter with Whatman #1.

0.5% Acid Alcohol:
70% alcohol 995ml
HCl, conc. 5ml
Add the acid to the 70% alcohol.

Scott's Tap Water:
NaHCO3 (Sodium bicarbonate) 2g
MgSO4 (Magnesium sulfate) 20g
dH2O 1000ml
Mix until dissolved. Autoclaving is not necessary.

Specific Aim II:

Develop three-dimensional mechanical models of human coronary atherosclerotic plaques based on minimally distorted histologic sections.

Processing and Embedding of Human Tissue

(This protocol is a modified version of an original obtained from Tracey Couse.)

Purpose:	Methacrylate embedding of soft tissue for histology purposes.
References:	Edited by Bancroft, J.D., Gamble, M. *Theory & Practice of Histological Techniques*, Fifth Edition. Churchill Livingstone, 2002.
Fixation:	10% neutral buffered formalin, 10% formal calcium, or 10% formal-saline.
Tissue Size:	10 x 5 x 2 mm
Hazards:	**Reagents used in this procedure are carcinogenic, neurotoxic, and explosive. User should wear gloves, goggles, and perform all work under a fume hood. Care must be taken to limit the addition of the catalyst and activator. Do not place solutions with catalyst and activator at temperatures greater that 37°C.**

- Pressure fix the sample in room temperature 10% neutral buffered formalin for 2 hours. (Fixative volume should be approximately twenty times that of tissue volume.) Fix for approximately 36 hours after pressure has been removed. (Fixation rate is approximately 1mm per 24 hours.)
- Once fixed, dehydrate and clear tissue on Shandon Pathcentre. Tissue will be dehydrated under pressure and vacuum via the following schedule: 80% alcohol for 1 hour, 95% alcohol for 1 hour x 2, 95% alcohol for 1.25 hours, 100% alcohol for 1 hour x 2, 100% alcohol for 1.25 hours, xylene substitute for 1 hour x 2, xylene substitute for 1.25 hours. Prepare infiltration solution a minimum of 30 minutes prior to completion of dehydration.
- Remove sample from processor and place into 10mL of MMA infiltration solution:

Infiltration Solution	30mL
MMA (monomer)	22.5mL
Dibutyl phthalate (softener)	7.5mL
Benzoyl peroxide (catalyst)	1.5g

Mix solution for at least 30 minutes before adding sample.

- Infiltrate in two 10mL changes of infiltration solution each for 1 hour. Infiltrate in a further change of infiltration solution overnight. The infiltration steps are performed on a rotator at room temperature.
- Prepare the embedding solution:

Embedding Solution	15 mL
MMA (monomer)	11.25 mL
Dibutyl phthalate (softener)	3.75 mL
Benzoyl peroxide (starter)	0.75 g
N,N-dimethyl-p-toluidine (activator)	94 μL

- Combine the first 3 ingredients of the embedding solution, vortex, and place on shaker for a minimum of 30 minutes.
- Add activator and combine (by hand for 1 minute).
- Pour solution into a tube and position artery.
- Cut the sample from the tube.
- If sample is longer than 10 mm, cut block into segments using the Isomet. Mark proximal end.
- Ensure ends are flat using the grinder. Superglue block(s) to base(s).

Notes:

a. Reagents used in this protocol are carcinogenic, neurotoxic, and explosive.
b. Care must be taken to limit the addition of the catalyst and activator.
c. Do not place solutions with catalyst and activator at temperatures greater that 37°C.
d. Heat causes rapid polymerization. Boiling may result and therefore bubbles will become trapped in the polymerized block.
e. Avoid contamination of MMA solutions with water, as they are incompatible.
f. For optimal processing use agitation.
g. Polymerization is enhanced under anaerobic conditions.

Reagents:

10% Neutral buffered formalin: Fisher #SF100-20
Methyl methacrylate: Fisher # AC127140025
Dibutyl phthalate: Aldrich #15,243-9
Benzoyl peroxide: Sigma #17,998-1
Barium Sulfate: Sigma #B3758
N,N-dimethyl-p-toluidine (aka N-N, dimethylaniline): Aldrich #D18900-6

Masson's Trichrome Staining

(This protocol is a modified version of an original obtained from Tracey Couse.)

Purpose: Collagen stain differentiating it from smooth muscle cells.
References: Mallory, Sheehan & Hrapchak
Carson, FL: *Histotechnology: A Self-Instructional Text*.
American Society of Clinical Pathologists, 1990.
Microtomy: 2-5 um sections.
Fixation: Bouin's solution is preferred. 10% neutral buffered formalin may be used.
QC: Small intestine, uterus, appendix.
Hazards: Dried picric acid is explosive. Keep container tightly sealed. Wet lid before opening. Discard as chemical waste by calling OEHS.

Method:

1/ Deplasticize sections in xylene twice for 20 minutes and in acetone for 5 minutes.
2/ Continue deplasticization and rehydration to distilled water using the following schedule:
Xylene x 3 for 3 minutes each.
100% alcohol x 3 for 2 minutes each.
95% alcohol x 2 for 2 minutes each.
75% alcohol x 1 for 2 minutes.
3/ Rinse well in distilled water.
4/ Mordant sections in Bouin's for 1 hour at 56°C.
5/ Remove slides from oven and allow cooling at room temperature. Wash in running tap water until yellow is no longer visible.
6/ Rinse in distilled water.
7/ Stain in Weigert's hematoxylin for 2 minutes.
8/ Wash in running tap water for 10 minutes.
9/ Rinse in distilled water.
10/ Stain sections in Biebrich's scarlet-acid fuchsin for 4 minutes. Solution can be used twice before discarding.
11/ Rinse in distilled water.
12/ Place sections in phosphomolybdic-phosphotungstic acid for 10 minutes. Discard after use. This step removes red from collagen.
13/ Stain sections in aniline blue for 5-10 minutes. Solution may be used twice before discarding.
14/ Rinse the slides in 1% acetic acid solution for 3-5 minutes. Discard solution after use.
15/ Dehydrate in 95% and 100% alcohol, twice each.
16/ Clear with 2-3 changes of xylene and mount with synthetic resin.

Results:
Nuclei black
Cytoplasm, muscle fibers, keratin red
Collagen and mucus blue

Notes:
Collagen may be counterstained with light green in place of aniline blue.
The following changes are made:
Step 11. Place sections in 5% aqueous phosphotungtic acid solution.
Step 12. Stain 5 minutes in 2% light green.
Light green is a preferred counter stain when collagen is predominant. Use aniline blue when small amounts are to be demonstrated.

Reagents & Solutions:

Bouin's Solution:
Picric acid, saturated aqueous solution 75ml
Formaldehyde, 37% to 40% 25ml
Glacial acetic acid 5ml

Weigert's Iron Hematoxylin:
Solution A Hematoxylin (C.I. 75290) 10g
Alcohol, 95% 1000ml
Solution B Ferric chloride, 29% aqueous solution 20ml
Distilled water 475ml
Glacial acetic acid 5ml
Working solution: Mix equal parts of A to B.

Biebrich Scarlet-Acid Fuchsin Solution:
Biebrich scarlet (C.I. 26905), 1% aqueous solution 360ml
Acid fuchsin (C.I. 42685), 1% aqueous solution 40ml
Glacial acetic acid 4ml

Phosphomolybdic-Phosphotungstic Acid Solution:
Phosphomolybdic acid 25g
Phosphotungstic acid 25g
Distilled water 1200ml

Aniline Blue Solution:
Aniline blue 25g
Glacial acetic acid 20ml
Distilled water 1000ml

1% Acetic Acid Solution:
Glacial acetic acid 1ml
Distilled water 99ml

2% Light Green (read notes for use)
Light green SF yellowish (C.I. 42095) 2.0g
Distilled water 98ml
Glacial acetic acid 1.0ml

Von Kossa Staining

(This protocol is a modified version of an original obtained from Tracey Couse.)

Purpose: Detection of calcium phosphate.
References: Carson, FL: Histotechnology: A Self-Instructional Text.
American Society of Clinical Pathologists, 1990.
Microtomy: 4-5 um sections.
Fixation: Alcohols preferred. 10% neutral buffered formalin acceptable.
QC: Section containing calcium.
Hazards: Silver nitrate is dangerous. Wear goggles & gloves. Dispose of to chemical waste.

Method:
1/ Deplasticize sections in xylene twice for 20 minutes and in acetone for 5 minutes.
2/ Continue deplasticization and rehydration to distilled water using the following schedule:
Xylene x 3 for 3 minutes each.
100% alcohol x 3 for 2 minutes each.
95% alcohol x 2 for 2 minutes each.
75% alcohol x 1 for 2 minutes.
3/ Place sections in silver nitrate solution and expose to bright sunlight or a UV light source for 10 to 20 minutes. Check slides periodically and stop reaction when the calcium salts are brown to black.
4/ Rinse in distilled water.
5/ Place slides in 5% sodium thiosulfate for 2-3 minutes.
6/ Wash well in distilled water.
7/ Counter stain for 5 minutes in nuclear-fast red.
8/ Wash sections well in water.
9/ Dehydrate through 95% and 100% alcohol, twice each.
10/ Clear with 2-3 changes of xylene and mount with synthetic resin.

Results:
Calcium salts_____black.
Background_____red.

Notes:
The silver reacts with the anions, mainly carbonate and phosphate of the calcium salts. Bright light reduces the silver salts to metallic silver. Unreduced silver is removed via sodium thiosulfate.
The use of unbuffered formalin may cause false positive results. Formic acid can lead to the generation of formalin pigment, which will reduce silver and result in a brown reaction product.

Reagents & Solutions:

5% Silver Nitrate

Silver nitrate	5g
Distilled water	100ml

5% Sodium Thiosulfate

5% Sodium thiosulfate	5g
Distilled water	100ml

Nuclear-fast Red (Kernechtrot) Solution

Nuclear-fast red	0.5g
Aluminum sulfate	25g
Distilled water	500ml

Dissolve the aluminum sulfate in the distilled water. Proceed to dissolve the nuclear-fast red in this solution, using heat. Cool, filter, and add a few grains of thymol for preservation.

APPENDIX B:

MATLAB CODE

Specific Aim I:

Quantify and correct for histologic distortions to achieve more accurate mechanical models of arteries.

Shrinkage Distortion Calculation

shrinkagedistortion.m

```
% This program calculates the shrinkage distortion.

clear all
close all

% Read in fresh and embedded images by inputting file names of each.

I=imread([<input>]);
I2=imread([<input>]);

% Calculate area of fresh section.
h=REGIONPROPS(I, 'all');
areaf = [h.Area];

% Calculate area of embedded section.
h2=REGIONPROPS(I2, 'all');
areae = [h2.Area];

% Record result.
A=(areaf-areae)/areaf;
```

Registration Mark Identification

pickreghole.m

```
% This program is used to identify registration marks in embedded and
%  sectioned and stained state images.

clear all
close all

% Read in image by inputting file name.
I = imread(<input>);

R = 8;

% Zoom in on image by pressing the left mouse button and zoom out by
%  pressing right mouse button.  Press enter to exit zooming.
imshow(I)
set(gcf,'Pointer','circle')
hold on
theta = 0:10:360;
x = [];
y = [];
i = 1;

% Select four registration marks by pressing the left mouse button.
%  Selection is marked with a green circle and a red star.
%  Move a selected point using the right mouse button.  Cancel by
%  clicking the middle mouse button.  Click a fifth time to end
%  selection process.
while i <= 5
    [xtemp,ytemp,button] = GINPUT(1);
    if (button == 1)
        plot(xtemp,ytemp,'r*')
        xc = xtemp + R*cos(deg2rad(theta));
        yc = ytemp + R*sin(deg2rad(theta));
        plot(xc,yc,'g-')
        x = [x; xtemp];
        y = [y; ytemp];
        i = i + 1;
    elseif (button == 3)
        dist = (xtemp - x).^2 + (ytemp - y).^2;
        [index] = find(dist==min(dist))
        x(index) = xtemp;
        y(index) = ytemp;
        close
        imshow(I)
        hold on
        plot(x,y,'r*')
        for j = 1:size(x,1)
            xc = x(j) + R*cos(deg2rad(theta));
            yc = y(j) + R*sin(deg2rad(theta));
            plot(xc,yc,'g-')
        end
```

```
    elseif (button == 2)
        break
    end
end

% Record location of registration marks.
x = x(1:4);
y = y(1:4);
A=[x y];
```

Sectioning Distortion Calculation

sectioningdistortion.m

```
% This program calculates distortions due to sectioning.

clear all
close all

% Load registration hole location data by inputting file name.
Xall = load([<input>]);

[numpoints, numrows]=size(Xall);

% Set-up matrices to be used to solve for affine transformation
%  coefficients(uses least squares differences).
 for d=1:4:numpoints
     X1temp=Xall(d:d+3,1);
     X2temp=Xall(d:d+3,2);
     x1temp=Xall(d:d+3,3);
     x2temp=Xall(d:d+3,4);
     A = zeros(8,6);
     a=zeros(8,1);
     for i = 1:2:7
        A(i,3) = 1;
     end
     for i=2:2:8
        A(i,6)=1;
     end
     for j = 1:4
        A(2*j-1,1)=X1(j,1);
        A(2*j-1,2)=X2(j,1);
        A(2*j,4)=X1(j,1);
        A(2*j,5)=X2(j,1);
    end
    for k=1:4
        a(2*k-1,1)=x1(k,1);
        a(2*k,1)=x2(k,1);
    end

    % Solve for affine transformation coefficients.
    C= inv(transpose(A)*A)*transpose(A)*a;

    % Place coefficients in transformation matrix.
        Aff= [C(1), C(2), C(3);
        C(4), C(5), C(6);
        0,    0,    1];

    IAff=(Aff);

    % Rotation.
    rot= asin((Aff(1,2)-Aff(2,1))/2);
```

```
    % Translation Component.
    T = [1,  0,  -Aff(1,3);
        0,  1,  -Aff(2,3);
        0,  0,         1];

    % Rotation Component.
    R = [cos(rot),  -sin(rot),  0;
        sin(rot),   cos(rot),  0;
        0,             0,  1];

    % Deformation Matrix.
    Adef_inv = [inv(R)*inv(T)*inv(Aff)];

    % Green Strain.
    E(1,1)=0.5*((IAff(1,1)^2)+(IAff(2,1)^2)-1);
    E(2,2)=0.5*((IAff(1,2)^2)+(IAff(2,2)^2)-1);
    E(1,2)=0.5*((IAff(1,1)*IAff(1,2))+(IAff(2,1)*IAff(2,2)));
    Ex=E(1,1);
    Ey=E(2,2);
    Exy=E(1,2);

    % Cauchy Strain.
    e(1,1)=IAff(1,1)-1;
    e(2,2)=IAff(2,2)-1;
    e(1,2)=0.5*(IAff(1,2)+IAff(2,1));
    ex=e(1,1);
    ey=e(2,2);
    exy=e(1,2);

    % Principal Strain.
    e1 = (ex + ey)/2+(((ex-ey)/2).^2+exy.^2).^0.5;
    e2 = (ex + ey)/2-(((ex-ey)/2).^2+exy.^2).^0.5;
    theta = rad2deg(atan((-ex+ey)./exy));
    E1 = (Ex + Ey)/2+(((Ex-Ey)/2).^2+Exy.^2).^0.5;
    E2 = (Ex + Ey)/2-(((Ex-Ey)/2).^2+Exy.^2).^0.5;
    Theta = rad2deg(atan((-Ex+Ey)./Exy));

    % Record results.
    Strainc(1:6,(d+3)/4)=[ex; ey; exy; e1; e2; theta];
    Straing(1:6,(d+3)/4)=[Ex; Ey; Exy; E1; E2; Theta];
    Affine(1:6,(d+3)/4)=[C(1);C(2);C(3);C(4);C(5);C(6)];
end
```

Distortion Correction

distortioncorrection.m

```
% This code corrects for distortions.

clear all
close all

% Read in lumen and outer boundary point data file from sectioned and
%  stained segmentation.
Bpts=load([<input>]);

% Input inverse of affine transformation matrix.
Ai=[<input>];

% Read in lumen and outer boundary point data file from embedded
%  segmentation.
Bpts2=load([<input>]);

% Input shrinkage value.
s=<input>;

% Apply sectioning distortion correction.
C(1)=Ai(1,1);
C(2)=Ai(1,2);
C(3)=Ai(1,3);
C(4)=Ai(2,1);
C(5)=Ai(2,2);
C(6)=Ai(2,3);

[r c]=size(Bpts);

for i=1:r
    X(i,1)=Bpts(i,1)*C(1)+Bpts(i,2)*C(2)+C(3);
    X(i,2)=Bpts(i,1)*C(4)+Bpts(i,2)*C(5)+C(6);
end

% Save sectioning distortion corrected point data.
save sectioning_corrected.txt X -ASCII

% Apply shrinkage distortion correction.
[r c]=size(Bpts2);

for i=1:r
    X(i,1)=Bpts2(i,1)*sqrt(1+s);
    X(i,2)=Bpts2(i,2)*sqrt(1+s);
end

% Save shrinkage distortion corrected point data.
save shrinkage_corrected.txt X -ASCII
```

Error in Correction Calculation

correctionerror.m

```
% This program calculates the error in the distortion correction.

clear all;
close all;

% Read in original segmentation by inputting file name.
j=imread([<input>]);
BW1 = im2bw(j,0.5);
imshow(BW1)

% Read in corrected reconstruction by inputting file name.
j2=imread([<input>]);
BW12 = im2bw(j2,0.5);

% Subtract original segmentation from corrected reconstruction.
Ic=BW12-BW1;

% Count number of non-corresponding pixels in subtracted image.
counter=0;
[m,n]=size(Ic)
for a=1:m
    for b=1:n
        if Ic(a,b)==1
            counter=counter+1;
        end
        if Ic(a,b)==-1
            counter=counter+1;
        end
    end
end
pixelsnc(d,1)=counter;

% Count number of pixels in original segmentation.
F = imfill(BW1,'holes');
counter=0;
[m,n]=size(F)
for a=1:m
    for b=1:n
        if F(a,b)==1
            counter=counter+1;
        end
    end
end
pixelsf(d,1)=counter;

% Calculate and store error.
error(d,1)=pixelsnc(d,1)/pixelsf(d,1)
end
```

Specific Aim II:

Develop three-dimensional mechanical models of human coronary atherosclerotic plaques based on minimally distorted histologic sections.

Landmark Identification

landmarkidentification.m

```
% This program is used to identify a landmark in an unstained and
%  stained image of a slide.

clear all
close all
numslides = <input>;
t=1;

for k = 1:numslides
    % Read in unstained image.
    I = imread([ 'Unstained\' num2str(k) '.tif']);

    % Zoom in on image by pressing the left mouse button and zoom out
    by
     %  pressing right mouse button.  Press enter to exit zooming.
    imshow(I)
    set(gcf,'Pointer','fullcross')
    hold on
    x = [];
    y = [];
    i = 1;
    zoom on
    pause

   % Select landmark by pressing the left mouse button.  Selection is
   %  marked with a red star. Click left mouse button to confirm
   %  selection.
    while i <= 2
        [xtemp,ytemp,button] = GINPUT(1);
        if (button == 1)
            plot(xtemp,ytemp,'r*')
            x = [x; xtemp];
            y = [y; ytemp];
            i = i + 1;
        end
    end
    close all

    % Record location of landmark in unstained image.
    A(t,1)=x(1,1);
    A(t,2)=y(1,1);
```

```
    % Read in stained image.
    I = imread([ 'Stained\' num2str(k,'%03i') '.tif']);

    % Zoom in on image by pressing the left mouse button and zoom out
       by
     %  pressing right mouse button.  Press enter to exit zooming.
    imshow(I)
    set(gcf,'Pointer','fullcross')
    hold on
    x = [];
    y = [];
    i = 1;
    zoom on
    pause

    % Select landmark by pressing the left mouse button.
    %  Selection is marked with a red star. Click left mouse button to
    %  confirm selection.
    while i <= 2
        [xtemp,ytemp,button] = GINPUT(1);
        if (button == 1)
            plot(xtemp,ytemp,'r*')
            x = [x; xtemp];
            y = [y; ytemp];
            i = i + 1;
        end
    end
    close all

    % Record location of landmark in stained image.
    A(t,3)=x(1,1);
    A(t,4)=y(1,1);

    % Calculate and record translations into a TXT file.
    T(t,1)=A(t,3)-A(t,1);
    T(t,2)=A(t,4)-A(t,2);
    t=t+1;
    Tr=round(T);
    dlmwrite('landmarklocation.txt', Tr);
end
```

Stained Slide Alignment

alignstainedslide.m

```
% This program is used to align an image of a stained slide with an
%  image of the same unstained slide.

numslides = <input>;

for k=1:numslides
    close all
    % Load in text file containing translation data.
    T=dlmread('<input>');
    tx=-T(k,1);
    ty=T(k,2);

    % Read in stained image.
    I2=imread([ 'Stained\' num2str(k,'%03i') '.tif']);
    for i=1:3
        I=I2(:,:,i);

        % Translate stained image in the x-direction.
        M=size(I);
        Mr=M(2);
        if tx>0
            I(:,tx+1:Mr)=I(:,1:Mr-tx);
            I(:,1:tx)=0;
        elseif tx<0
            I(:,1:Mr-(-tx))=I(:,(-tx)+1:Mr);
            I(:,Mr-(-tx)+1:Mr)=0;
        end

        % Translate stained image in the y-direction.
        Mc=M(1);
        if ty<0
            I((-ty)+1:Mc,:)=I(1:Mc-(-ty),:);
            I(1:(-ty),:)=0;
        elseif ty>0
            I(1:Mc-ty,:)=I(ty+1:Mc,:);
            I(Mc-ty+1:Mc,:)=0;
        end
        I2(:,:,i)=I;
    end

    % Save translated image of the stained slide as a TIFF file.
    imwrite(I2,['Stained Translated\' num2str(k,'%04i') '.tif'])
end
```

Image Cropping

cropimages.m

```
% This program identically crops unstained and translated stain images.

clear all
close all
numslides = <input>;

% Input size of resulting cropped image.
height = <input>;
width = <input>;
t=1;
for k=1:numslides
    close all

    % The following process is repeated 4 times because there are
    %  4 sections on a slide.
    for f=1:4
        % Read in the unstained slide image.
        I = imread([ 'Unstained\' num2str(k) '.tif']);

        % Select a point above and to the left of a section by pressing
        %  the left mouse button. This point will correspond to the
top-
        %  left point in the cropped images.
        imshow(I)
        set(gcf,'Pointer','fullcross')
        hold on
        x = [];
        y = [];
        i = 1;
        while i <= 1
            [xtemp,ytemp,button] = GINPUT(1);
            if (button == 1)
                plot(xtemp,ytemp,'r*')
                x = [x; xtemp];
                y = [y; ytemp];
                i = i + 1;
            end
        end
        close all

        % Store the location of the selected point.
        orgx=x(1,1);
        orgy=y(1,1);

        % Read in the translated image of the stained slide.
        I2 = imread([ 'Stained Translated\' num2str(k,'%04i') '.tif']);
```

```
        % Crop the unstained slide image.
        I3=imcrop(I,[orgx,orgy, height, width]);
        [r3 c3 x3]= size(I3);
        I3c=zeros(width+1, height+1,1);
        I3c=zeros(width+1, height+1,1);
        I3c=zeros(width+1, height+1,1);
        I3c=uint8(I3c);
        I3c(1:r3,1:c3,1)= I3(1:r3,1:c3,1);
        I3c(1:r3,1:c3,2)= I3(1:r3,1:c3,2);
        I3c(1:r3,1:c3,3)= I3(1:r3,1:c3,3);

        % Crop the translated stained slide image.
        I4=imcrop(I2,[orgx,orgy, height, width]);
        [r4 c4 x4]= size(I4);
        I4c=zeros(width+1, height+1,1);
        I4c=zeros(width+1, height+1,1);
        I4c=zeros(width+1, height+1,1);
        I4c=uint8(I4c);
        I4c(1:r3,1:c3,1)= I4(1:r3,1:c3,1);
        I4c(1:r3,1:c3,2)= I4(1:r3,1:c3,2);
        I4c(1:r3,1:c3,3)= I4(1:r3,1:c3,3);

        % Visually confirm unstained and translated stained images
        %  match-up.
        imshow(I3c);
        figure;
        imshow(I4c);

        % Save cropped images as TIFF files.
        imwrite(I3c,['Unstained Cropped\' num2str(t,'%04i') '.tif'])
        imwrite(I4c,['Stained Cropped\' num2str(t,'%04i') '.tif'])
        t=t+1;
    end
end
```

Stained Section Alignment

alignstainedsection.m

```
% This program automatically aligns stained cropped images by applying
a
%  transformation that was obtained by manually aligning unstained
%  cropped images in Amira.

numsections = <input>;

% Load in text file containing Amira transformation data. 1st column is
%  translation in x-direction, 2nd is translation in y-direction, 3rd
is
%  rotation, and 4th is flip (-1=no flip; 1=flip).
A = dlmread('<input>');

txc=A(:,1);
tyc=A(:,2);
rotc=A(:,3);
flipc=A(:,4);
p=1;
for k=1:numsections
    tx=txc(k,1);
    ty=tyc(k,1);
    rot=rotc(k,1);
    flip=flipc(k,1);
    % Read in stained cropped image.
    I2 = imread([ 'Stained Cropped\' num2str(k,'%03i') '.tif']);
    for i=1:3
        I=I2(:,:,i);

        % Flip image if required.
        if flip==1
            I=fliplr(I);
        End

        % Rotate image.
        I=imrotate(I,rot,'bilinear','crop');

        % Translate image in x-direction.
        M=size(I);
        Mr=M(2);
        if tx>0
            I(:,tx+1:Mr)=I(:,1:Mr-tx);
            I(:,1:tx)=0;
        elseif tx<0
            I(:,1:Mr-(-tx))=I(:,(-tx)+1:Mr);
            I(:,Mr-(-tx)+1:Mr)=0;
        End
```

```
        % Translate image in y-direction.
        Mc=M(1);
        if ty<0
            I((-ty)+1:Mc,:)=I(1:Mc-(-ty),:);
            I(1:(-ty),:)=0;

        elseif ty>0
            I(1:Mc-ty,:)=I(ty+1:Mc,:);
            I(Mc-ty+1:Mc,:)=0;
        end
        I2(:,:,i)=I;
    end

    p=p+1;
    % Save translated stained images as TIFF files.
    imwrite(I2,['Stained Aligned\' num2str(k,'%03i') '.tif'])
end
```

Automatic Segmentation

autoseg.m

```
% This program automatically segments stained aligned images based on
%  the manual segmentation of a single representative image.  Pixels\
%  were classified as either background, media, or other tissue.

numsections = <input>;

% Read in manually segmented image by inputting file name.
I = imread('<input>');

I=double(I);
[rowI colI z3]=size(I);

% Read in original stained aligned image used to generate manual
%  segmentation.
J=imread('Stained Aligned\<input>.tif');
{rowJ colJ]=size(J);
J1=J;

% Obtain the pixel intensity value of the 3 components present in the
%  manual segmentation.
z=nonzeros(I);
z=sort(z);
[zr zc]=size(z);
v(1,1)=z(1,1);
x=2;
for i=2:zr-1
    if z(i,1)~=z(i+1,1);
        v(x,1)=z(i+1,1);
        x=x+1;
    end
end
v1=v(1,1);
v2=v(2,1);
v3=v(3,1);

% Calculate the average color of the media.
n=0;
for i=1:rowI
    for j=1:colI
        if I(i,j)==v1;
            A(n+1,1)=J1(i,j,1);
            A(n+1,2)=J1(i,j,2);
            A(n+1,3)=J1(i,j,3);
            n=n+1;
        end
    end
end
a=mean(A);
ra=a(1,1);
ga=a(1,2);
ba=a(1,3);
```

```
% Calculate the average color of the other tissue.
n=0;
for i=1:rowI
    for j=1:colI
        if I(i,j)==v2;
            B(n+1,1)=J1(i,j,1);
            B(n+1,2)=J1(i,j,2);
            B(n+1,3)=J1(i,j,3);
            n=n+1;
        end
    end
end
b=mean(B);
rb=b(1,1);
gb=b(1,2);
bb=b(1,3);

% Calculate the average color of the background.
n=0;
for i=1:rowI
    for j=1:colI
        if I(i,j)==v3;
            C(n+1,1)=J1(i,j,1);
            C(n+1,2)=J1(i,j,2);
            C(n+1,3)=J1(i,j,3);
            n=n+1;
        end
    end
end
c=mean(C);
rc=c(1,1);
gc=c(1,2);
bc=c(1,3);
i=0;

for i=1:numsections
    % Read in and show image of stained aligned section.
    I=imread(['Stained Aligned\' num2str(i-1, '%03i') '.tif']);
    J1=I;
    imshow(J1);
    J2=J1;
    JH=zeros(rowI,colI);
    JB=zeros(rowI,colI);
    JO=zeros(rowI,colI);
    for p=1:rowI
        for j=1:coli

            % Store pixel value
            x=J1(p,j,1);
            if x > 0
                r8=J1(p,j,1);
                g8=J1(p,j,2);
                b8=J1(p,j,3);
                r=double(r8);
                g=double(g8);
                b=double(b8);
```

```
                % Calculate distance between pixel and average colors.
                C1=(sqrt((r-ra)^2+(g-ga)^2+(b-ba)^2));
                C2=(sqrt((r-rb)^2+(g-gb)^2+(b-bb)^2));
                C3=(sqrt((r-rc)^2+(g-gc)^2+(b-bc)^2));
                C=[C1;C2;C3];

               % Identify component whose average color is nearest to
               %  the pixel color.
                Cs=sort(C);
                t=Cs(1,1);

               % Assign closest average color to pixel.
                if t==C1
                    J2(p,j,1)=v1;
                    J2(p,j,2)=v1;
                    J2(p,j,3)=v1;
                    JH(p,j,1)=v1;
                    JH(p,j,2)=v1;
                    JH(p,j,3)=v1;
                end
                if t==C2
                    J2(p,j,1)=v2;
                    J2(p,j,2)=v2;
                    J2(p,j,3)=v2;
                    JO(p,j,1)=v2;
                    JO(p,j,2)=v2;
                    JO(p,j,3)=v2;
                end
                if t==C3
                    J2(p,j,1)=v3;
                    J2(p,j,2)=v3;
                    J2(p,j,3)=v3;
                    JB(p,j,1)=v3;
                    JB(p,j,2)=v3;
                    JB(p,j,3)=v3;
                end
            end
        end
    end
    J2=uint8(J2);

    % Show the automatically segmented image.
    imshow(J2);

    % Save translated stained images as TIFF files.
    imwrite(J2,['AutoSeg\' num2str(i,'%01i') '.tif'],'tif')
end
```

Arterial Wall Segmentation

wall.m

```
% This program is used to generate binary images of the arterial wall
%  based on automatically segmented images.

clear all;
close all;

numsections = <input>;

for g=1:numsections
    close all;
    clear Hall;
    clear Fall;
    clear Lm;
    % Read in automatically segmented image.
    I = imread(['AutoSeg\' num2str(g,'%01i') '.tif']);
    I=double(I);
    [rowI colI z3]=size(I);

    % Obtain the pixel intensity value of the 3 components present in
    %  the automatic segmentation.
    z=nonzeros(I);
    z=sort(z);
    [zr zc]=size(z);
    v(1,1)=z(1,1);
    x=2;
    for i=2:zr-1
        if z(i,1)~=z(i+1,1);
            v(x,1)=z(i+1,1);
            x=x+1;
        end
    end
    [vr vc]=size(v);

    % Obtain the pixel value of the media.
    vh=min(v);

    % Obtain the pixel value of the background.
    vb=max(v);

    % Identify all media.
    for i=1:rowI
        for j=1:colI
            if I(i,j,1)==vh;
                Hall(i,j,1)=255;
                Hall(i,j,1)=255;
                Hall(i,j,1)=255;
            end
```

```
        if I(i,j,1)~=vh
            Hall(i,j,1)=0;
            Hall(i,j,1)=0;
            Hall(i,j,1)=0;
        end
    end
end

% Save binary image of health tissue as a TIFF file.
imwrite(Hall,['Media\' num2str(g,'%01i') '.tif'],'tif')

% Label the components in the binary image.
Hall = im2bw(Hall);
[L, num]=bwlabel(Hall);

% Find and isolate the largest component in a separate image.
sizedata = regionprops(L,'area');
val= max([sizedata.Area]);
loc = find([sizedata.Area]==val);
for i=1:rowI
    for j=1:colI
        H(i,j)=0;
        if L(i,j)==loc;
            H(i,j,1)=1;
        end
    end
end

% Find outer boundary by filling holes.
Outer = imfill(H,'holes');

% Identify all background.
for i=1:rowI
    for j=1:colI
        if I(i,j,1)==vhigh;
            Lm(i,j,1)=255;
            Lm(i,j,1)=255;
            Lm(i,j,1)=255;
        end
        if I(i,j,1)~=vhigh
            Lm(i,j,1)=0;
            Lm(i,j,1)=0;
            Lm(i,j,1)=0;
        end
    end
end

% Label the components in the binary image.
Lm = im2bw(Lm);
[L, num]=bwlabel(Lm);
```

```
    % Find and isolate the 2nd largest component in a separate image.
    sizedata = regionprops(L,'area');
    valsort=sort([sizedata.Area]);
    [x y]=size(valsort);
    val= valsort(y-1);
    loc = find([sizedata.Area]==val);
    for i=1:rowI
        for j=1:colI
            P3(i,j)=0;
            if L(i,j)==loc;
                P3(i,j,1)=1;
            end
        end
    end

    % Fill holes and save image of lumen as a TIFF file.
    Lumen = imfill(P3,'holes');
    imwrite(Lumen,['Lumen\' num2str(g,'%01i') '.tif'],'tif')

    % Obtain binary image of the arterial wall
    P5=~Lumen;
    Wall=Outer & P5;
    figure;

    % Save image of arterial wall as a TIFF file
    imwrite(Wall,['Wall\' num2str(g,'%01i') '.tif'],'tif')
end
```

Combine Segmentations

correctionerror.m

```
% This program is used to obtain a segmented image of a stained section
%  in which each pixel has been classified as media, fibrous tissue,
%  lipid, calcification, or background.

numsections = <input>;

for g=1:numsections
    % Read in binary image of wall.
    W=imread(['Wall\' num2str(g,'%04i') '.tif']);
    W=double(W);
    [row col z]=size(W);

    % Read in binary image of media.
    H=imread(['Media\' num2str(g,'%04i') '.tif']);
    H=double(H);

    % Read in binary image of lipid (PNG from Amira).
    L=imread(['Lipid\' num2str(g,'%04i') '.png']);
    L=double(L);

    % Read in binary image of calification (PNG from Amira).
    C=imread(['Calcification\' num2str(g,'%04i') '.png']);
    C=double(C);

    % Combined segmentations into a single image.  All wall pixels not
    %  classified as media, lipid, or calcification are classified
    %  as fibrous tissue.
    for i=1:row
        for j=1:col
            Seg(i,j,1)=0;
            Seg(i,j,2)=0;
            Seg(i,j,3)=0;

           % Make fibrous tissue blue.
            if W(i,j)==1
                Seg(i,j,1)=0;
                Seg(i,j,2)=0;
                Seg(i,j,3)=255;

                % Make media green.
                if H(i,j)==1
                    Seg(i,j,1)=0;
                    Seg(i,j,2)=255;
                    Seg(i,j,3)=0;
                end
```

```
                % Make lipid white.
                if L(i,j)==1
                    Seg(i,j,1)=255;
                    Seg(i,j,2)=255;
                    Seg(i,j,3)=255;
                end

                % Make calcification red.
                if C(i,j)==1
                    Seg(i,j,1)=255;
                    Seg(i,j,2)=0;
                    Seg(i,j,3)=0;
                end
            end
        end
    end

   % Save combined segmentation as a TIFF file.
    Seg=uint8(Seg);
    imwrite(Seg,['SegCombine\' num2str(g,'%01i') '.tif'],'tif')
end
```

Gaussian Blurring Application

blurring.m

```
% This program is used to smooth arterial wall surfaces using Gaussian
%  blurring.

numsections = <input>;

for g=1:numsections;
    % Read in binary image of arterial wall.
    I = imread(['Wall\' num2str(g,'%04i') '.png']);
    I=double(I);

    % Apply Gaussian blurring.
    H = fspecial('gaussian',[5 5], 3);
    Blur = imfilter(I,H,'replicate');
    Blur1 = im2bw(Blur,.1);

    % Save blurred arterial wall image as a TIFF file.
    imwrite(Blur1,['Wall Blurred\' num2str(g,'%04i') '.tif'],'tif')
end
```

Downsize Point Clouds

downsizingpointclouds.m

```
% This program downsizes the point cloud data.

clear all
close all

f=1;
k=1;
numsections = <input>;

for g=1:numsections
    % Read in blurred arterial wall image.
    I = imread(['Wall Blurred\' num2str(g,'%04i') '.png']);
    I2=I;

    % Define perimeter pixels as boundary coordinates.
    BW = bwperim(I2,4);
    [y x] = find(BW~=0);
    X = [x y];

    % Calculate centroid.
    cgx = mean(X(:,1));
    cgy = mean(X(:,2));

    % Sort coordinates in sequential order, beginning with the first
    %  point.  Walk through coordinate data, assigning nearest point to
    %  sorted matrix and eliminating it from the unsorted matrix.
    new_pos = 1;
    Xsort=[X(new_pos,:)];
    X(new_pos,:)=[];
    min_dX2 = [];
    while size(X,1)>=1
        dX = repmat(Xsort(end,:),size(X,1),1) - X;
        dX2 = sum(dX.^2,2);
        min_dX2 = [min_dX2; min(dX2)];
        new_pos = find(dX2 == min(dX2));
        new_pos = new_pos(1,1);
        Xsort=[Xsort; X(new_pos,:)];
        X(new_pos,:)=[];
    end


    imax=find(min_dX2 == max(min_dX2));
    Xout = Xsort(1:imax,:);
    Xin = Xsort(imax+1:end,:);
```

```
% Check for problems in boundary identification.
    ifind = find(min_dX2 > 2.1);
    if length(ifind) > 1
        disp(['WARNING: More than two boundaries may be present'])
        disp(['Please examine the ' num2str(length(ifind)) ' locations
              in the BW image.'])
        disp(['Which include the following sorted node locations: '
        num2str(ifind')])
        figure
        imshow(BW)
        hold on
        axis equal
        for i = 1:length(ifind)
            j = ifind(i);
            plot(Xsort(j:j+1,1),Xsort(j:j+1,2),'r-')
            plot(Xsort(j:j+1,1),Xsort(j:j+1,2),'rx')
        end
    end

    % Plot cg and coordinate data as lines on segmented image.
    figure
    imshow(I)
    hold on
    axis equal
    plot(cgx,cgy, 'y+')
    plot(Xout(:,1),Xout(:,2), 'c-')
    plot(Xin(:,1),Xin(:,2), 'y-')

    % Find the point at theta = 0 on the outer boundary and reorder the
    %  point set so it starts in sequence from this point. Find all
    %  four points with y-coordinate of cg. Find point with greatest
    %  corresponding x-coordinate.
    ifindy = find(Xout(:,2)==round(cgy));
    ifindxy = find(Xout(ifindy,1) == max(Xout(ifindy,1)));
    istart = ifindy(ifindxy);
    Xout = [Xout(istart:end,:); Xout(1:istart-1,:)];

    % Determine if order of outer points is CCW, if not reorder the
    %  points.
    [theta, rho] = cart2pol(Xout(:,1)-cgx, Xout(:,2)-cgy);
    dtheta = [theta(end); theta] - [theta; theta(1)];
    sum_dtheta = (sum(dtheta) - min(dtheta) - max(dtheta))*360/2/pi;
    if(sum_dtheta > 0)
        disp('Outer boundary is correctly ordered counterclockwise.')
    elseif(sum_dtheta < 0)
        disp('Outer boundary is being re-ordered counterclockwise.')
        Xout = Xout(end:-1:1,:);
    end
```

```
% Downsample outer boundary to 200 points in 4 quadrants.
    ifindy = find(Xout(:,2)==round(cgy));
    imin = find(Xout(ifindy,1) == min(Xout(ifindy,1)));
    out180 = ifindy(imin);
    ifindx = find(Xout(:,1)==round(cgx));
    out90 = min(ifindx);
    out270 = max(ifindx);
    Xoutd = [];
    dn = out90/50;
    for i = 1:50;
        istep = round((i-1)*dn) + 1;
        Xoutd = [Xoutd; Xout(istep,:)];
    end
    dn = (out180-out90)/50;
    for i = 1:50;
        istep = round((i-1)*dn) + out90;
        Xoutd = [Xoutd; Xout(istep,:)];
    end
    dn = (out270-out180)/50;
    for i = 1:50;
        istep = round((i-1)*dn) + out180;
        Xoutd = [Xoutd; Xout(istep,:)];
    end
    dn = (length(Xout)-out270)/50;
    for i = 1:50;
        istep = round((i-1)*dn) + out270;
        Xoutd = [Xoutd; Xout(istep,:)];
    end

    % Find the point at theta = 0 on the inner boundary and reorder the
    %  point set so it starts in sequence from this point.
    ifindy = find(Xin(:,2)==round(cgy));
    plot(Xin(ifindy(1),1),Xin(ifindy(1),2),'rx')
    plot(Xin(ifindy(2),1),Xin(ifindy(2),2),'ro')
    ifindxy = find(Xin(ifindy,1) == max(Xin(ifindy,1)));
    istart = ifindy(ifindxy);
    Xin = [Xin(istart:end,:); Xin(1:istart-1,:)];

    % Determine if order of inner points is CCW, if not reorder the
    %  points.
    [theta, rho] = cart2pol(Xin(:,1)-cgx, Xin(:,2)-cgy);
    dtheta = [theta(end); theta] - [theta; theta(1)];
    sum_dtheta = (sum(dtheta) - min(dtheta) - max(dtheta))*360/2/pi;
    if(sum_dtheta > 0)
        disp('Inner boundary is correctly ordered counterclockwise.')
    elseif(sum_dtheta < 0)
        disp('Inner boundary is being re-ordered counterclockwise.')
        Xin = Xin(end:-1:1,:);
    end
```

```
% Downsample inner boundary to 200 points in 4 quadrants.
    ifindy = find(Xin(:,2)==round(cgy));
    imin = find(Xin(ifindy,1) == min(Xin(ifindy,1)));
    in180 = ifindy(imin);
    ifindx = find(Xin(:,1)==round(cgx));
    in90 = min(ifindx);
    in270 = max(ifindx);
    Xind = [];
    dn = in90/50;
    for i = 1:50;
        istep = round((i-1)*dn) + 1;
        Xind = [Xind; Xin(istep,:)];
    end
    dn = (in180-in90)/50;
    for i = 1:50;
        istep = round((i-1)*dn) + in90;
        Xind = [Xind; Xin(istep,:)];
    end
    dn = (in270-in180)/50;
    for i = 1:50;
        istep = round((i-1)*dn) + in180;
        Xind = [Xind; Xin(istep,:)];
    end
    dn = (length(Xin)-in270)/50;
    for i = 1:50;
        istep = round((i-1)*dn) + in270;
        Xind = [Xind; Xin(istep,:)];
    end

   % Plot sorted and downsampled data with quadrants
    plot(Xoutd(:,1), Xoutd(:,2), 'cx')
    plot(Xind(:,1), Xind(:,2), 'yx')
    plot([Xind(1,1) Xoutd(1,1)],[Xind(1,2) Xoutd(1,2)], 'r-')
    plot([Xind(50,1) Xoutd(50,1)],[Xind(50,2) Xoutd(50,2)], 'r-')
    plot([Xind(100,1) Xoutd(100,1)],[Xind(100,2) Xoutd(100,2)], 'r-')
    plot([Xind(150,1) Xoutd(150,1)],[Xind(150,2) Xoutd(150,2)], 'r-')
    XindT(n:n-1+200,1)=Xind(:,1);
    XindT(n:n-1+200,2)=Xind(:,2);
    XindT(n:n-1+200,3)=g;
    XoutdT(n:n-1+200,1)=Xoutd(:,1);
    XoutdT(n:n-1+200,2)=Xoutd(:,2);
    XoutdT(n:n-1+200,3)=g;
    n=n+200;
    [is c]=size(Xin);
    [os c]=size(Xout);
    XinT(f:f+is-1,1)=Xin(:,1);
    XinT(f:f+is-1,2)=Xin(:,2);
    XinT(f:f+is-1,3)=g;
    XoutT(k:k+os-1,1)=Xout(:,1);
    XoutT(k:k+os-1,2)=Xout(:,2);
    XoutT(k:k+os-1,3)=g;
    f=f+is;
    k=k+os;
end
```

```
% Impose resolution values
XoutdT(:,1:2)=19.05*XoutdT(:,1:2);
XoutdT(:,3)=150*XoutdT(:,3);
XindT(:,1:2)=19.05*XindT(:,1:2);
XindT(:,3)=150*XindT(:,3);

% Record reduced point cloud data for outer and luminal surface as TXT
%  files.
save Outerpointcloud.txt XoutdT -ASCII
save Luminalpointcloud.txt XindT -ASCII
```

Diameter Calculation

diametercalculations.m

```
% This program calculates the inner and outer diameter on the artery at
% specified axial locations.

clear all
close all

numsections=<input>;
ii=1;

for ne=1:numsections

    % Read in binary image of arterial wall.
    Ii=imread(['Wall\' num2str(ne,'%04i') '.png']);

    [r c d]=size(Ii);

    % Generate image in which lumen is filled in.
    It(:,:,1)=ones(r,c).*255;
    It(:,:,2)=ones(r,c).*255;
    It(:,:,3)=ones(r,c).*255;
    for a2=1:r
        for b2=1:c
            if Ii(a2,b2,1)==0
                if Ii(a2,b2,2)==0
                    if Ii(a2,b2,3)==0
                        It(a2,b2,1)=0;
                        It(a2,b2,2)=0;
                        It(a2,b2,3)=0;
                    end
                end
            end
        end
    end
    It = im2bw(It);
    I=imfill(It,'holes');

    % Calculate outer diameter.
    [L, num]=bwlabel(I);
    sizedata = regionprops(L,'EquivDiameter');
    val=sort([sizedata.EquivDiameter]);

    % Calculate inner diameter.
    I2=I-It;
    [L2, num2]=bwlabel(I2);
    sizedata2 = regionprops(L2,'EquivDiameter');
    val2=sort([sizedata2.EquivDiameter]);
```

```
    % Store results.
    idiam(ne,1)=val;
    odiam(ne,1)=val2;

    clear I I2 Ii It L L2 a2 b2 c num num2
    clear r sizedata sizedata2 val val2

end
```

Distance Between Element Centroids Calculation

correctionerror.m

```
% This program calculates the average distance between elements'
%  centroids for a FEM generated in Ansys.

clear all
close all
n=1;

slicestart = <input>;
slicestop = <input>;

% Load in text file obtained from Ansys containing centroid data by
%  inputting file name.
X = load(['<input>']);

% Remove resolution constraints.
X(:,1)=X(:,1)/19.05;
X(:,2)=X(:,2)/19.05;
X(:,3)=X(:,3)/150;

% Sort data by slice number.
Xr=sortrows(X,3);
Z=Xr(:,3);
for lp=slicestart:slicestop-1
    clear C;

    % Find all centroids between 2 slices of interest.
    ind=find(lp < Z & Z < (lp+1));
    [r1 c1]= size(ind);
    C(1:r1,1)=Xr(ind(1,1):ind(r1,1),1);
    C(1:r1,2)=Xr(ind(1,1):ind(r1,1),2);
    C(1:r1,3)=Xr(ind(1,1):ind(r1,1),3);
    [r c]=size(C);

    %  Walk through centroid data and calculate distance between a
point
    %   and its nearest neighbor.  Eliminate point from matrix after
    %   calculation.
    for f=1:r-1
        clear XI;
        clear YI;
        clear d;
        XI=C(f:r,1);
        YI=C(f:r,2);
        a=1;
```

```
        for i=f:r-1
            b=a+1;
            x2=XI(b,1);
            x1=XI(a,1);
            y2=XI(b,1);
            y1=XI(a,1);
            xd=x2-x1;
            yd=y2-y1;
            d(a,1)=sqrt(xd^2+yd^2);
            a=a+1;
        end
        R(f,1)=min(d);
    end

    % Calculate average distance between points for a single increment.
    FDall(lp-5,1)=mean(R);
end

% Calculate distance between all centroids.
FD=mean(FDall)
```

Element Elastic Modulus Calculation

elasticmodulus.m

```
% This program calculates an elastic modulus value for each element
%   of a FEM generated in Ansys.

clear all

slicestart = <input>;
slicestop = <input>;
FD = <input>;

% Load in text file obtained from Ansys containing centroid data by
%  inputting file name.
X = load(['<input>']);

% Remove resolution constraints.
X(:,1)=X(:,1)/19.05;
X(:,2)=X(:,2)/19.05;
X(:,3)=X(:,3)/150;
[r c]=size(X);
numelements = r;
for g=1:numelements;
    close all

% Identify slice number of 2 sections nearest the element's centroid.
s2= X(g,3);
    s1= floor(s2);
    s3= ceil(s2);
        if s1 > slicestart
        if s3 < slicestop

            % Read in segmentation above centroid.
            I = imread(['SegCombine\' num2str(s1,'%04i') '.png']);
            % Identify circle centered at x and y centroid locations
            %   with a radius equal to 1/2 the average distance between
            %   element centroids.
            x=X(g,1);
            y=X(g,2);
            I = I(:,:,1);
            R = FD/2;
            Fx = 1:size(I,1);
            Fy = 1:size(I,2)';
            dx = x - Fx;
            dy = y - Fy;
            for i = 1:length(dx)
                for j = 1:length(dy)
                    ds2(j,i) = dx(i)^2+dy(j)^2;
                end
            end
```

```
% Plot the circle.
[jfind, ifind] = find(ds2<=R^2);
map = [0 0 0; 0 0 1; 0 1 0; 0 1 1; 1 1 1];
imshow(I,map)
hold on
plot(ifind, jfind, 'rx')
axis equal

% Determine intensity values for components.
for i = 1:length(ifind)
    V(i,1) = I(jfind(i), ifind(i));
end

% Calculate area fractions of components in the circle.
%  Estimate the elastic modulus for the circle.
pixcount(g,1:4) = [length(find(V==1)), length(find(V==2)),
   length(find(V==3)), length(find(V==4))];
fpix(g,1:4) = pixcount(g,1:4)/sum(pixcount(g,1:4));
mpv = [3.88E5 2.45E6 1.82E7 1.07E8];
mp(g,1) = dot(fpix(g,1:4),mpv);

% Read in segmentation below centroid.
I = imread(['SegCombine\' num2str(s3,'%04i') '.png']);

% Identify circle centered at x and y centroid locations
%  with a radius equal to 1/2 the average distance between
%  element centroids.
x=X(g,1);
y=X(g,2);
I = I(:,:,1);
R = FD/2;
Fx = 1:size(I,1);
Fy = 1:size(I,2)';
dx = x - Fx;
dy = y - Fy;
for i = 1:length(dx)
    for j = 1:length(dy)
        ds2(j,i) = dx(i)^2+dy(j)^2;
    end
end

% Plot the circle.
[jfind, ifind] = find(ds2<=R^2);
map = [0 0 0; 0 0 1; 0 1 0; 0 1 1; 1 1 1];
imshow(I,map)
hold on
plot(ifind, jfind, 'rx')
axis equal

% Determine intensity values for components.
for i = 1:length(ifind)
    V(i,1) = I(jfind(i), ifind(i));
end
```

```
            % Calculate area fractions of components in the circle.
            %  Estimate the elastic modulus for the circle.
            pixcount(g,5:8) = [length(find(V==1)), length(find(V==2)),
               length(find(V==3)), length(find(V==4))];
            fpix(g,5:8) = pixcount(g,5:8)/sum(pixcount(g,5:8));
            mpv = [3.88E5 2.45E6 1.82E7 1.07E8];
            mp(g,2) = dot(fpix(g,5:8),mpv);
            % Calculate the elastic modulus of the element using a
            %  linear interpolation scheme.
            mpfinal(g,1)=(((s2-s1)*(mp(g,2)-mp(g,1)))/(s3-s1))+mp(g,1);
            g
        end
    end
end

% Record material properties into a TXT file.
save MaterialProperties.txt mpfinal -ASCII
```

Specific Aim III:

Determine whether correlations between stress results from 3-D mechanical models and plaque features exist and whether these stress results are consistent with results from 2-D mechanical models.

Ansys Node File Conversion

nodefile.m

```
% This program converts Ansys node files into numbers only text files.
%  It is a modified version of code written by Peter Carnell.
% Sample format with column numbers:
%12345678901234567890123456789012345678901234567890123456789012345678901234567890
%  NODE        X           Y           Z         THXY    THYZ    THZX
%      1    3032.0      7873.0      10931.        0.00    0.00    0.00
%      2    3739.9      7505.2      9655.7        0.00    0.00    0.00
%12345678901234567890123456789012345678901234567890123456789012345678901234567890

clear all
close all

% Open file by inputting .lis file name
fid = fopen('<input>', 'r');
nread = 1;
eofstat = 0;

% Until end of file is reached...
while(eofstat==0)

    % Read each line as character string.
    tline = fgets(fid);

    % If character string meets data characteristics, extract data.
    if(length(tline)) > 7 & nread == str2num(tline(1:8));
        node(nread,1) = str2num(tline(1:9));
        x(nread,1) = str2num(tline(10:21));
        y(nread,1) = str2num(tline(22:33));
        z(nread,1) = str2num(tline(34:45));
        nread = nread + 1
    end
    eofstat = feof(fid);
end
fclose(fid);

X = [x y z];

% Record output into text file.
save NLIST.txt X -ASCII
```

Ansys Element File Conversion

elementfile.m

```
% This program converts Ansys element files into numbers only text
files.
%  It is a modified version of code written by Peter Carnell.

% Sample format with column numbers:
%12345678901234567890123456789012345678901234567890123456789012345678901234567890
%    ELEM    MAT    TYP    REL ESY    SEC        NODES
%
%       1      1      1      1   0      1   6009  2761  1684  6007
%       2      2      1      1   0      1   6008  2758  1683  2755
%12345678901234567890123456789012345678901234567890123456789012345678901234567890

clear all
close all
tic

% Open file by inputting .lis file name.

fid = fopen('<input>', 'r');

eread = 1;
eofstat = 0;

% Until end of file is reached...
while(eofstat==0)

    % Read each line as character string.
    tline = fgets(fid);

    % If character string meets data characteristics, extract data.
    if(length(tline)) > 7 & eread == str2num(tline(1:8));
        elem(eread,1) = str2num(tline(1:9));
        material(eread,1) = str2num(tline(10:13));
        type(eread,1) = str2num(tline(14:17));
        real_constant(eread,1) = str2num(tline(18:21));
        esys(eread,1) = str2num(tline(22:25));
        section(eread,1) = str2num(tline(26:29));
        topo(eread,1) = str2num(tline(30:36));
        topo(eread,2) = str2num(tline(37:42));
        topo(eread,3) = str2num(tline(43:48));
        topo(eread,4) = str2num(tline(49:54));
        eread = eread + 1;
    end
    eofstat = feof(fid);
end
fclose(fid);

% Record output into text file.
save ELIST.txt topo -ASCII
toc
```

Ansys Solution File Conversion

solutionfile.m

```
% This program converts Ansys solution files into numbers only text
%  files.  It is a modified version of code written by Peter Carnell.

% Sample format with column numbers:
%12345678901234567890123456789012345678901234567890123456789012345678901234567890
%  ELEMENT=       1        SOLID187
%     NODE    S1          S2          S3          SINT        SEQV
%    28289  0.10182E+06 -52508.     -95940.     0.19776E+06 0.18002E+06
%    17229   74716.      11625.    -0.14785E+06 0.22256E+06 0.19868E+06
%     2117  -85246.     -88244.    -0.25234E+06 0.16710E+06 0.16562E+06
%12345678901234567890123456789012345678901234567890123456789012345678901234567890


clear all
close all

% Open file by inputting .lis file name.
fid = fopen('<input>', 'r');


eofstat = 0;
enum = 1;
% Until end of file is reached...
while(eofstat==0)

    % Read each line as character string.
    tline = fgets(fid);

    % If character string meets data characteristics, extract data.
    if(length(tline) > 34 & tline(27) == 'S');
        tline = fgets(fid);
        for i = 1:4
            tline = fgets(fid);
            if(length(tline) > 25)
                node(enum,1) =  str2num(tline(2:9));
                S1(enum,1) =  str2num(tline(10:21));
                S2(enum,1) =  str2num(tline(22:33));
                S3(enum,1) =  str2num(tline(34:45));
                SINT(enum,1) = str2num(tline(46:57));
                SEQV(enum,1) = str2num(tline(58:69));
                enum=enum+1
            end
        end
    end
    eofstat = feof(fid);
    enum;
end

fclose(fid);

sprin = [node S1 S2 S3 SINT SEQV];
```

```
% Record output into text file.
save StressResults.txt sprin -ASCII
toc
```

3-D Model Stresses at 2-D Locations Calculation

3dresultsat2dlocations.m

```
% This program calculates stress results from 3-D model at inputted
%  axial locations of interest using an interpolation scheme.  It is a
%  modified version of a code written by Peter Carnell.

clear all
close all

% Read in nodal solutions from 3-D model by inputting .txt file name.
%  These are called input solutions.
v_in=load(['<input>']);

% Read in locations of nodal solutions from 3-D model by inputting .txt
%  file name.  These are called input coordinates.
coor_in=load(['<input>']);

% Read in nodal locations at axial locations of interest where
solutions
%  are to be obtained by inputting .txt file name.  These are called
%  output coordinates.
coor_out_all=load(['<input>']);

[m n]=size(coor_out_all);

% Number of nearest values to be used for interpolation.
numclose=8;

% Input axial sampling information.
zstart=<input>;
zinc=<input>;
numsections=<input>;


w=1;
e=1;
lf=0;
p=1;

for i=1:numsections

    % Isolate output coordinates at a particular axial location.
    q=find(coor_out_all(:,3)==zstart);
    [l b]=size(q);
    for i=1:l
        coor_out(i,1)=coor_out_all(q(i,1),1);
        coor_out(i,2)=coor_out_all(q(i,1),2);
        coor_out(i,3)=coor_out_all(q(i,1),3);
        coor_out(i,4)=q(i,1);
    end
```

```
    if(length(coor_in) == length(coor_out))
        iskip = 1;
    else
        iskip = 0;
    end
    h=waitbar(0,'please wait');
    % For each output coordinate, find the 8 (=numclose) closest input
    %  coordinates using a minimum distance calculation.

    for i=1:length(coor_out)
        waitbar(i/length(coor_out),h)
        temp_coor=coor_out(i,1:3);
        dist=sqrt((coor_in(:,1)-temp_coor(1)).^2+(coor_in(:,2)-
           temp_coor(2)).^2+(coor_in(:,3)-temp_coor(3)).^2);
        [temp,tempindex]=sort(dist);
        index=tempindex(1+iskip:numclose+iskip);

        % Calculate output solutions (solutions at axial locations of
        %  interest) using interpolation weighted by distances.
        for j=1:length(index)
            frac=1/dist(index(j))/sum(1./dist(index));
            Wv(j)=frac*v_in(index(j),1);
        end
        weighed_Wv=sum(Wv);
        v_out(i,:)=[sum(v_in(index,1))./length(index)];
    end
    close(h)

    % Store output solutions for a particular axial location.
    [m1 n1]=size(v_out);
    v_out_all=zeros(m,1)
    v_out_all_t(p:p+m1-1,1)=v_out;
    v_out_all_t_loc(p:p+m1-1,1)=coor_out(:,4);
    p=p+m1+1;

    % Go to next axial location.
    zstart=zstart+zinc;
    clear coor_out;
    clear v_out;

end

% Record output solutions into a text file.
save Outputsolutions.txt v_out_all -ASCII
```

Plot Stress Distribution

plotxsectionstressdistribution.m

```
% This program generates a cross-sectional stress distribution plot.

clear all
close all

% Read in nodal location information by inputting .txt file name.
X_all=load('<input>');

% Read in nodal connectivity information (Element file) by
inputting .txt file name.
topo_all=load('<input>');

% Read in nodal solutions by inputting .txt file name.
v2_all=load('<input>');

% Specify axial location of interest.
zstart_i=<input>

w=1;
e=1;
lf=0;
p=1;

% Isolate nodes at axial location of interest.
q=find(X_all(:,3)==zstart);
[l b]=size(q);

% Find elements containing isolated nodes.
for i=1:l
    [row col]=find(topo_all==q(i,1));
    emp=isempty(row);
    if emp==0
        [l2 ew]=size(row);
        for j=1:l2
            topo(lf+j,1)=topo_all(row(j,1),1);
            topo(lf+j,2)=topo_all(row(j,1),2);
            topo(lf+j,3)=topo_all(row(j,1),3);
            topo(lf+j,4)=topo_all(row(j,1),4);
        end
        lf=lf+l2;
    end
end

for i=1:l
    X(q(i,1),1)=X_all(q(i,1),1);
    X(q(i,1),2)=X_all(q(i,1),2);
    X(q(i,1),3)=X_all(q(i,1),3);
    v2(q(i,1),1)=v2_all(q(i,1),1);
end

% Plot stress distribution.
```

```
hold on
axis equal
axis ij
h = patch('Vertices', X, 'Faces', topo, 'FaceVertexCData', v2,
'FaceColor','interp')
colorbar
axis equal tight
axis off
```

Maximum Stress Acquisition and Upper Quartile Stress Average Calculation

upperquartileandmaxstress.m

```
% This program calculates the upper quartile stress and obtains the
%  maximum stress at axial locations of interest.

clear all
close all

% Read in nodal location information by inputting .txt file name.

X_all=load('<input>');


% Read in nodal solutions by inputting .txt file name.
v2_all=load('<input>');

% Input axial sampling information.
zstart_i=<input>;
zinc=<input>;
numsections=<input>;

for g=1:numsections

    % Choose particular axial location.
    zstart=zstart_i+zinc*(g-1);

    % Isolate nodes at particular axial location.
    q=find(X_all(:,3)==zstart);
    [l b]=size(q);

    % Find solutions at isolated nodes.
    for i=1:l
        X_s(i,1)=v2_all(q(i,1),1);
    end

   % Calculate average upper quartile stress and obtain maximum at
   %  particular axial location.
    X_s=sort(X_s);
    [r_s c_s]=size(X_s);
    qd=(r_s/4);
    Sq(g,1)=mean(X_s(round(qd*3)+1:round(qd*4),1));
    Sq(g,2)=max(X_s);
    clear X_s r_s c_s q
end

% Record results into a text file.
save StressResultsPerSection.txt Sq -ASCII
```

Fibrous Cap Thickness Calculation

fcthickness.m

```
% This program calculates the fibrous cap thickness at specified axial
%  locations.  It is a modified version of a code written by Shaun
%  Eshraghi.

clear all
close all

numsections=<input>;
ii=1;

for g=1:numsections

 % Read in binary images containing lumen and lipid pool only.
    A=imread(['FCImages\' num2str(g,'%04i') '.png']);
    bw = im2bw(A);
    [mm, nn] = size(bw);

    %Label the objects in the image.
    [L, num] = bwlabeln(bw);

    % Sort objects by size.
    sizedata = regionprops(L,'area');
    [valsort, indexsort] = sort([sizedata.Area]);
    [x, y]=size(valsort);

    % Determine centroid locations of objects.
    centerdata = regionprops(L, 'centroid');
    censort = centerdata(indexsort);
    bwedge = zeros(mm, nn);
    bwedgesum = zeros(mm,nn);
    temp = [censort(y).Centroid];

    % Centroid of lumen.
    xc = temp(1); yc = temp(2);

    % If only one object is found, do not calculate distance.
    if y>=2;

        % Isolate lipid pools one at a time.
        for kk = 1:(y-1);
            val= valsort(y-kk);
            loc = find([sizedata.Area]==val);
            [mm, nn] = size(L);
            newbw = zeros(mm, nn);
            for ii =1:mm;
                for jj = 1:nn;
                    if L(ii,jj) == loc;
                        newbw(ii,jj) = 1;
                    end
                end
            end
```

```
nc = round(xc);
mc = round(yc);
% Calculate angles at the centroid of lumen from the
%  horizontal to four corners of an image.
phi1 = atan(mc/(nn-nc));
phi2 = atan(mc/nc);
phi3 = atan((mm-mc)/nc);
phi4 = atan((mm-mc)/(nn-nc));

% Place border around image.
newbwbound(:,1:3) = ones(mm,3);
newbwbound(:,(nn-2:nn)) = ones(mm,3);
newbwbound((1:3),:) = ones(3,nn);
newbwbound((mm-2:mm),:) = ones(3,nn);
newbwbound = newbwbound + newbw;

% Isolate the edge of the lipid pool one octant at a time.
i1 = nc;
j1 = mc;

% Octant I.
for theta = 0:0.001:phi1;
    j1 =  mc;
    while newbwbound(j1, i1) == 0
        i1 = i1 + 1;
        j1 =  mc - fix((i1 - nc)*tan(theta));
    end
    if newbw(j1, i1) == 1;
        bwedge(j1, i1) = 1;
    end
    i1 = nc;
end

i1 = nc;
j1 = mc;

% Octant II.
for theta = 0:0.001:(pi/2 - phi1);
    i1 = nc;
    while newbwbound(j1, i1) == 0
        j1 = j1 - 1;
        i1 = nc + fix((mc - j1)*tan(theta));
    end
    if newbw(j1, i1) == 1;
        bwedge(j1, i1) = 1;
    end
    j1 = mc;
end

i1 = nc;
j1 = mc;



% Octant III.
for theta = 0:0.001:(pi/2 - phi2)
    i1 = nc;
```

```
    while newbwbound(j1, i1) == 0
        j1 = j1 - 1;
        i1 = nc - fix((mc - j1)*tan(theta));
    end
    if newbw(j1, i1) == 1;
        bwedge(j1, i1) = 1;
    end
    j1 = mc;
end

i1 = nc;
j1 = mc;

% Octant IV.
for theta = 0:0.001:phi2;
    j1 = mc;
    while newbwbound(j1, i1) == 0
        i1 = i1 - 1;
        j1 = mc + fix((i1 - nc)*tan(theta));
    end
    if newbw(j1, i1) == 1;
        bwedge(j1, i1) = 1;
    end
    i1 = nc;
end

i1 = nc;
j1 = mc;

% Octant V.
for theta = 0:0.001:phi3;
    j1 = mc;
    while newbwbound(j1, i1) == 0
        i1 = i1 - 1;
        j1 = mc - fix((i1 - nc)*tan(theta));
    end
    if newbw(j1, i1) == 1;
        bwedge(j1, i1) = 1;
    end
    i1 = nc;
end

i1 = nc;
j1 = mc;

% Octant VI.
for theta = 0:0.001:(pi/2 - phi3)
    i1 = nc;
    while newbwbound(j1, i1) == 0
        j1 = j1 + 1;
        i1 = nc - fix((mc - j1)*tan(theta));
    end
    if newbw(j1, i1) == 1;
        bwedge(j1, i1) = 1;
    end
    j1 = mc;
end
```

```
        i1 = nc;
        j1 = mc;

        % Octant VII.
        for theta = 0:0.001:(pi/2 - phi4);
            i1 = nc;
            while newbwbound(j1, i1) == 0
                j1 = j1 + 1;
                i1 = nc + fix((mc - j1)*tan(theta));
            end
            if newbw(j1, i1) == 1;
                bwedge(j1, i1) = 1;
            end
            j1 = mc;
        end


        i1 = nc;
        j1 = mc;

        % Octant VIII.
        for theta = 0:0.001:phi4;
            j1 = mc;
            while newbwbound(j1, i1) == 0
                i1 = i1 + 1;
                j1 = mc + fix((i1 - nc)*tan(theta));
            end
            if newbw(j1, i1) == 1;
                bwedge(j1, i1) = 1;
            end
            i1 = nc;
        end
        % Combine all lipid pool edges into a single image.
        bwedgesum = bwedgesum + bwedge;

    end
end

equest=exist('ii');



% Obtain image of lumen only.
if equest==1
    bwedgesum = im2bw(bwedgesum);
    lumenbw = zeros(ii,jj);
    for ii =1:mm;
        for jj = 1:nn;
            if L(ii,jj) == indexsort(y);
                lumenbw(ii,jj) = 1;
            end
        end
    end

    % Calculate fibrous cap thickness values.
    D_all = bwdist(lumenbw);
```

```
            D_lipid = D_all.*bwedgesum;
            counter = 1;
            sum = 0;
            for ii=1:mm
                for jj=1:nn
                    if D_lipid(ii,jj) ~= 0;
                        sum(counter,1) = D_lipid(ii,jj);
                        counter = counter + 1;
                    end
                end
            end

            % Obtain minimum fibrous cap thickness.
            fcthickness(ne,1) = min(sum)*6.67;
        end

        clear A D_all D_lipid L bw bwedge bwedgesum censort centerdata
        clear counter g i1 ii indexsort j1 jj kk loc lumenbw mc mm nc newbw
        clear newbwbound nn num numsections phi1 phi2 phi3 phi4 sc sizedata
        clear sum temp theta val valsort x xc y yc

    end
```

Lipid Content Calculation

lipidcontent.m

```
% This program calculates the lipid content at specified axial
locations.

clear all
close all

numsections=<input>;

countw=0;
countl=0;

for g=1:numsections

    % Read in binary image of arterial wall.
    I=imread(['Wall\' num2str(g,'%04i') '.png']);
    [r c x]= size(I);

   % Count number of wall pixels.
    for i=1:r
        for j=1:c
           if I(i,j,1)==255
               countw=countw+1;
           end
        end
    end

    % Read in binary image of lipid.
    L=imread(['Lipid\' num2str(g,'%04i') '.png']);
    [r c x]= size(L);

    % Count number of lipid pixels.
    for i=1:r
        for j=1:c
           if I(i,j,1)==255
               countl=countl+1;
           end
        end
    end

    % Calculate lipid content.
    Lc(g,1)=countl/countw;
    countw=0;
    countl=0;
end
```

Stenosis Severity Calculation

stenosisseverity.m

```
% This program calculates the stenosis severity at specified axial
% locations.

clear all
close all

numsections=<input>;

for g=1:numsections

    % Read in binary image of internal elastic lamina area.
    Iiel=imread(['IEL\' num2str(g,'%04i') '.png']);

    % Read in binary image of lumen.
    Ilu=imread(['Lumen\' num2str(g,'%04i') '.png']);

    Iiel = im2bw(Iiel);
    Ilu = im2bw(Ilu);

    % Obtain image of lesion area.
    Ile=Iel-Ilu;

    % Calculate internal elastic lamina area.
    [L3, num3]=bwlabel(Iiel);
    sizedata3 = regionprops(L3,'area');
    valsort3=sort([sizedata3.Area]);
    IELA(g,1)=valsort3;

    % Calculate lesion area.
    [L5, num5]=bwlabel(I5);
    sizedata5 = regionprops(L5,'area');
    valsort5=sort([sizedata5.Area]);
    LA(g,1)=valsort5;

    % Calculate stenosis severity.
    stenosis(g,1)= LA(g,1)/IELA(g,1);

    clear L5 num5 L3 num3 Iiel Ilu Ile sizedata3 valsort3 sizedata5
    clear valsort5

end
```

Calcification Content Calculation

calcificationcontent.m

```
% This program calculates the calcification content at specified axial
%  locations.

clear all
close all

numsections=<input>;

countw=0;
countc=0;

for g=1:numsections

    % Read in binary image of arterial wall.
    I=imread(['Wall\' num2str(g,'%04i') '.png']);
    [r c x]= size(I);

   % Count number of wall pixels.
    for i=1:r
        for j=1:c
           if I(i,j,1)==255
               countw=countw+1;
           end
        end
    end

    % Read in binary image of calcification.
    L=imread(['Lipid\' num2str(g,'%04i') '.png']);
    [r c x]= size(L);

    % Count number of calcification pixels.
    for i=1:r
        for j=1:c
           if I(i,j,1)==255
               countc=countc+1;
           end
        end
    end

    % Calculate calcification content.
    Lc(g,1)=countc/countw;
    countw=0;
    countl=0;
end
```

REFERENCES

1. Achenbach, S., Moselewski, F., Ropers, D., Ferencik, M., Hoffmann, U., MacNeill, B., Pohle, K., Baum, U., Anders, K., Jang, I. K., Daniel, W. G., and Brady, T. J., 2004, "Detection of Calcified and Noncalcified Coronary Atherosclerotic Plaque by Contrast-Enhanced, Submillimeter Multidetector Spiral Computed Tomography: A Segment-Based Comparison with Intravascular Ultrasound," Circulation, 109(1), pp. 14-17.

2. Amarenco, P., Duyckaerts, C., Tzourio, C., Henin, D., Bousser, M. G., and Hauw, J. J., 1992, "The Prevalence of Ulcerated Plaques in the Aortic Arch in Patients with Stroke," N Engl J Med, 326(4), pp. 221-225.

3. ANSYS, 2004a, "Ansys Elements Reference Manual," Release 9.0.

4. ANSYS, 2004b, "Ansys Theory Reference Manual," Release 9.0.

5. Arroyo, L. H., and Lee, R. T., 1999, "Mechanisms of Plaque Rupture: Mechanical and Biologic Interactions," Cardiovasc Res, 41(2), pp. 369-375.

6. Avolio, A., Jones, D., and Tafazzoli-Shadpour, M., 1998, "Quantification of Alterations in Structure and Function of Elastin in the Arterial Media," Hypertension, 32(1), pp. 170-175.

7. Bancroft, J. D., and Gamble, M., 2002, Theory and Practice of Histological Techniques, Churchill Livingstone, London.

8. Bank, A. J., Versluis, A., Dodge, S. M., and Douglas, W. H., 2000, "Atherosclerotic Plaque Rupture: A Fatigue Process?," Med Hypotheses, 55(6), pp. 480-484.

9. Baroldi, G., Silver, M. D., Mariani, F., and Giuliano, G., 1988, "Correlation of Morphological Variables in the Coronary Atherosclerotic Plaque with Clinical Patterns of Ischemic Heart Disease," Am J Cardiovasc Pathol, 2(2), pp. 159-172.

10. Beattie, D., Xu, C., Vito, R., Glagov, S., and Whang, M. C., 1998, "Mechanical Analysis of Heterogeneous, Atherosclerotic Human Aorta," J Biomech Eng, 120(5), pp. 602-607.

11. Becker, C. R., Nikolaou, K., Muders, M., Babaryka, G., Crispin, A., Schoepf, U. J., Loehrs, U., and Reiser, M. F., 2003, "Ex Vivo Coronary Atherosclerotic Plaque Characterization with Multi-Detector-Row Ct," Eur Radiol, 13(9), pp. 2094-2098.

12. Bezerra, H. G., Higuchi, M. L., Gutierrez, P. S., Palomino, S. A., Silvestre, J. M., Libby, P., and Ramires, J. A., 2001, "Atheromas That Cause Fatal Thrombosis

Are Usually Large and Frequently Accompanied by Vessel Enlargement," Cardiovasc Pathol, 10(4), pp. 189-196.

13. Biasucci, L. M., Liuzzo, G., Angiolillo, D. J., Sperti, G., and Maseri, A., 2000, "Inflammation and Acute Coronary Syndromes," Herz, 25(2), pp. 108-112.

14. Brezinski, M. E., Tearney, G. J., Bouma, B. E., Boppart, S. A., Hee, M. R., Swanson, E. A., Southern, J. F., and Fujimoto, J. G., 1996, "Imaging of Coronary Artery Microstructure (in Vitro) with Optical Coherence Tomography," Am J Cardiol, 77(1), pp. 92-93.

15. Burke, A. P., Farb, A., Malcom, G. T., Liang, Y. H., Smialek, J., and Virmani, R., 1997, "Coronary Risk Factors and Plaque Morphology in Men with Coronary Disease Who Died Suddenly," N Engl J Med, 336(18), pp. 1276-1282.

16. Burke, A. P., Virmani, R., Galis, Z., Haudenschild, C. C., and Muller, J. E., 2003, "34th Bethesda Conference: Task Force #2--What Is the Pathologic Basis for New Atherosclerosis Imaging Techniques?," J Am Coll Cardiol, 41(11), pp. 1874-1886.

17. Burke, A. P., Weber, D. K., Kolodgie, F. D., Farb, A., Taylor, A. J., and Virmani, R., 2001, "Pathophysiology of Calcium Deposition in Coronary Arteries," Herz, 26(4), pp. 239-244.

18. Carmines, D. V., McElhaney, J. H., and Stack, R., 1991, "A Piece-Wise Non-Linear Elastic Stress Expression of Human and Pig Coronary Arteries Tested in Vitro," J Biomech, 24(10), pp. 899-906.

19. Carnell, P. H., 2005, "Intramural Stress and Inflammation in Arterial Branches : A Histology-Based Approach," Ph.D. Thesis, Georgia Institute of Technology, Atlanta.

20. Carnell, P. H., Vito, R. P., and Taylor, W. R., 2006, "Characterizing Intramural Stress and Inflammation in Hypertensive Arterial Bifurcations," Biomech Model Mechanobiol.

21. Casscells, W., Naghavi, M., and Willerson, J. T., 2003, "Vulnerable Atherosclerotic Plaque: A Multifocal Disease," Circulation, 107(16), pp. 2072-2075.

22. Chau, A. H., Chan, R. C., Shishkov, M., MacNeill, B., Iftimia, N., Tearney, G. J., Kamm, R. D., Bouma, B. E., and Kaazempur-Mofrad, M. R., 2004, "Mechanical Analysis of Atherosclerotic Plaques Based on Optical Coherence Tomography," Ann Biomed Eng, 32(11), pp. 1494-1503.

23. Cheng, G. C., Loree, H. M., Kamm, R. D., Fishbein, M. C., and Lee, R. T., 1993, "Distribution of Circumferential Stress in Ruptured and Stable Atherosclerotic Lesions. A Structural Analysis with Histopathological Correlation," Circulation, 87(4), pp. 1179-1187.

24. Dalager-Pedersen, S., Falk, E., Ringgaard, S., Kristensen, I. B., and Pedersen, E. M., 1999, "Effects of Temperature and Histopathologic Preparation on the Size and Morphology of Atherosclerotic Carotid Arteries as Imaged by Mri," J Magn Reson Imaging, 10(5), pp. 876-885.

25. Davies, M. J., 1990, "A Macro and Micro View of Coronary Vascular Insult in Ischemic Heart Disease," Circulation, 82(3 Suppl), pp. II38-46.

26. Detrano, R., Hsiai, T., Wang, S., Puentes, G., Fallavollita, J., Shields, P., Stanford, W., Wolfkiel, C., Georgiou, D., Budoff, M., and Reed, J., 1996, "Prognostic Value of Coronary Calcification and Angiographic Stenoses in Patients Undergoing Coronary Angiography," J Am Coll Cardiol, 27(2), pp. 285-290.

27. Deverell, M. H., Bailey, N., and Whimster, W. F., 1989, "Tissue Distortion in Three-Dimensional Reconstruction of Wax or Plastic Embedded Microscopic Structures," Pathol Res Pract, 185(5), pp. 598-601.

28. Dorbin, P. B., 1996, "Effect of Histologic Preparation on the Cross-Sectional Area of Arterial Rings " Journal of Surgical Research, 61(2), pp. 413-415.

29. Dowling, N. E., 1999, Mechanical Behavior of Materials: Engineering Methods for Deformation, Fracture, and Fatigue, Prentice Hall, New Jersey, pp. 208-209.

30. Falk, E., 1982, "Coronary Artery Narrowing without Irreversible Myocardial Damage or Development of Collaterals. Assessment Of "Critical" Stenosis in a Human Model," Br Heart J, 48(3), pp. 265-271.

31. Falk, E., 1989, "Morphologic Features of Unstable Atherothrombotic Plaques Underlying Acute Coronary Syndromes," Am J Cardiol, 63(10), pp. 114E-120E.

32. Falk, E., Shah, P. K., and Fuster, V., 1995, "Coronary Plaque Disruption," Circulation, 92(3), pp. 657-671.

33. Farb, A., Burke, A. P., Tang, A. L., Liang, T. Y., Mannan, P., Smialek, J., and Virmani, R., 1996, "Coronary Plaque Erosion without Rupture into a Lipid Core. A Frequent Cause of Coronary Thrombosis in Sudden Coronary Death," Circulation, 93(7), pp. 1354-1363.

34. Finet, G., Ohayon, J., and Rioufol, G., 2004, "Biomechanical Interaction between Cap Thickness, Lipid Core Composition and Blood Pressure in Vulnerable Coronary Plaque: Impact on Stability or Instability," Coron Artery Dis, 15(1), pp. 13-20.

35. Friedman, M. H., Deters, O. J., Mark, F. F., Bargeron, C. B., and Hutchins, G. M., 1983, "Arterial Geometry Affects Hemodynamics. A Potential Risk Factor for Athersoclerosis," Atherosclerosis, 46(2), pp. 225-231.

36. Fung, Y. C., 1993, Biomechanics: Mechanical Properties of Living Tissues, Springer-Verlag, New York, NY.

37. Fuster, V., 1999, The Vulnerable Atherosclerotic Plaque. Understanding, Identification and Modification, Armonk, New York, NY, pp. 2-3.

38. Fuster, V., 1994, "Lewis A. Conner Memorial Lecture. Mechanisms Leading to Myocardial Infarction: Insights from Studies of Vascular Biology," Circulation, 90(4), pp. 2126-2146.

39. Galis, Z. S., Sukhova, G. K., Lark, M. W., and Libby, P., 1994, "Increased Expression of Matrix Metalloproteinases and Matrix Degrading Activity in Vulnerable Regions of Human Atherosclerotic Plaques," J Clin Invest, 94(6), pp. 2493-2503.

40. Giroud, D., Li, J. M., Urban, P., Meier, B., and Rutishauer, W., 1992, "Relation of the Site of Acute Myocardial Infarction to the Most Severe Coronary Arterial Stenosis at Prior Angiography," Am J Cardiol, 69(8), pp. 729-732.

41. Glagov, S., Weisenberg, E., Zarins, C. K., Stankunavicius, R., and Kolettis, G. J., 1987, "Compensatory Enlargement of Human Atherosclerotic Coronary Arteries," N Engl J Med, 316(22), pp. 1371-1375.

42. Gonzalez, R. C., and Woods, R. E., 2002, Digital Imaging Processing, Prentice Hall, Upper Saddle River, NJ.

43. Hangartner, J. R., Charleston, A. J., Davies, M. J., and Thomas, A. C., 1986, "Morphological Characteristics of Clinically Significant Coronary Artery Stenosis in Stable Angina," Br Heart J, 56(6), pp. 501-508.

44. Hansson, G. K., Libby, P., Schonbeck, U., and Yan, Z. Q., 2002, "Innate and Adaptive Immunity in the Pathogenesis of Atherosclerosis," Circ Res, 91(4), pp. 281-291.

45. Helander, K. G., 1994, "Kinetic Studies of Formaldehyde Binding in Tissue," Biotech Histochem, 69(3), pp. 177-179.

46. Henney, A. M., Wakeley, P. R., Davies, M. J., Foster, K., Hembry, R., Murphy, G., and Humphries, S., 1991, "Localization of Stromelysin Gene Expression in Atherosclerotic Plaques by in Situ Hybridization," Proc Natl Acad Sci U S A, 88(18), pp. 8154-8158.

47. Hermiller, J. B., Tenaglia, A. N., Kisslo, K. B., Phillips, H. R., Bashore, T. M., Stack, R. S., and Davidson, C. J., 1993, "In Vivo Validation of Compensatory Enlargement of Atherosclerotic Coronary Arteries," Am J Cardiol, 71(8), pp. 665-668.

48. Holzapfel, G. A., Sommer, G., and Regitnig, P., 2004, "Anisotropic Mechanical Properties of Tissue Components in Human Atherosclerotic Plaques," J Biomech Eng, 126(5), pp. 657-665.

49. Holzapfel, G. A., Stadler, M., and Gasser, T. C., 2005, "Changes in the Mechanical Environment of Stenotic Arteries During Interaction with Stents: Computational Assessment of Parametric Stent Designs," J Biomech Eng, 127(1), pp. 166-180.

50. Holzapfel, G. A., Stadler, M., and Schulze-Bauer, C. A., 2002, "A Layer-Specific Three-Dimensional Model for the Simulation of Balloon Angioplasty Using Magnetic Resonance Imaging and Mechanical Testing," Ann Biomed Eng, 30(6), pp. 753-767.

51. Huang, H., Virmani, R., Younis, H., Burke, A. P., Kamm, R. D., and Lee, R. T., 2001, "The Impact of Calcification on the Biomechanical Stability of Atherosclerotic Plaques," Circulation, 103(8), pp. 1051-1056.

52. Humphrey, J. D., 2002, "Cardiovascular Solid Mechanics: Cells, Tissues, and Organs," Springer-Verlag, New York, NY.

53. Humphrey, J. D., and Rajagopal, K. R., 2002, "A Constrained Mixture Model for Growth and Remodeling of Soft Tissues," Mathematical Models and Methods in Applied Science, 12(3), pp. 407-430.

54. Islam, A. L., and Frisch, B., 1985, "Plastic Embedding in Routine Histology. I: Preparation of Semithin Resin Sections of Undecalcified Marrow Cores," Histopathology, 9, pp. 1263-1274.

55. Jang, I. K., Bouma, B. E., Kang, D. H., Park, S. J., Park, S. W., Seung, K. B., Choi, K. B., Shishkov, M., Schlendorf, K., Pomerantsev, E., Houser, S. L., Aretz, H. T., and Tearney, G. J., 2002, "Visualization of Coronary Atherosclerotic Plaques in Patients Using Optical Coherence Tomography: Comparison with Intravascular Ultrasound," J Am Coll Cardiol, 39(4), pp. 604-609.

56. Jones, A. S., Milthorpe, B. K., and Howlett, C. R., 1994, "Measurement of Microtomy-Induced Section Distortion and Its Correction for 3-Dimensional Histological Reconstructions," Cytometry, 15(2), pp. 95-105.

57. Kilpatrick, D., Goudet, C., Sakaguchi, Y., Bassiouny, H. S., Glagov, S., and Vito, R., 2001, "Effect of Plaque Composition on Fibrous Cap Stress in Carotid Endarterectomy Specimens," J Biomech Eng, 123(6), pp. 635-638.

58. Kilpatrick, D., Xu, C., Vito, R., and Glavgov, S., 2002, "Correlation of Mechanical Behavior and Mmp-1 Presence in Human Atherosclerotic Plaque," Journal of Mechanics in Medicine and Biology 1(2), pp. 1-7.

59. Kragel, A. H., Reddy, S. G., Wittes, J. T., and Roberts, W. C., 1989, "Morphometric Analysis of the Composition of Atherosclerotic Plaques in the Four Major Epicardial Coronary Arteries in Acute Myocardial Infarction and in Sudden Coronary Death," Circulation, 80(6), pp. 1747-1756.

60. Ku, D. N., Giddens, D. P., Zarins, C. K., and Glagov, S., 1985, "Pulsatile Flow and Atherosclerosis in the Human Carotid Bifurcation. Positive Correlation between Plaque Location and Low Oscillating Shear Stress," Arteriosclerosis, 5(3), pp. 293-302.

61. Kukreja, N., Garcia-Garcia, H. M., and Serruys, P. W., 2006, "Invasive Imaging Techniques for the Assessment of Vulnerable Plaque," Minerva Cardioangiol, 54(5), pp. 603-617.

62. Lee, R. T., 2000, "Plaque Stabilization: The Role of Lipid Lowering," Int J Cardiol, 74 Suppl 1, pp. S11-15.

63. Lee, R. T., Grodzinsky, A. J., Frank, E. H., Kamm, R. D., and Schoen, F. J., 1991, "Structure-Dependent Dynamic Mechanical Behavior of Fibrous Caps from Human Atherosclerotic Plaques," Circulation, 83(5), pp. 1764-1770.

64. Lee, R. T., and Libby, P., 1997, "The Unstable Atheroma," Arterioscler Thromb Vasc Biol, 17(10), pp. 1859-1867.

65. Lee, R. T., Schoen, F. J., Loree, H. M., Lark, M. W., and Libby, P., 1996, "Circumferential Stress and Matrix Metalloproteinase 1 in Human Coronary Atherosclerosis. Implications for Plaque Rupture," Arterioscler Thromb Vasc Biol, 16(8), pp. 1070-1073.

66. Lendon, C. L., Davies, M. J., Born, G. V., and Richardson, P. D., 1991, "Atherosclerotic Plaque Caps Are Locally Weakened When Macrophages Density Is Increased," Atherosclerosis, 87(1), pp. 87-90.

67. Lendon, C. L., Davies, M. J., Richardson, P. D., and Born, G. V., 1993, "Testing of Small Connective Tissue Specimens for the Determination of the Mechanical Behaviour of Atherosclerotic Plaques," J Biomed Eng, 15(1), pp. 27-33.

68. LeVeen, R. F., Wolf, G. L., and Turco, M. A., 1983, "Morphometric Changes in Normal Arteries and Those Undergoing Transluminal Angioplasty," Investigative Radiology, 18(1), pp. 63-67.

69. Libby, P., 2002, "Atherosclerosis: The New View," Sci Am, 286(5), pp. 46-55.

70. Libby, P., 2001, "Current Concepts of the Pathogenesis of the Acute Coronary Syndromes," Circulation, 104(3), pp. 365-372.

71. Libby, P., 1995, "Molecular Bases of the Acute Coronary Syndromes," Circulation, 91(11), pp. 2844-2850.

72. Libby, P., Ridker, P. M., and Maseri, A., 2002, "Inflammation and Atherosclerosis," Circulation, 105(9), pp. 1135-1143.

73. Little, W. C., Constantinescu, M., Applegate, R. J., Kutcher, M. A., Burrows, M. T., Kahl, F. R., and Santamore, W. P., 1988, "Can Coronary Angiography Predict the Site of a Subsequent Myocardial Infarction in Patients with Mild-to-Moderate Coronary Artery Disease?," Circulation, 78(5 Pt 1), pp. 1157-1166.

74. Loree, H. M., Grodzinsky, A. J., Park, S. Y., Gibson, L. J., and Lee, R. T., 1994a, "Static Circumferential Tangential Modulus of Human Atherosclerotic Tissue," J Biomech, 27(2), pp. 195-204.

75. Loree, H. M., Kamm, R. D., Stringfellow, R. G., and Lee, R. T., 1992, "Effects of Fibrous Cap Thickness on Peak Circumferential Stress in Model Atherosclerotic Vessels," Circ Res, 71(4), pp. 850-858.

76. Loree, H. M., Tobias, B. J., Gibson, L. J., Kamm, R. D., Small, D. M., and Lee, R. T., 1994b, "Mechanical Properties of Model Atherosclerotic Lesion Lipid Pools," Arterioscler Thromb, 14(2), pp. 230-234.

77. Losordo, D. W., Rosenfield, K., Kaufman, J., Pieczek, A., and Isner, J. M., 1994, "Focal Compensatory Enlargement of Human Arteries in Response to Progressive Atherosclerosis. In Vivo Documentation Using Intravascular Ultrasound," Circulation, 89(6), pp. 2570-2577.

78. Low, A. F., Tearney, G. J., Bouma, B. E., and Jang, I. K., 2006, "Technology Insight: Optical Coherence Tomography--Current Status and Future Development," Nat Clin Pract Cardiovasc Med, 3(3), pp. 154-162; quiz 172.

79. Lowder, M. L., Li, S., Carnell, P. H., and Vito, R. P., 2007, "Correction of Distortion of Histologic Sections of Arteries," J Biomech, 40(2), pp. 445-450.

80. Manfrini, O., Mont, E., Leone, O., Arbustini, E., Eusebi, V., Virmani, R., and Bugiardini, R., 2006, "Sources of Error and Interpretation of Plaque Morphology by Optical Coherence Tomography," Am J Cardiol, 98(2), pp. 156-159.

81. Marcu, L., Fishbein, M. C., Maarek, J. M., and Grundfest, W. S., 2001, "Discrimination of Human Coronary Artery Atherosclerotic Lipid-Rich Lesions by Time-Resolved Laser-Induced Fluorescence Spectroscopy," Arterioscler Thromb Vasc Biol, 21(7), pp. 1244-1250.

82. McCarthy, J. H., and Palmer, F. J., 1974, "Incidence and Significance of Coronary Artery Calcification," Br Heart J, 36(5), pp. 499-506.

83. Moreno, P. R., Falk, E., Palacios, I. F., Newell, J. B., Fuster, V., and Fallon, J. T., 1994, "Macrophage Infiltration in Acute Coronary Syndromes. Implications for Plaque Rupture," Circulation, 90(2), pp. 775-778.

84. Murashige, A., Hiro, T., Fujii, T., Imoto, K., Murata, T., Fukumoto, Y., and Matsuzaki, M., 2005, "Detection of Lipid-Laden Atherosclerotic Plaque by Wavelet Analysis of Radiofrequency Intravascular Ultrasound Signals: In Vitro Validation and Preliminary in Vivo Application," J Am Coll Cardiol, 45(12), pp. 1954-1960.

85. Nair, A., Kuban, B. D., Obuchowski, N., and Vince, D. G., 2001, "Assessing Spectral Algorithms to Predict Atherosclerotic Plaque Composition with Normalized and Raw Intravascular Ultrasound Data," Ultrasound Med Biol, 27(10), pp. 1319-1331.

86. Nair, A., Kuban, B. D., Tuzcu, E. M., Schoenhagen, P., Nissen, S. E., and Vince, D. G., 2002, "Coronary Plaque Classification with Intravascular Ultrasound Radiofrequency Data Analysis," Circulation, 106(17), pp. 2200-2206.

87. Newby, A. C., and Zaltsman, A. B., 1999, "Fibrous Cap Formation or Destruction--the Critical Importance of Vascular Smooth Muscle Cell Proliferation, Migration and Matrix Formation," Cardiovasc Res, 41(2), pp. 345-360.

88. Nikkari, S. T., O'Brien, K. D., Ferguson, M., Hatsukami, T., Welgus, H. G., Alpers, C. E., and Clowes, A. W., 1995, "Interstitial Collagenase (Mmp-1) Expression in Human Carotid Atherosclerosis," Circulation, 92(6), pp. 1393-1398.

89. Nikolaou, K. L., Becker, C. R., Flohr, T., Huber, A., Scheidler, J., Fayad, Z. A., and Reiser, M. F., 2004, "Optimization of Ex Vivo Ct- and Mr- Imaging of Atherosclerotic Vessel Wall Changes," Int J Cardiovasc Imaging, 20(4), pp. 327-334.

90. Noll, G., 1998, "Pathogenesis of Atherosclerosis: A Possible Relation to Infection," Atherosclerosis, 140 Suppl 1, pp. S3-9.

91. Ohayon, J., Finet, G., Treyve, F., Rioufol, G., and Dubreuil, O., 2005, "A Three-Dimensional Finite Element Analysis of Stress Distribution in a Coronary Atherosclerotic Plaque: In-Vivo Prediction of Plaque Rupture Location," Biomechanics Applied to Computer Assisted Surgery, 37, pp. 225-241.

92. Ohayon, J., Teppaz, P., Finet, G., and Rioufol, G., 2001, "In-Vivo Prediction of Human Coronary Plaque Rupture Location Using Intravascular Ultrasound and the Finite Element Method," Coron Artery Dis, 12(8), pp. 655-663.

93. Park, J. C., Siegel, R. J., and Demer, L. L., 1993, "Effect of Calcification and Formalin Fixation on in Vitro Distensibility of Human Femoral Arteries," Am Heart J, 125(2 Pt 1), pp. 344-349.

94. Pasterkamp, G., Schoneveld, A. H., van der Wal, A. C., Haudenschild, C. C., Clarijs, R. J., Becker, A. E., Hillen, B., and Borst, C., 1998, "Relation of Arterial

Geometry to Luminal Narrowing and Histologic Markers for Plaque Vulnerability: The Remodeling Paradox," J Am Coll Cardiol, 32(3), pp. 655-662.

95. Patwari, P., Weissman, N. J., Boppart, S. A., Jesser, C., Stamper, D., Fujimoto, J. G., and Brezinski, M. E., 2000, "Assessment of Coronary Plaque with Optical Coherence Tomography and High-Frequency Ultrasound," Am J Cardiol, 85(5), pp. 641-644.

96. Piegl, L., and Tiller, W., 1997, The Nurbs Book, Springer Verlag, Berlin.

97. Pletcher, M. J., Tice, J. A., Pignone, M., and Browner, W. S., 2004, "Using the Coronary Artery Calcium Score to Predict Coronary Heart Disease Events: A Systematic Review and Meta-Analysis," Arch Intern Med, 164(12), pp. 1285-1292.

98. Rachev, A., Manoach, E., Berry, J., and Moore, J. E., Jr., 2000, "A Model of Stress-Induced Geometrical Remodeling of Vessel Segments Adjacent to Stents and Artery/Graft Anastomoses," J Theor Biol, 206(3), pp. 429-443.

99. Raggi, P., Callister, T. Q., Cooil, B., He, Z. X., Lippolis, N. J., Russo, D. J., Zelinger, A., and Mahmarian, J. J., 2000, "Identification of Patients at Increased Risk of First Unheralded Acute Myocardial Infarction by Electron-Beam Computed Tomography," Circulation, 101(8), pp. 850-855.

100. Reddy, J. N., 1993, " " An Introduction to the Finite Element Method, McGraw-Hill, New York, NY, p. 68.

101. Rey, F. E., and Pagano, P. J., 2002, "The Reactive Adventitia: Fibroblast Oxidase in Vascular Function," Arterioscler Thromb Vasc Biol, 22(12), pp. 1962-1971.

102. Richardson, P. D., 2002, "Biomechanics of Plaque Rupture: Progress, Problems, and New Frontiers," Ann Biomed Eng, 30(4), pp. 524-536.

103. Richardson, P. D., Davies, M. J., and Born, G. V., 1989, "Influence of Plaque Configuration and Stress Distribution on Fissuring of Coronary Atherosclerotic Plaques," Lancet, 2(8669), pp. 941-944.

104. Rifkin, R. D., Parisi, A. F., and Folland, E., 1979, "Coronary Calcification in the Diagnosis of Coronary Artery Disease," Am J Cardiol, 44(1), pp. 141-147.

105. Rosamond, W., Flegal, K., Friday, G., Furie, K., Go, A., Greenlund, K., Haase, N., Ho, M., Howard, V., Kissela, B., Kittner, S., Lloyd-Jones, D., McDermott, M., Meigs, J., Moy, C., Nichol, G., O'Donnell, C. J., Roger, V., Rumsfeld, J., Sorlie, P., Steinberger, J., Thom, T., Wasserthiel-Smoller, S., and Hong, Y., 2007, "Heart Disease and Stroke Statistics--2007 Update: A Report from the American Heart Association Statistics Committee and Stroke Statistics Subcommittee," Circulation, 115(5), pp. e69-171.

106. Ross, R., 1999, "Atherosclerosis--an Inflammatory Disease," N Engl J Med, 340(2), pp. 115-126.

107. Rumberger, J. A., Simons, D. B., Fitzpatrick, L. A., Sheedy, P. F., and Schwartz, R. S., 1995, "Coronary Artery Calcium Area by Electron-Beam Computed Tomography and Coronary Atherosclerotic Plaque Area. A Histopathologic Correlative Study," Circulation, 92(8), pp. 2157-2162.

108. Saia, F., Schaar, J., Regar, E., Rodriguez, G., De Feyter, P. J., Mastik, F., Marzocchi, A., Marrozzini, C., Ortolani, P., Palmerini, T., Branzi, A., van der Steen, A. F., and Serruys, P. W., 2006, "Clinical Imaging of the Vulnerable Plaque in the Coronary Arteries: New Intracoronary Diagnostic Methods," J Cardiovasc Med (Hagerstown), 7(1), pp. 21-28.

109. Salunke, N. V., Topoleski, L. D., Humphrey, J. D., and Mergner, W. J., 2001, "Compressive Stress-Relaxation of Human Atherosclerotic Plaque," J Biomed Mater Res, 55(2), pp. 236-241.

110. Schmermund, A., and Erbel, R., 2001, "Unstable Coronary Plaque and Its Relation to Coronary Calcium," Circulation, 104(14), pp. 1682-1687.

111. Schoenhagen, P., Ziada, K. M., Kapadia, S. R., Crowe, T. D., Nissen, S. E., and Tuzcu, E. M., 2000, "Extent and Direction of Arterial Remodeling in Stable Versus Unstable Coronary Syndromes : An Intravascular Ultrasound Study," Circulation, 101(6), pp. 598-603.

112. Schroeder, W., Martin, K., and Lorensen, B., 1998, The Visualization Toolkit, an Object-Oriented Approach to 3d Graphics Prentice-Hall, New Jersey.

113. Shaalan, W. E., Cheng, H., Gewertz, B., McKinsey, J. F., Schwartz, L. B., Katz, D., Cao, D., Desai, T., Glagov, S., and Bassiouny, H. S., 2004, "Degree of Carotid Plaque Calcification in Relation to Symptomatic Outcome and Plaque Inflammation," J Vasc Surg, 40(2), pp. 262-269.

114. Siegel, R. J., Swan, K., Edwalds, G., and Fishbein, M. C., 1985, "Limitations of Postmortem Assessment of Human Coronary Artery Size and Luminal Narrowing: Differential Effects of Tissue Fixation and Processing on Vessels with Different Degrees of Atherosclerosis," J Am Coll Cardiol, 5(2 Pt 1), pp. 342-346.

115. Skrinjar, O., 2004, "Discussions and Notes on Image Segmentation Techniques."

116. St Goar, F. G., Pinto, F. J., Alderman, E. L., Fitzgerald, P. J., Stinson, E. B., Billingham, M. E., and Popp, R. L., 1992, "Detection of Coronary Atherosclerosis in Young Adult Hearts Using Intravascular Ultrasound," Circulation, 86(3), pp. 756-763.

117. Stary, H. C., Chandler, A. B., Dinsmore, R. E., Fuster, V., Glagov, S., Insull, W., Jr., Rosenfeld, M. E., Schwartz, C. J., Wagner, W. D., and Wissler, R. W., 1995, "A Definition of Advanced Types of Atherosclerotic Lesions and a Histological Classification of Atherosclerosis. A Report from the Committee on Vascular Lesions of the Council on Arteriosclerosis, American Heart Association," Arterioscler Thromb Vasc Biol, 15(9), pp. 1512-1531.

118. Stary, H. C., Chandler, A. B., Glagov, S., Guyton, J. R., Insull, W., Jr., Rosenfeld, M. E., Schaffer, S. A., Schwartz, C. J., Wagner, W. D., and Wissler, R. W., 1994, "A Definition of Initial, Fatty Streak, and Intermediate Lesions of Atherosclerosis. A Report from the Committee on Vascular Lesions of the Council on Arteriosclerosis, American Heart Association," Circulation, 89(5), pp. 2462-2478.

119. Swindle, M., 1992, Swine as Models in Biomedical Research, Iowa State University Press, Ames.

120. Tang, D., Yang, C., Zheng, J., Woodard, P. K., Sicard, G. A., Saffitz, J. E., and Yuan, C., 2004, "3d Mri-Based Multicomponent Fsi Models for Atherosclerotic Plaques," Ann Biomed Eng, 32(7), pp. 947-960.

121. Taylor, A. J., Burke, A. P., O'Malley, P. G., Farb, A., Malcom, G. T., Smialek, J., and Virmani, R., 2000, "A Comparison of the Framingham Risk Index, Coronary Artery Calcification, and Culprit Plaque Morphology in Sudden Cardiac Death," Circulation, 101(11), pp. 1243-1248.

122. Topoleski, L. D., and Salunke, N. V., 2000, "Mechanical Behavior of Calcified Plaques: A Summary of Compression and Stress-Relaxation Experiments," Z Kardiol, 89 Suppl 2, pp. 85-91.

123. Topoleski, L. D., Salunke, N. V., Humphrey, J. D., and Mergner, W. J., 1997, "Composition- and History-Dependent Radial Compressive Behavior of Human Atherosclerotic Plaque," J Biomed Mater Res, 35(1), pp. 117-127.

124. Tuzcu, E. M., Hobbs, R. E., Rincon, G., Bott-Silverman, C., De Franco, A. C., Robinson, K., McCarthy, P. M., Stewart, R. W., Guyer, S., and Nissen, S. E., 1995, "Occult and Frequent Transmission of Atherosclerotic Coronary Disease with Cardiac Transplantation. Insights from Intravascular Ultrasound," Circulation, 91(6), pp. 1706-1713.

125. Valenta, J., Vitek, K., Cihak, R., Konvickova, S., Sochor, M., and Horny, L., 2002, "Age Related Constitutive Laws and Stress Distribution in Human Main Coronary Arteries with Reference to Residual Strain," Biomed Mater Eng, 12(2), pp. 121-134.

126. Varnava, A. M., Mills, P. G., and Davies, M. J., 2002, "Relationship between Coronary Artery Remodeling and Plaque Vulnerability," Circulation, 105(8), pp. 939-943.

127. Veress, A. I., Cornhill, J. F., Herderick, E. E., and Thomas, J. D., 1998, "Age-Related Development of Atherosclerotic Plaque Stress: A Population-Based Finite-Element Analysis," Coron Artery Dis, 9(1), pp. 13-19.

128. Veress, A. I., Vince, D. G., Anderson, P. M., Cornhill, J. F., Herderick, E. E., Klingensmith, J. D., Kuban, B. D., Greenberg, N. L., and Thomas, J. D., 2000, "Vascular Mechanics of the Coronary Artery," Z Kardiol, 89 Suppl 2, pp. 92-100.

129. Versluis, A., Bank, A. J., and Douglas, W. H., 2006, "Fatigue and Plaque Rupture in Myocardial Infarction," J Biomech, 39(2), pp. 339-347.

130. Virmani, R., Kolodgie, F. D., Burke, A. P., Farb, A., and Schwartz, S. M., 2000, "Lessons from Sudden Coronary Death: A Comprehensive Morphological Classification Scheme for Atherosclerotic Lesions," Arterioscler Thromb Vasc Biol, 20(5), pp. 1262-1275.

131. Virmani, R., Kolodgie, F. D., Burke, A. P., Finn, A. V., Gold, H. K., Tulenko, T. N., Wrenn, S. P., and Narula, J., 2005, "Atherosclerotic Plaque Progression and Vulnerability to Rupture: Angiogenesis as a Source of Intraplaque Hemorrhage," Arterioscler Thromb Vasc Biol, 25(10), pp. 2054-2061.

132. Vito, R. P., and Dixon, S. A., 2003, "Blood Vessel Constitutive Models-1995-2002," Annu Rev Biomed Eng, 5, pp. 413-439.

133. Vonesh, M. J., Cho, C. H., Pinto, J. V., Jr., Kane, B. J., Lee, D. S., Roth, S. I., Chandran, K. B., and McPherson, D. D., 1997, "Regional Vascular Mechanical Properties by 3-D Intravascular Ultrasound with Finite-Element Analysis," Am J Physiol, 272(1 Pt 2), pp. H425-437.

134. Waddell, T. K., Dart, A. M., Gatzka, C. D., Cameron, J. D., and Kingwell, B. A., 2001, "Women Exhibit a Greater Age-Related Increase in Proximal Aortic Stiffness Than Men," J Hypertens, 19(12), pp. 2205-2212.

135. Weissberg, P. L., 2000, "Atherogenesis: Current Understanding of the Causes of Atheroma," Heart, 83(2), pp. 247-252.

136. Welgus, H. G., Campbell, E. J., Cury, J. D., Eisen, A. Z., Senior, R. M., Wilhelm, S. M., and Goldberg, G. I., 1990, "Neutral Metalloproteinases Produced by Human Mononuclear Phagocytes. Enzyme Profile, Regulation, and Expression During Cellular Development," J Clin Invest, 86(5), pp. 1496-1502.

137. Wilcox, J. N., 1992, "Analysis of Local Gene Expression in Human Atherosclerotic Plaques," J Vasc Surg, 15(5), pp. 913-916.

138. Wilensky, R. L., Song, H. K., and Ferrari, V. A., 2006, "Role of Magnetic Resonance and Intravascular Magnetic Resonance in the Detection of Vulnerable Plaques," J Am Coll Cardiol, 47(8 Suppl), pp. C48-56.

139. Wilhjelm, J. E., Vogt, K., Jespersen, S. K., and Sillesen, H., 1997, "Influence of Tissue Preservation Methods on Arterial Geometry and Echogenicity," Ultrasound Med Biol, 23(7), pp. 1071-1082.

140. Williamson, S. D., Lam, Y., Younis, H. F., Huang, H., Patel, S., Kaazempur-Mofrad, M. R., and Kamm, R. D., 2003, "On the Sensitivity of Wall Stresses in Diseased Arteries to Variable Material Properties," J Biomech Eng, 125(1), pp. 147-155.

141. Wolinsky, H., and Glagov, S., 1967, "A Lamellar Unit of Aortic Medial Structure and Function in Mammals," Circ Res, 20(1), pp. 99-111.

142. Wolinsky, H., and Glagov, S., 1964, "Structural Basis for the Static Mechanical Properties of the Aortic Media," Circ Res, 14, pp. 400-413.

143. Worthley, S. G., Helft, G., Fuster, V., Fayad, Z. A., Fallon, J. T., Osende, J. I., Roque, M., Shinnar, M., Zaman, A. G., Rodriguez, O. J., Verhallen, P., and Badimon, J. J., 2000, "High Resolution Ex Vivo Magnetic Resonance Imaging of in Situ Coronary and Aortic Atherosclerotic Plaque in a Porcine Model," Atherosclerosis, 150(2), pp. 321-329.

144. Yabushita, H., Bouma, B. E., Houser, S. L., Aretz, H. T., Jang, I. K., Schlendorf, K. H., Kauffman, C. R., Shishkov, M., Kang, D. H., Halpern, E. F., and Tearney, G. J., 2002, "Characterization of Human Atherosclerosis by Optical Coherence Tomography," Circulation, 106(13), pp. 1640-1645.

145. Yutani, C., Imakita, M., Ishibashi-Ueda, H., Tsukamoto, Y., Nishida, N., and Ikeda, Y., 1999, "Coronary Atherosclerosis and Interventions: Pathological Sequences and Restenosis," Pathol Int, 49(4), pp. 273-290.

146. Zheng, J., El Naqa, I., Rowold, F. E., Pilgram, T. K., Woodard, P. K., Saffitz, J. E., and Tang, D., 2005, "Quantitative Assessment of Coronary Artery Plaque Vulnerability by High-Resolution Magnetic Resonance Imaging and Computational Biomechanics: A Pilot Study Ex Vivo," Magn Reson Med, 54(6), pp. 1360-1368.